

# SELF-CONSISTENT CALCULATIONS OF HADRON PROPERTIES AT NON-ZERO TEMPERATURE

Dissertation  
zur Erlangung des Doktorgrades  
der Naturwissenschaften  
vorgelegt beim Fachbereich Physik  
der Johann Wolfgang Goethe-Universität  
in Frankfurt am Main

von  
Wolf Christian Beckmann  
aus Düsseldorf

Frankfurt am Main 2005

(D 30)

vom Fachbereich Physik der Johann Wolfgang Goethe-Universität  
als Dissertation angenommen

Dekan: Prof. Dr. Wolf Aßmus

Gutachter: Prof. Dr. Dirk H. Rischke  
Prof. Dr. Carsten Greiner

Datum der Disputation: 28. März 2006

# TABLE OF CONTENTS

<b>1</b>	<b>Introduction</b>	<b>9</b>
1.1	Theoretical background . . . . .	10
1.2	Quantum field theory and the path integral quantization . . . . .	12
1.3	Approximation schemes . . . . .	25
1.3.1	Perturbation expansion . . . . .	25
1.3.2	The loop expansion . . . . .	28
1.3.3	The Cornwall-Jackiw-Tomboulis formalism . . . . .	30
1.4	Quantum field theory at non-zero temperature . . . . .	34
1.5	The standard model . . . . .	36
1.6	Quantum chromodynamics . . . . .	37
1.6.1	Phases of nuclear matter . . . . .	42
1.7	Effective models . . . . .	44
1.7.1	The Walecka model . . . . .	47
1.8	The intention of this work . . . . .	48
<b>2</b>	<b>The Hartree approximation</b>	<b>51</b>
2.1	Results in Hartree approximation . . . . .	57
2.1.1	Thermodynamic properties . . . . .	59
<b>3</b>	<b>Beyond the Hartree approximation</b>	<b>67</b>
3.1	General prerequisites . . . . .	67
3.1.1	The spectral function . . . . .	67
3.1.2	Projection operators for the vector mesons . . . . .	72
3.1.3	The Dirac structure of the fermions . . . . .	75
3.2	The self-energies, masses, and fields . . . . .	76
3.2.1	The self-energy of the $\sigma$ meson . . . . .	78
3.2.2	The self-energy of the $\omega$ meson . . . . .	84
3.2.3	The fermion self-energy . . . . .	87
3.2.4	The imaginary parts of the self-energies . . . . .	95
3.2.5	Self-energies and spectral functions . . . . .	95
3.2.6	Sum rules . . . . .	98
3.2.7	The field equation and the masses . . . . .	102
3.3	Numerical solution of the self-consistent equations . . . . .	103

---

3.4	Results in the improved approximation . . . . .	105
3.4.1	The masses and the fields . . . . .	105
3.4.2	The bosonic spectral functions . . . . .	109
3.4.3	The fermionic spectral functions . . . . .	115
<b>4</b>	<b>Conclusions and outlook</b>	<b>125</b>
<b>A</b>	<b>Conventions</b>	<b>129</b>
<b>B</b>	<b>Determination of the parameters</b>	<b>131</b>
<b>C</b>	<b>Deutsche Zusammenfassung</b>	<b>135</b>

# LIST OF FIGURES

1.1	A possible path for the field value at the fixed point $\mathbf{x}_l$ in space. . .	14
1.2	A possible evolution of the disturbing source term with time. . . .	20
1.3	Feynman diagrams for two- and four-point Green's functions. . . .	23
1.4	A quartic self-interaction vertex. . . . .	25
1.5	Connecting two legs of a vertex gives a one-loop diagram. . . . .	26
1.6	Perturbation series up to third order. . . . .	27
1.7	The one-particle irreducible loops in the self-energy. . . . .	27
1.8	$SU(3)$ -multiplets of baryons (left) baryon resonances (middle) and scalar mesons (right). . . . .	38
1.9	Fundamental quark (left) and anti-quark (right) representation of $SU(3)$ . . . . .	39
1.10	Schematic phase diagram of strongly interacting matter. . . . .	43
2.1	The two-particle irreducible diagrams which are considered in this thesis. Dashed lines represent $\sigma$ propagators, wavy lines $\omega$ propagators and full lines stand for fermion propagators. . . . .	52
2.2	The tadpole-diagram which forms the $\sigma$ meson self-energy in Hartree-approximation. . . . .	53
2.3	The integration contour for the calculation of Matsubara sums. The dots mark the poles of the cotangent. . . . .	54
2.4	The mass of the $\sigma$ field in Hartree approximation compared to tree-level approximation. At low temperatures the curves lie on top of each other so only the grey lines are visible. . . . .	58
2.5	The mass of the fermion in Hartree approximation (black lines) and on tree-level (grey lines). At high chemical potentials in the left diagram and low temperatures in the right one the curves lie on top of each other so only the grey lines are visible. . . . .	60
2.6	The $\sigma$ field in Hartree approximation (black lines) and on tree-level (grey lines). At high chemical potentials in the left diagram and low temperatures in the right one the curves lie on top of each other so only the grey lines are visible. . . . .	60

2.7	The pressure (left) and the entropy density (right) in Hartree and tree-level approximation. The differences between the approximations are almost invisible. . . . .	65
2.8	The pressure (left) and the entropy density (right) in Hartree and tree-level approximation at $T = 200$ MeV. The figure highlights the differences between the approximations. . . . .	65
3.1	Vertices containing fermion lines can be connected only in one way.	77
3.2	Distribution of momenta in sunset diagrams. . . . .	78
3.3	The self-energy of the $\sigma$ meson in diagrammatic language. . . . .	79
3.4	The self-energy of the $\omega$ -meson in diagrammatic language. . . . .	84
3.5	The self-energy of the fermion in diagrammatic language. . . . .	88
3.6	The hatched region shows the momenta which are integrated over. The momentum integration is constrained by the Theta function. Note that the size of this region depends on the external momentum.	104
3.7	The left figure shows the $\sigma$ field in comparison of the Hartree-, tree-level and the improved approximation. The right diagram shows the same comparison for the mass of the fermion. . . . .	106
3.8	The two integral terms of the $\sigma$ field equation. The left-hand figure shows the integral over $\mathcal{G}_\sigma$ while the right-hand side shows the scalar density which is the term proportional to $g_\sigma$ . . . . .	107
3.9	Mass of the $\sigma$ field in the Hartree, tree-level, and the improved approximation. . . . .	108
3.10	The spectral function of the $\sigma$ meson at a temperature of $T = 100$ MeV, $T = 150$ MeV, $T = 200$ MeV and $T = 250$ MeV. . . . .	110
3.11	The decay width of the $\sigma$ meson as a function of temperature at $k = 165$ MeV. The width approximately increases exponentially with higher temperatures. . . . .	111
3.12	The imaginary part of the self-energy (left-hand side) and the complete spectral function (right-hand side) of the $\sigma$ meson at $T = 150$ MeV. . . . .	111
3.13	The spectral function of the $\sigma$ meson at a momentum of $k = 165$ MeV as a function of energy at $T = 150$ MeV, $T = 200$ MeV and $T = 250$ MeV. Beside the mass-shell and the two-baryon decay one can see the two $\sigma$ -meson decay of the sunset diagram at an energy of twice the effective $\sigma$ mass. . . . .	112
3.14	The transverse projection of the spectral function of the $\omega$ meson at a temperature of $T = 100$ MeV, $T = 150$ MeV, $T = 200$ MeV and $T = 250$ MeV. . . . .	113

3.15	The transverse (left) and longitudinal (right) projection of the $\omega$ -meson spectral function at a momentum of $k = 495$ MeV as a function of energy at $T = 150$ MeV, $T = 200$ MeV and $T = 250$ MeV. The fermion-anti-fermion decay is very pronounced at the lower two temperatures and merges with the mass-shell peak at $T = 250$ MeV. . . . .	114
3.16	The decay width of the transverse and the longitudinal projection of the $\omega$ meson at different temperatures and a momentum of $k = 765$ MeV. Both widths approximately increase exponentially with temperature. . . . .	115
3.17	The longitudinal projection of the spectral function of the $\omega$ meson at a temperature of $T = 100$ MeV, $T = 150$ MeV, $T = 200$ MeV and $T = 250$ MeV. . . . .	116
3.18	The part of the fermionic spectral density which is proportional to $\gamma_0$ at a temperature of $T = 100$ MeV, $T = 150$ MeV, $T = 200$ MeV and $T = 250$ MeV. . . . .	117
3.19	The width of the fermion spectral function $\rho_0$ as a function of momentum at different temperatures and $k = 765$ MeV. . . . .	118
3.20	Cut through the spectral function $\rho_0$ of the fermion at a momentum of $k = 195$ MeV. The onset of the $\sigma$ meson decay is clearly visible between $\omega = 1400$ MeV and $\omega = 1500$ MeV at the lower two temperatures. At higher temperatures this process only alters the slope a bit. The interaction with the $\omega$ meson occurs at around $\omega = 1700$ MeV as a little step at $T = 150$ MeV. . . . .	119
3.21	The part of the fermionic spectral density which is proportional to the unit matrix, $\rho_m$ , at a temperature of $T = 100$ MeV, $T = 150$ MeV, $T = 200$ MeV and $T = 250$ MeV. . . . .	120
3.22	Cut through the fermion spectral function $\rho_0$ at a momentum of $k = 195$ MeV. The onset of the decay with the $\sigma$ meson is clearly visible between $\omega = 1400$ MeV and $\omega = 1500$ MeV. Also the $\omega$ decay at around $\omega = 1700$ MeV is visible as a little step at the lower two temperatures. . . . .	121
3.23	The part of the fermionic spectral density which is proportional to $\gamma_i$ at a temperature of $T = 100$ MeV, $T = 150$ MeV, $T = 200$ MeV and $T = 250$ MeV. . . . .	122
3.24	Cut through the fermion spectral function $\rho_v$ at a momentum of $k = 195$ MeV. The onset of the decay with the $\sigma$ meson is clearly visible between $\omega = 1400$ MeV and $\omega = 1500$ MeV. The $\omega$ -meson decay occurs at $\omega = 1720$ MeV and moves to the right together with the fermion mass. . . . .	123





—I—

## INTRODUCTION

IN THE BEGINNING was the big bang. The universe was created and has been expanding ever since. During its evolution it passed through different stages, eventually forming our world as we know it today. Just  $10^{-33}$  seconds after the big bang particles such as quarks and anti-quarks were formed. The temperature at this time was about  $10^{25}\text{K}$  ( $10^{12}\text{GeV}$ ) which was far too high for compound objects to exist. Quarks and anti-quarks together with the exchange particles of their interaction, the gluons, moved freely, building a form of matter which is known as the *quark-gluon plasma*.

As the universe continued to expand it became bigger and cooler. Only some  $10^{-5}$  seconds after its formation the temperature had dropped to  $2 \times 10^{12}\text{K}$  (200 MeV). This allowed the quarks and gluons to bind into composite particles, the *hadrons*. Thus the universe went through a phase transition from the quark-gluon-plasma phase to the *hadronic phase*. All different kinds of hadrons were created, containing not only the lighter quarks which make up today's world, but also all heavier quarks. However, with continuing expansion most of the heavy hadrons decayed, leaving matter that consisted mainly of the light up- and down-quarks. The surviving hadrons were the nucleons, i.e., protons and neutrons made from three quarks as well as the light mesons, built from a quark and an anti-quark. The big bang produced quarks and anti-quarks in nearly equal amounts. Therefore, the number of nucleons was almost identical to that of their anti-particles, which are built from three anti-quarks. At around  $10^{-4}$  seconds after the big bang, when the temperature had fallen to around  $10^{12}\text{K}$  (100 MeV), these nucleons and anti-nucleons annihilated each other.

The numbers of particles and anti-particles were, however, apparently not exactly equal. Had this been the case all nucleons would have been annihilated, leaving nothing to form today's universe where it is obvious that nucleons exist.

The production of nucleons and anti-nucleons stopped at this stage of the evolution. The only things to be created at this point were pairs of leptons, e.g. electrons and positrons. Eventually, these also annihilated each other when the

universe had reached a temperature of  $10^{10}$  K (1 MeV) which was about one second later. Again, the numbers of electrons and positrons were not exactly equal, leading to a surplus of electrons of about one billionth. These are observed today. Some ten seconds after this the protons and neutrons left over from the annihilation started combining to form the first atomic nuclei. About 25 % of the new nuclei were  $^4\text{He}$ , 0.001 % deuterium as well as minor amounts of  $^3\text{He}$ , lithium and beryllium. Just five minutes later, the synthesis of nuclei came to an end and the next few minutes saw the decay of the remaining neutrons.

It took another 397 000 years for the universe to reach a temperature of 3000 K. At this point the density of radiation reached a level which made it possible for electrons to combine with nuclei to form the first atoms. Since light does not interact with atoms to the same extent as with free electrons, radiation could now propagate freely and the universe became transparent.

In the course of the evolution matter became more and more influenced by gravity. Clusters formed and eventually galaxies, stars and the earth, where today, about 14 billion years after the big bang, man is wondering where he came from. What did he find out?

## 1.1 Theoretical background

The efforts to understand nature have always been governed by the ambition to find principles explaining observations. The aim has been to come from a descriptive view of the world to a deductive one. These principles were after all expressed in mathematical terms, i.e., objects of observation were identified with well-defined mathematical objects while certain coherences between these objects had the status of mathematical axioms. This procedure led to objectivity.

But there was another implication of the quest for general principles that could be phrased with the paradox sounding clause "The more you want to describe, the fewer words you need". And in fact this turned out to be a characteristic of physical theories. The first success in this direction was achieved in classical mechanics, where Newton was able to attribute all phenomena to only three axioms, known as Newton's laws. Similarly, it was found that the whole world of classical electrodynamics can be described by just the four Maxwell's equations. However, at the beginning of the 20th century it turned out that these two theories had not been an exhaustive description of the world. In fact it emerged that classical mechanics failed to describe processes at very high velocities (close to the speed of light). Up until then it had not been possible to perform experiments which tested this region. As a consequence, in 1905 the theory of special relativity was developed by Albert Einstein. It turned out that classical mechanics is contained in this theory as the limit of low velocities. The new theory caused a fundamental change in the pictures of space and time which physicists had, but was now far more comprehensive. The revolution of the prevalent space-time

picture was continued by Einstein in his theory of general relativity (1914), where he was able to describe gravity as a curvature of space-time.

And there was another area where physics could not be explained in the framework of the classical theories: It emerged that at small distances (so that Heisenberg's uncertainty principle gains relevance at around  $10^{-8}m$ ) matter adopts wave properties. This was a fundamental contradiction to the then prevalent picture that matter can be assigned an exact place in space. On the other hand it was found that waves behave like particles. Electromagnetic waves, in particular, whose wave characteristics had been deduced from classical electrodynamics, appeared as particles in certain arrangements as for example the photo-effect. The contradiction in this problem was solved by *quantum mechanics*, developed by scientists around Max Planck, Niels Bohr, Werner Heisenberg, and Erwin Schrödinger at the beginning of the 20th century. Quantum mechanics describes particles in terms of waves. The energy of the particle is identified with the frequency and its momentum is related to the wave length. To extract the original particle properties from the waves, mathematical operators are introduced for each of them. This procedure is known as *quantization*. Again, classical mechanics was comprised in this new theory, but now as the limit of large distances.

In their quest for unification and more general principles, physicists tried to combine quantum mechanics with the theory of special relativity to be able to describe quantum phenomena at high velocities (meaning high energies in practice). Paul Dirac, Oskar Benjamin Klein, and Walter Gordon played a major role in this development.

However, this new *relativistic quantum mechanics* had a serious shortcoming: Special relativity allows for the conversion of mass into energy and vice versa, expressed by the relation  $E = mc^2$ . In elementary particle physics this means that the number of particles is not conserved but changes naturally, so that more than one particle is generally involved. Thus particle physics cannot be treated in the framework of a one particle-theory like relativistic quantum mechanics. Even if the energy is not sufficient for particle creation, Heisenberg's uncertainty principle,  $\Delta E \Delta t \geq \hbar$ , allows for the appearance of particle pairs for a very short time. A consistent relativistic theory thus has to allow for particle creation and annihilation.

This demand led to the development of *quantum field theories* (e.g. [PS95]) where particles are treated as fields and the quantized variables are the field strengths. The applicability of quantum field theories is rather general. The particles of the standard model for example, which will be introduced in detail below, are treated in three quantum field theories, namely *quantum chromodynamics (QCD)* which is the theory of the strong interaction, *quantum electrodynamics (QED)* that describes the electromagnetic interactions and furthermore the *theory of weak interactions*. Also compound particles such as baryons and mesons can be covered by quantum field theories because they are also small and relativistic. This is indeed an important point, since later it will be shown that many calculations

cannot be carried out in the framework of the theories of the actual elementary particles, in particular in QCD. Therefore alternative theories for compound particles are often developed.

But quantum field theories are also used outside elementary particle physics. As a completely different application, quantum field-theoretical methods are also used in solid state physics where the fields are phonon fields, for example. Let us get a little more insight into the ideas of quantum field theory in general.

## 1.2 Quantum field theory and the path integral quantization

In classical mechanics as well as quantum mechanics the basic quantities of consideration are space and momentum because a given particle can be assigned a place and a momentum. This is obviously no longer possible if the particle number is not conserved as in relativistic theories. An alternative is the description of particles in terms of fields. A field associates a value to a space-time point, i.e., it is a function  $\phi(X)$ . For simplicity, only neutral (real-valued) scalar fields are considered in the following.

It is known from classical field theory that the dynamics of a field can be expressed by the Lagrange function

$$L = \int d^3x \mathcal{L}[\phi(X), \partial_\mu \phi(X)] \quad . \quad (1.1)$$

The canonical conjugate momentum is then

$$\pi(X) = \frac{\partial \mathcal{L}}{\partial(\partial_t \phi)} \quad . \quad (1.2)$$

Thus instead of space and momentum, the fundamental variables are now the field and the conjugate momentum field.

As in classical field theory the Hamilton function is the Legendre transform of  $L$ :

$$H = \int d^3x \mathcal{H}(\pi, \phi) = \int d^3x (\pi \partial_t \phi - \mathcal{L}) \quad . \quad (1.3)$$

The Hamilton function stated here defines a *classical* field theory. To apply it to quantum fields one has to *quantize* the field and the conjugate momentum, i.e., assign operators as

$$\begin{aligned} \phi(X) &\longrightarrow \hat{\phi}(X) \\ \pi(X) &\longrightarrow \hat{\pi}(X) \quad , \end{aligned} \quad (1.4)$$

where the field operator has a set of time-dependent eigenstates

$$\hat{\phi}(X)|\phi, t\rangle = \phi(X)|\phi, t\rangle \quad . \quad (1.5)$$

At this point two alternatives for the further procedure exist. The first one is the so called *canonical quantization* where commutation relations for the operators are postulated. These commutation relations account for the impossibility to measure the field and its momentum at the same time. The other alternative is *path integral quantization* which is the method of choice in this work and will therefore be described in more detail in the following.

Let us start with the *quantum mechanical situation*. In quantum mechanics position is the quantized variable (or momentum in momentum space). The idea of path integration is then to sum up coherently all possible paths in space that a particle can take to get from one point to some other. As a simple example one could imagine a particle passing through the famous double slit: There are two possible ways for the particle to get from one side to the other, namely through one of the slits. Thus the amplitude for the particle to propagate to the other side is the *coherent* sum of the two amplitudes for the particle to pass through each slit. Summing up coherently means that the phase of the particle's wave function is taken into account. The result will be the well-known interference pattern.

In *quantum field theory* the quantized variable is the field. Again the idea is to build the coherent sum of different paths. But now the paths are not paths in position but in values of the field. Thus for a given location the path integral states the amplitude for the field at a time  $t$  to assume a certain value at a different time  $t'$ . This shall be concretized in the following.

With the introduction of operators in (1.4) also the Hamilton function becomes an operator. This *Hamilton operator*  $\hat{H}$  contains the complete information about the time evolution of the field. If a field is in the state  $|\phi, t\rangle$  at some time  $t$  one can construct the state of the field  $|\phi, t'\rangle$  at a time  $t'$  by applying the *time evolution operator*

$$|\phi, t'\rangle = e^{i\hat{H}(t'-t)}|\phi, t\rangle \quad . \quad (1.6)$$

However, this is just a formal construction of the field at different times. For physical purposes the interesting question is how the field actually evolves with time. More precisely one wants to know the probability for a field in the state  $|\phi, t\rangle$  to evolve into the state  $|\phi', t'\rangle$ , i.e., the transition amplitude

$$\langle\phi', t'|\phi, t\rangle = \langle\phi'|e^{-i\hat{H}(t'-t)}|\phi\rangle \quad . \quad (1.7)$$

This quantity is known as *Feynman core*.

With the Feynman core the time evolution of any field can be calculated just by integration <sup>1</sup>

$$\hat{\phi}(\mathbf{x}', t') = \int d\phi \langle\phi', t'|\phi, t\rangle \hat{\phi}(\mathbf{x}, t) \quad . \quad (1.8)$$

---

<sup>1</sup>In mathematical terms this is a convolution and the Feynman core takes the role of a Green's function. In fact one can show in general that, if some cause is linearly connected to an effect, the effect can be constructed from the cause by convoluting with a Green's function.

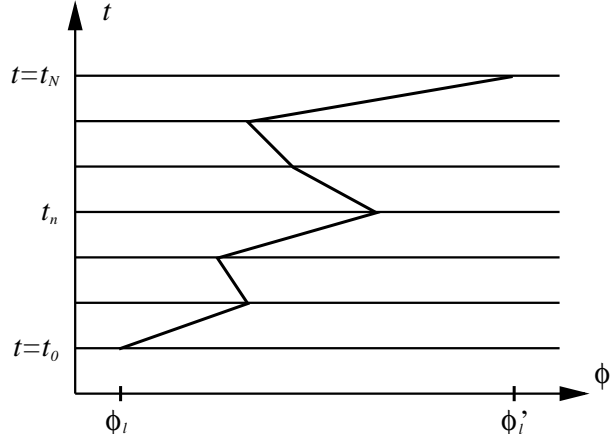


Figure 1.1: A possible path for the field value at the fixed point  $\mathbf{x}_l$  in space.

To compute this quantity explicitly we discretize space and time so that we can track the field's path.

This is done by splitting the time interval of consideration  $(t, t')$  into  $N$  small steps of equal distance  $\epsilon$  with the intermediate times  $t_n$ , where  $n = 0, \dots, N$  and  $t_0 = t, t_1 = t + \epsilon, \dots, t_N = t'$ . Furthermore, space is discretized in  $M$  points  $\mathbf{x}_l$ , where  $l = 1, \dots, M$ . At each of these points relation (1.7) can be applied separately. For simplicity the field operator is denoted in brief as  $\hat{\phi}_{ln} := \hat{\phi}(\mathbf{x}_l, t_n)$  in the following. The transition amplitude (1.7) can be written as the product of the amplitudes at the different points in space

$$\langle \phi', t' | \phi, t \rangle \simeq \prod_{l=1}^M \langle \phi'_l, t' | \phi_l, t \rangle \quad . \quad (1.9)$$

One can now make use of the discretization of time by decomposing the amplitude  $\langle \phi'_l, t' | \phi_l, t \rangle$  into amplitudes from every time step to the next at a given point in space as shown in fig.1.1 . This can be achieved by applying the completeness relation for the eigenstates  $|\phi_{ln}\rangle$  of the field operator  $\hat{\phi}_{ln}$  at a given point in space and time

$$\int d\phi_{ln} |\phi_{ln}\rangle \langle \phi_{ln}| = 1 \quad . \quad (1.10)$$

By inserting these identities into (1.9) the transition amplitude becomes

$$\begin{aligned} \prod_{l=1}^M \langle \phi'_l, t' | \phi_l, t \rangle &= \prod_{l=1}^M \int d\phi_{lN-1} \dots \int d\phi_{l2} \int d\phi_{l1} \langle \phi'_{l0} | e^{-i\hat{H}\epsilon} | \phi_{lN-1} \rangle \dots \\ &\times \langle \phi_{l2} | e^{-i\hat{H}\epsilon} | \phi_{l1} \rangle \langle \phi_{l1} | e^{-i\hat{H}\epsilon} | \phi_{l0} \rangle \quad . \end{aligned} \quad (1.11)$$

Eventually one is interested in the limit where the number of time steps  $N$  becomes infinite and the path continuous. It is therefore sufficient to calculate the

amplitude for infinitesimal adjacent times in a Taylor expansion

$$\langle \phi_{ln+1} | e^{-i\hat{H}\epsilon} | \phi_{ln} \rangle = \langle \phi_{ln+1} | 1 - i\hat{H}\epsilon | \phi_{ln} \rangle + \mathcal{O}(\epsilon^2) \quad . \quad (1.12)$$

According to (1.11) the transition amplitude is thus the product of the amplitudes at every time step, integrated over all values the field can adopt at every step. In other words the field can take different paths through its values, each having a certain amplitude. The complete amplitude is then the coherent integral over all possible paths.

For the consideration of discretized paths also the Hamilton operator has to be discretized. This is achieved by just replacing the spatial integral by a sum

$$\hat{H} = \int d^3x \hat{\mathcal{H}}(\hat{\pi}, \hat{\phi}) \quad \longrightarrow \quad \hat{H} = \sum_{l=1}^M \Delta V \hat{\mathcal{H}}(\hat{\pi}_l, \hat{\phi}_l) \quad . \quad (1.13)$$

The eigenstates of the conjugate field operator  $\hat{\pi}_{ln}$  also obey a completeness relation

$$\int \frac{d\pi_{ln}}{2\pi} \Delta V |\pi_{ln}\rangle \langle \pi_{ln}| = 1 \quad , \quad (1.14)$$

which can be used to calculate the matrix element of the Hamilton operator

$$\begin{aligned} \langle \phi_{ln+1} | \hat{H}(\hat{\pi}, \hat{\phi}) | \phi_{ln} \rangle &= \int \frac{d\pi_{ln}}{2\pi} \Delta V \langle \phi_{ln+1} | \pi_{ln} \rangle \langle \pi_{ln} | \hat{H} | \phi_{ln} \rangle \\ &= \int \frac{d\pi_{ln}}{2\pi} \Delta V \langle \phi_{ln+1} | \pi_{ln} \rangle \langle \pi_{ln} | \phi_{ln} \rangle \Delta V \mathcal{H}(\pi_{ln}, \phi_{ln}). \end{aligned} \quad (1.15)$$

Here it has been used that the Hamilton operator is a functional of the field operator  $\hat{\phi}$  and the conjugate field operator  $\hat{\pi}$ . Those act on their eigenstates in the first line of (1.15) so the Hamilton operator can be replaced by the classical Hamilton density where the eigenvalues are variables. In quantum mechanics it is known that a momentum eigenstate in space is just a plane wave

$$\langle q | p \rangle = e^{ipq} \quad . \quad (1.16)$$

A similar relation holds for the field and its conjugated field:

$$\langle \phi_{ln} | \pi_{ln} \rangle = e^{i\Delta V \pi_{ln} \phi_{ln}} \quad . \quad (1.17)$$

With this (1.15) is evaluated and the result is inserted into the transition amplitude of two neighboring time steps (1.12)

$$\langle \phi_{ln+1} | \phi_{ln} \rangle = \int \frac{d\pi_{ln}}{2\pi} \Delta V e^{i\Delta V \pi_{ln}(\phi_{ln+1} - \phi_{ln})} [1 - i\epsilon \Delta V \mathcal{H}(\pi_{ln}, \phi_{ln})] + \mathcal{O}(\epsilon^2) \quad . \quad (1.18)$$

For discrete space-time one can now calculate the Feynman core by inserting (1.18) into (1.11). By using

$$1 - i\epsilon\Delta V\mathcal{H} \simeq e^{-i\epsilon\Delta V\mathcal{H}} \quad (1.19)$$

for small  $\epsilon$ , equation (1.9) becomes

$$\begin{aligned} \langle \phi', t' | \phi, t \rangle &\simeq \prod_{l=1}^M \left( \prod_{n=1}^{N-1} \int d\phi_{ln} \prod_{n=0}^{N-1} \int \frac{d\pi_{ln}}{2\pi} \Delta V \right) \\ &\times \exp \left\{ i\epsilon\Delta V \sum_{n=0}^{N-1} \sum_{l=1}^M \left[ \pi_{ln} \frac{\phi_{ln+1} - \phi_{ln}}{\epsilon} - \mathcal{H}(\pi_{ln}, \phi_{ln}) \right] \right\} . \end{aligned} \quad (1.20)$$

Since this expression is given for a discrete space-time one can identify the time derivative

$$\dot{\phi}_{ln} = \frac{\phi_{ln+1} - \phi_{ln}}{\epsilon} \quad (1.21)$$

in the exponent. At this point an important simplification can be made if the Hamilton function only depends on the square of the conjugate field. Then the momentum integration becomes an ordinary Gaussian integral which can be carried out explicitly. This is done in the following. For clarity only one integral at a single space-time point is considered.

Let the Hamilton function be of the form

$$\mathcal{H}(\pi, \phi) = \frac{1}{2}\pi^2 + \mathcal{H}'(\phi) . \quad (1.22)$$

From (1.2) and (1.3) it follows that  $\pi = \dot{\phi}$ . Then the transition amplitude from one time step to the next (compare eqs. (1.18) and (1.20)) is

$$\begin{aligned} \langle \phi_{ln+1} | e^{-i\hat{H}\epsilon} | \phi_{ln} \rangle &\simeq \int \frac{d\pi_{ln}}{2\pi} \Delta V \exp \left\{ i\epsilon\Delta V \left[ \pi_{ln} \dot{\phi}_{ln} - \frac{1}{2}\pi_{ln}^2 - \mathcal{H}'(\phi_{ln}) \right] \right\} \\ &= \frac{\Delta V}{2\pi} \exp \left\{ i\epsilon\Delta V \left[ \frac{1}{2}\dot{\phi}_{ln}^2 - \mathcal{H}'(\phi_{ln}) \right] \right\} \int_{-\infty}^{\infty} d\pi' e^{-\frac{1}{2}i\epsilon\Delta V \pi'^2} \\ &= \left( \frac{2\pi i\epsilon}{\Delta V} \right)^{-1/2} \exp \left\{ i\epsilon\Delta V \left[ \frac{1}{2}\dot{\phi}_{ln}^2 - \mathcal{H}'(\phi_{ln}) \right] \right\} , \end{aligned} \quad (1.23)$$

where the standard form of the Gaussian integral has been extracted and then been integrated. Finally this result is inserted into (1.20) and the continuum limit is performed:

$$\begin{aligned} \langle \phi', t' | \phi, t \rangle &= \lim_{V \rightarrow \infty} \lim_{M \rightarrow \infty} \lim_{N \rightarrow \infty} \prod_{l=1}^M \prod_{n=1}^{N-1} \int d\phi_{ln} \left( \frac{2\pi i\epsilon}{\Delta V} \right)^{-N/2} \\ &\times \exp \left\{ i\epsilon\Delta V \sum_{n=0}^{N-1} \sum_{l=1}^M \mathcal{L}(\phi_{ln}, \partial_\mu \phi_{ln}) \right\} . \end{aligned} \quad (1.24)$$



Here the Lagrange density has been introduced according to (1.3). By defining the abbreviation

$$\int \mathcal{D}\phi := \lim_{V \rightarrow \infty} \lim_{M \rightarrow \infty} \lim_{N \rightarrow \infty} \prod_{l=1}^M \prod_{n=1}^{N-1} \int d\phi_{ln} \quad , \quad (1.25)$$

(1.24) can be written as

$$\langle \phi', t' | \phi, t \rangle = \mathcal{N} \int \mathcal{D}\phi e^{i \int d^4 X \mathcal{L}(\phi, \partial_\mu \phi)} \quad . \quad (1.26)$$

Again the integration runs over all paths with  $\phi(t) = \phi$  and  $\phi(t') = \phi'$ . The quantity  $\mathcal{N}$  is a normalization constant which is undetermined. However, usually one is only interested in the functional form of the path integral, so the constant is irrelevant. It drops out when physical quantities are computed (compare (1.39)). The result (1.26) shows that all possible paths contribute to the transition amplitude with the same amount but with a different phase which is given by the action

$$I(\phi, \partial_\mu \phi) = \int d^4 X \mathcal{L}(\phi, \partial_\mu \phi) \quad . \quad (1.27)$$

When considering macroscopic systems, where  $I \gg \hbar$ , the contributions of different neighboring paths will cancel in average. Only if  $I(\phi, \partial_\mu \phi)$  is stationary in the vicinity of a path this will contribute. This demand is well known from classical field theory. It is the Hamilton principle which states that the actual path of a field (in the sense introduced above) is the one where the action becomes stationary:  $\delta I = 0$ . In quantum systems the phase factor will not necessarily lead to cancellation, so interference effects occur like those in the double slit system in quantum mechanics.

### Feynman propagators and correlation functions

The Feynman core characterizes the evolution of a given state in time. For practical purposes a quantity is needed that accounts for the interaction as well as the creation and annihilation of particle fields. Let us consider the most simple case: A particle is created at a given point in space time and annihilated at a different point with  $t_i > t_j$ :

$$\langle 0 | \hat{\phi}(X_i) \hat{\phi}(X_j) | 0 \rangle \quad . \quad (1.28)$$

This quantity is known as the *Feynman propagator* or *two-point correlation function*. It can be calculated within the path integral formalism as follows.

We start with the matrix element of the product of two field operators  $\hat{\phi}(X_i)$  and  $\hat{\phi}(X_j)$  in the space of its eigenstates  $\langle \phi', t' |$  and  $|\phi, t\rangle$ . As in (1.11) one considers the discretized path integral

$$\langle \phi'_l, t' | \hat{\phi}(\mathbf{x}_l, t_i) \hat{\phi}(\mathbf{x}_l, t_j) | \phi_l, t \rangle = \int d\phi_{lN-1} \cdots \int d\phi_{l2} \int d\phi_{l1} \langle \phi'_{lN} | \phi_{lN-1} \rangle \cdots$$

$$\begin{aligned}
& \times \langle \phi_{li+1} | \hat{\phi}(\mathbf{x}_l, t_i) | \phi_{li} \rangle \cdots \langle \phi_{lj+1} | \hat{\phi}(\mathbf{x}_l, t_j) | \phi_{lj} \rangle \\
& \times \cdots \langle \phi_{l1} | \phi_{l0} \rangle \quad .
\end{aligned} \tag{1.29}$$

For simplicity only one point in space is shown here. Since the field operators act on their eigenstates one can replace them by their eigenvalues which contribute just as a factor. Thus the total path integral is

$$\langle \phi', t' | T[\hat{\phi}(X_i) \hat{\phi}(X_j)] | \phi, t \rangle = \int \mathcal{D}\phi \phi(X_i) \phi(X_j) e^{i \int d^4 X \mathcal{L}(\phi, \partial_\mu \phi)} \quad . \tag{1.30}$$

Here the time ordering operator  $T$  has been introduced because in (1.29) it follows from the definition of the path integral that  $t_i > t_j$ . The time ordering operator ensures that the field operator with the later time argument acts to the left state while the one with the earlier argument acts to the right:

$$T[\hat{\phi}(t_i) \hat{\phi}(t_j)] = \begin{cases} \hat{\phi}(t_i) \hat{\phi}(t_j) & \text{if } t_i > t_j \\ \hat{\phi}(t_j) \hat{\phi}(t_i) & \text{if } t_i < t_j \end{cases} \quad . \tag{1.31}$$

The vacuum state  $|0\rangle$ , which is required for the Feynman propagator, can be extracted from the eigenstates of the field operator by decomposition into eigenstates of the Hamilton operator  $\hat{H}|n\rangle = E_n|n\rangle$  :

$$|\phi, t\rangle = e^{i\hat{H}t} \sum_n |n\rangle \langle n | \phi, 0 \rangle = \sum_n e^{iE_n t} |n\rangle \langle n | \phi, 0 \rangle \quad , \tag{1.32}$$

where the time evolution operator (1.6) has been used. With this relation the matrix element (1.30) can be rewritten as

$$\begin{aligned}
\langle \phi', t' | T[\hat{\phi}(X_i) \hat{\phi}(X_j)] | \phi, t \rangle &= \sum_{n, n'} e^{-i(E_{n'} t' - E_n t)} \langle \phi', 0 | n' \rangle \langle n | \phi, 0 \rangle \\
&\times \langle n' | T[\hat{\phi}(X_i) \hat{\phi}(X_j)] | n \rangle \quad .
\end{aligned} \tag{1.33}$$

If  $n = n' = 0$  the second row is obviously the Feynman propagator which now has to be extracted from this expression. The idea is to let the time go to infinity. It will turn out that this limit favors the wanted vacuum contribution. Taking the limit  $t \rightarrow \infty$  does not help at first because the exponential function with the imaginary exponent oscillates undamped. However, if one adds an imaginary component to the time, the exponential function goes to zero asymptotically with increasing  $t$ . With the time coordinates rotated into the imaginary direction,  $\tau = e^{i\delta} t$  and  $\tau' = e^{i\delta} t'$ , the limit of the matrix element becomes

$$\begin{aligned}
\lim_{\substack{t' \rightarrow \infty \\ t \rightarrow -\infty}} \langle \phi', t' | T[\hat{\phi}(X_i) \hat{\phi}(X_j)] | \phi, t \rangle &= \lim_{\substack{\tau' \rightarrow e^{i\delta} \infty \\ \tau \rightarrow -e^{i\delta} \infty}} \langle \phi', e^{-i\delta} \tau' | T[\hat{\phi}(X_i) \hat{\phi}(X_j)] | \phi, e^{-i\delta} \tau \rangle \\
&\longrightarrow \lim_{\substack{\tau' \rightarrow \infty \\ \tau \rightarrow -\infty}} \langle \phi', e^{-i\delta} \tau' | T[\hat{\phi}(X_i) \hat{\phi}(X_j)] | \phi, e^{-i\delta} \tau \rangle .
\end{aligned} \tag{1.34}$$

The second row is an analytic continuation for  $\delta \rightarrow 0$  which is possible if the matrix element is analytic in  $t$  and  $t'$ . This method of rotating the time axis into the imaginary direction is known as *Wick rotation*. The angle of rotation does not play a role, but the task of extracting the vacuum contribution from the matrix element gets most simple if one chooses it to be  $\delta = \pi/2$ . Then the time gets purely imaginary, i.e.,  $t = -i\tau$ , where  $\tau$  is a real number. The matrix element becomes

$$\begin{aligned} \langle \phi', -i\tau' | T[\hat{\phi}(X_i)\hat{\phi}(X_j)] | \phi, -i\tau \rangle &= \sum_{n,n'} e^{-(E_{n'}\tau' - E_n\tau)} \langle \phi', 0 | n' \rangle \langle n | \phi, 0 \rangle \\ &\times \langle n' | T[\hat{\phi}(X_i)\hat{\phi}(X_j)] | n \rangle \quad . \end{aligned} \quad (1.35)$$

Unlike in (1.33) the exponential function in this expression does not oscillate anymore but drops as long as the exponent is negative. The rate of the decline is given by the energies  $E_n$ . Therefore, the summand with the lowest energy, which is the ground state, decreases most slowly and dominates for  $\tau \rightarrow \infty$ :

$$\begin{aligned} \langle \phi', -i\tau' | T[\hat{\phi}(X_i)\hat{\phi}(X_j)] | \phi, -i\tau \rangle &\rightarrow e^{-E_0(\tau' - \tau)} \langle \phi', 0 | 0 \rangle \langle 0 | \phi, 0 \rangle \\ &\times \langle 0 | T[\hat{\phi}(X_i)\hat{\phi}(X_j)] | 0 \rangle \quad . \end{aligned} \quad (1.36)$$

The pre-factor of the Feynman propagator in (1.36) is just the Feynman core in the limit of infinite times with a rotated time axis:

$$\begin{aligned} \langle \phi', -i\tau' | \phi, -i\tau \rangle &= \langle \phi', 0 | e^{-\tau'\hat{H}} e^{\tau\hat{H}} | \phi, 0 \rangle \\ &= \sum_{n,n'} \langle \phi', 0 | n' \rangle \langle n' | e^{(\tau - \tau')\hat{H}} | n \rangle \langle n | \phi, 0 \rangle \\ &= \sum_n \langle \phi', 0 | n \rangle \langle n | \phi, 0 \rangle e^{E_n(\tau - \tau')} \quad . \end{aligned} \quad (1.37)$$

Thus, the wanted Feynman propagator is the quotient of (1.36) and (1.37) in the limit of infinite times:

$$\langle 0 | T[\hat{\phi}(X_i)\hat{\phi}(X_j)] | 0 \rangle = \lim_{\substack{\tau' \rightarrow \infty \\ \tau \rightarrow -\infty}} \frac{\langle \phi', -i\tau' | T[\hat{\phi}(X_i)\hat{\phi}(X_j)] | \phi, -i\tau \rangle}{\langle \phi', -i\tau' | \phi, -i\tau \rangle} \quad . \quad (1.38)$$

Performing an analytic continuation back to real times and expressing the matrix element as well as the Feynman core in terms of path integrals one can write

$$\langle 0 | T[\hat{\phi}(X_i)\hat{\phi}(X_j)] | 0 \rangle = \lim_{\substack{t' \rightarrow \infty \\ t \rightarrow -\infty}} \frac{\int \mathcal{D}\phi \phi(X_i)\phi(X_j) e^{i \int d^4X \mathcal{L}(\phi, \dot{\phi})}}{\int \mathcal{D}\phi e^{i \int d^4X \mathcal{L}(\phi, \dot{\phi})}} \quad . \quad (1.39)$$

The extension to  $n$ -point functions is straightforward. Following the same ideas as above yields

$$\langle 0 | T[\hat{\phi}(X_1) \cdots \hat{\phi}(X_n)] | 0 \rangle = \lim_{\substack{t' \rightarrow \infty \\ t \rightarrow -\infty}} \frac{\int \mathcal{D}\phi \phi(X_1) \cdots \phi(X_n) e^{i \int d^4X \mathcal{L}(\phi, \dot{\phi})}}{\int \mathcal{D}\phi e^{i \int d^4X \mathcal{L}(\phi, \dot{\phi})}} \quad . \quad (1.40)$$

### The generating functional

To get a closer insight into the dynamics of quantum fields let us regard the behavior of the transition amplitude in the presence of a disturbance. This disturbance can be imagined as a classical external field which influences the evolution of the quantum field. In practice it will appear as an inhomogeneity in the equation of motion, so the previously homogeneous Lagrange equation becomes inhomogeneous. Within the Lagrangian this is achieved by an extra source term of the form  $J(X)\phi(X)$ . The way of calculating the path integral described above still holds, so the transition amplitude becomes

$$\langle \phi', t' | \phi, t \rangle_J = \mathcal{N} \int \mathcal{D}\phi e^{i \int_t^{t'} dt \int d^3x [\mathcal{L}(\phi, \partial_\mu \phi) + J\phi(X)]} . \quad (1.41)$$

Since one is not interested in the detailed effect of the disturbance on the state but just in the result after the disturbance is over, one considers the limits of infinite times  $t' \rightarrow +\infty$  and  $t \rightarrow -\infty$  and assumes the source to be switched on and off for large times (compare fig. 1.2)

$$\lim_{t \rightarrow \pm\infty} J(t) = 0 . \quad (1.42)$$

One can then insert a complete set of eigenstates at times  $t_1$  and  $t_2$  where the source term is assumed to vanish so (1.41) becomes

$$\langle \phi', t' | \phi, t \rangle_J = \lim_{M \rightarrow \infty} \prod_{l=1}^M \int d\phi_{l2} \int d\phi_{l1} \langle \phi'_l, t' | \phi_{l2} \rangle \langle \phi_{l2} | \phi_{l1} \rangle_J \langle \phi_{l1} | \phi_1, t \rangle , \quad (1.43)$$

where again space has been discretized the same way as in the derivation of the path integral. If one now expands the first and the last matrix element into eigenstates of the Hamilton operator one can use the same trick as in the derivation of the two-point function above. One lets time go to infinity after

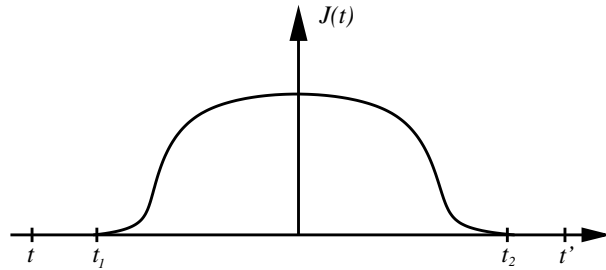


Figure 1.2: A possible evolution of the disturbing source term with time.

performing a Wick rotation (see (1.34)). Therefore only the vacuum contribution

survives and one can extract the transition amplitude from the vacuum to the vacuum, i. e., the probability that the vacuum is not affected by the disturbance

$$Z[J] = \langle 0|0 \rangle_J = \lim_{M \rightarrow \infty} \prod_{l=1}^M \int d\phi_{l2} \int d\phi_{l1} \langle 0|\phi_{l2} \rangle \langle \phi_{l2}|\phi_{l1} \rangle_J \langle \phi_{l1}|0 \rangle \quad . \quad (1.44)$$

In terms of path integrals this is analogous to (1.41)

$$Z[J] = \langle 0|0 \rangle_J = \mathcal{N} \int \mathcal{D}\phi e^{i \int_{-\infty}^{\infty} dt \int d^3x [\mathcal{L}(\phi, \partial_\mu \phi) + J\phi(X)]} \quad . \quad (1.45)$$

This is the *generating functional*. The normalization constant  $\mathcal{N}$  can be determined from the claim that the vacuum should be stable in absence of any disturbance, i. e., the amplitude should be  $Z[0] = 1$ .

The generating functional is of great importance in quantum field theory because it allows to calculate the  $n$ -point functions in a very convenient manner: The  $n$ -point function is just the  $n$ -th derivative of the generating functional with respect to the disturbing source:

$$\langle 0|T[\hat{\phi}(X_1) \cdots \hat{\phi}(X_n)]|0 \rangle = (-i)^n \frac{\delta^n Z[J]}{\delta J(X_1) \cdots \delta J(X_n)} \Big|_{J=0} \quad . \quad (1.46)$$

The physical value of the  $n$ -point function is given at vanishing source  $J = 0$ . The derivative is a *functional derivative* which is defined as follows:

$$\frac{\delta}{\delta J(X)} J(Y) = \delta^{(4)}(X - Y) \quad \text{or} \quad \frac{\delta}{\delta J(X)} \int d^4Y J(Y) \phi(Y) = \phi(X) \quad . \quad (1.47)$$

If the generating functional is known one can easily calculate all  $n$ -point functions by differentiation. Recall the meaning of the two-point function  $\langle 0|T(\hat{\phi}(X_1)\hat{\phi}(X_2))|0 \rangle$ . In (1.28) it has been stated that it is the Feynman propagator. In the special case that a particle does not interact this can be calculated exactly.

For illustration consider a free scalar field. Scalar fields are described by a Klein-Gordon Lagrangian

$$\mathcal{L}_{\text{KG}} = \frac{1}{2} (\partial_\mu \phi)^2 - \frac{1}{2} m^2 \phi^2 \quad . \quad (1.48)$$

The generating functional then reads

$$Z[J] = \int \mathcal{D}\phi \exp \left\{ i \int d^4X \left[ \frac{1}{2} (\partial_\mu \phi)^2 - \frac{1}{2} (m^2 - i\epsilon) \phi^2 + \phi J \right] \right\} \quad . \quad (1.49)$$

The additional term  $i\epsilon$  provides a Wick rotation to achieve the necessary damping as discussed below (1.33). For the first term in the exponent one can write

$$\int d^4X \partial_\mu \phi \partial^\mu \phi = - \int d^4X \phi \partial_\mu \partial^\mu \phi \quad , \quad (1.50)$$

which can be easily shown by using partial integration and assuming that the field vanishes at the boundaries. Thus the generating functional becomes

$$Z[J] = \int \mathcal{D}\phi \exp \left\{ -i \int d^4X \left[ \frac{1}{2} \phi \left( \partial_\mu \partial^\mu + m^2 - i\epsilon \right) \phi - \phi J \right] \right\} . \quad (1.51)$$

One can now decompose the field

$$\phi(X) \longrightarrow \phi(X) + \phi_0(X) \quad , \quad (1.52)$$

where  $\phi_0(X)$  obeys the inhomogenous Klein-Gordon equation

$$\left( \partial_\mu \partial^\mu + m^2 - i\epsilon \right) \phi_0(X) = J(X) \quad . \quad (1.53)$$

The Feynman propagator  $\Delta_F(X)$  is the solution to this equation if  $J(X)$  is a Dirac delta function (e.g. [GR96]). The solution to (1.53) is therefore

$$\phi_0(X) = - \int d^4Y \Delta_F(X - Y) J(Y) \quad . \quad (1.54)$$

Mathematically, the Feynman propagator is hence a *Green's function*. By using the fact that

$$\int d^4X \phi_0 \left( \partial_\mu \partial^\mu + m^2 - i\epsilon \right) \phi = \int d^4X \phi \left( \partial_\mu \partial^\mu + m^2 - i\epsilon \right) \phi_0 \quad , \quad (1.55)$$

one can insert the split field (1.52) into (1.51). The exponent of the generating functional then becomes

$$\begin{aligned} \int d^4X \left[ \frac{1}{2} \phi \left( \partial_\mu \partial^\mu + m^2 - i\epsilon \right) \phi - \phi J \right] &\longrightarrow \int d^4X \left[ \frac{1}{2} \phi \left( \partial_\mu \partial^\mu + m^2 - i\epsilon \right) \phi \right. \\ &\quad \left. + \phi \left( \partial_\mu \partial^\mu + m^2 - i\epsilon \right) \phi_0 + \frac{1}{2} \phi_0 \left( \partial_\mu \partial^\mu + m^2 - i\epsilon \right) \phi_0 - \phi J - \phi_0 J \right] . \end{aligned} \quad (1.56)$$

With the Klein-Gordon equation (1.53) some of these terms cancel each other, leaving only

$$\int d^4X \left[ \frac{1}{2} \phi \left( \partial_\mu \partial^\mu + m^2 - i\epsilon \right) \phi - \frac{1}{2} \phi_0 J \right] \quad . \quad (1.57)$$

If one now inserts the general solution (1.54) into this exponent the generating functional (1.51) becomes

$$\begin{aligned} Z[J] &= \int \mathcal{D}\phi \exp \left[ -\frac{i}{2} \int d^4X \phi \left( \partial_\mu \partial^\mu + m^2 - i\epsilon \right) \phi \right] \\ &\quad \times \exp \left[ -\frac{i}{2} \int \int d^4X d^4Y J(X) \Delta_F(X - Y) J(Y) \right] \quad . \end{aligned} \quad (1.58)$$

The generating functional now consists of two factors where the first one only depends on  $\phi$  and the second one only on the source  $J$ . The term including  $\phi$  is actually a number which one can call  $N$  so the generating functional becomes

$$Z[J] = N \exp \left[ -\frac{i}{2} \int \int d^4X d^4Y J(X) \Delta_F(X - Y) J(Y) \right] \quad . \quad (1.59)$$

Its second functional derivative in the sense of (1.46) is obviously the Feynman propagator

$$i\Delta_F(X - Y) = (-i)^2 \frac{\delta^2 Z[J]}{\delta J(X) \delta J(Y)} \Big|_{J=0} =: G^{(2)}(X, Y) \quad . \quad (1.60)$$

Note that for all uneven numbers of derivatives the Green's functions vanish because of the appearance of a factor  $J$  in front. Thus, the next non-vanishing Green's function is the 4-point function

$$\begin{aligned} G^{(4)}(X_1, X_2, X_3, X_4) &:= (-i)^4 \frac{\delta^4 Z[J]}{\delta J(X_1) \delta J(X_2) \delta J(X_3) \delta J(X_4)} \Big|_{J=0} \\ &= (-i)^4 [\Delta_F(X_1 - X_2) \Delta_F(X_3 - X_4) + \Delta_F(X_1 - X_3) \Delta_F(X_2 - X_4) \\ &\quad + \Delta_F(X_1 - X_4) \Delta_F(X_2 - X_3)] \quad . \quad (1.61) \end{aligned}$$

At this point it is useful to introduce Feynman graphs that provide a concise graphical notation for propagators. One associates a line with each of the Feynman propagators in (1.60) and (1.61). Then the Green's functions can be depicted as shown in fig. 1.3. The end points are identified with the space-time points  $X_i$ .

$$\begin{aligned} G^{(2)}(X_1, X_2) &= \text{---} \overline{\text{---}} \text{---} \\ G^{(4)}(X_1, X_2, X_3, X_4) &= \begin{array}{c} \text{---} \overline{\text{---}} \text{---} \\ \text{---} \overline{\text{---}} \text{---} \end{array} + \begin{array}{c} X_1 \\ | \\ X_3 \end{array} + \begin{array}{c} X_2 \\ | \\ X_4 \end{array} + \begin{array}{c} X_1 \quad X_2 \\ \diagdown \quad \diagup \\ X_3 \quad X_4 \end{array} \end{aligned}$$

Figure 1.3: Feynman diagrams for two- and four-point Green's functions.

The Feynman graphs of fig. 1.3 show the propagation of one and two particles between given space-time points, respectively. The fact that three summands occur in the four-point function means that the two propagating particles are indistinguishable. In general a  $2n$ -point function will be a sum of products of  $n$

two-point functions:

$$G^{(2n)}(X_1, \dots, X_{2n}) = \sum_{\text{all permutations}} G^{(2)}(X_{k_1}, X_{k_2}) \cdots G^{(2)}(X_{k_{2n-1}}, X_{k_{2n}}) \quad , \quad (1.62)$$

where the sum runs over all permutations of the indices  $x_k$  so that no summand appears twice. This identity is known as *Wick's theorem*. Obviously there is no new information added by the terms of the four-point interaction compared to the two-point function. Therefore, these diagrams can be reduced to the Feynman-propagator  $G^{(2)}(X_1, X_2)$ . To avoid these redundant contributions one can introduce the *generating functional for connected Green's functions*  $W$ . It is just the logarithm of the generating functional [Ryd96], i. e.

$$Z[J] = e^{iW[J]} \quad . \quad (1.63)$$

All connected Green's functions are calculated as the derivatives of the connected generating functional with respect to the source:

$$G_c^{(n)}(X_1, \dots, X_n) = i^{n-1} \frac{\delta^n W[J]}{\delta J(X_1) \cdots \delta J(X_n)} \Big|_{J=0} \quad . \quad (1.64)$$

In particular the first derivative is the expectation value of the field

$$\langle \phi(X) \rangle = \frac{\delta W[J]}{\delta J(X)} \Big|_{J=0} \equiv \hat{\phi} \quad . \quad (1.65)$$

At this point one can introduce the *effective action*. In general this is the Legendre transform of the generating functional for connected Vertex functions

$$\Gamma[\phi] = W[J] - \int d^4 X \phi(X) J(X) \quad . \quad (1.66)$$

With the effective action the expectation value of the field can be found as the solution of the *stationarity condition*

$$\frac{\delta \Gamma[\phi]}{\delta \phi(X)} \Big|_{\phi=\hat{\phi}} = 0 \quad . \quad (1.67)$$

Furthermore, the two-point vertex function is

$$\frac{\delta^2 \Gamma[\phi]}{\delta \phi(X_1) \delta \phi(X_2)} \Big|_{\phi=\hat{\phi}} = -G(X_1 - X_2) \quad . \quad (1.68)$$

The above presentation has been relatively simple because only non-interacting free particles have been considered. However, as soon as interactions are taken into account the generating functional becomes much more complicated. In general it is actually impossible to determine it exactly. Therefore, possibilities to approximate the generating functional have to be found.



## 1.3 Approximation schemes

As an example, consider the most simple case of an interacting theory where a scalar field only interacts with itself. The Lagrangian is

$$\mathcal{L} = \frac{1}{2}(\partial_\mu \phi)^2 - \frac{1}{2}m^2 \phi^2 - gV(\phi) \quad (1.69)$$

with the potential

$$V(\phi) = \frac{1}{4!}\phi^4 \quad . \quad (1.70)$$

Because of its potential the theory is called  $\phi^4$  theory. In the Feynman propagator not only lines, depicting free propagators as in fig. 1.3, appear now but also interactions of propagating fields. From the Lagrangian it follows that these interactions always occur with the fourth power in the fields. Thus one can draw interactions of propagators as crosses with four legs (see fig. 1.4).

Here, as in the following, we switch to momentum space and thus consider the

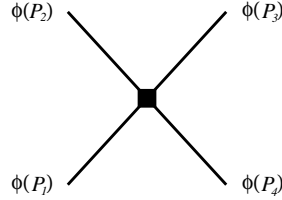


Figure 1.4: A quartic self-interaction vertex.

Fourier-transformed propagators:

$$\Delta_F(P) = \int d^4X e^{iP(X-Y)} \Delta_F(X-Y) \quad . \quad (1.71)$$

At every vertex momentum has to be conserved, so in more complex Feynman diagrams a vertex is associated with a Dirac delta function:

$$\text{Vertex} = -ig(2\pi^4)\delta^{(4)}\left(\sum p\right) \quad . \quad (1.72)$$

The main problem with the introduction of an interaction is that now the path integral cannot be calculated analytically as in the case of free propagation. However, one can think of different approximations to the actual value of the integral which are discussed in the following.

### 1.3.1 Perturbation expansion

Since the path integral of the free theory is known one can try to separate the interaction part from the free part of the path integral and approximate the former by a series expansion.

The Lagrangian is therefore

$$\mathcal{L} = \mathcal{L}_0 + \mathcal{L}_{\text{int}} \quad (1.73)$$

and the generating functional (1.45) becomes

$$\begin{aligned} Z[J] &= \mathcal{N} \int \mathcal{D}\phi \exp \left[ i \int d^4X (\mathcal{L}_0 + \mathcal{L}_{\text{int}} + J\phi) \right] \\ &= \mathcal{N} \int \mathcal{D}\phi \exp \left[ i \int d^4X (\mathcal{L}_0 + J\phi) \right] \exp \left[ -i \int d^4X gV(\phi) \right] . \end{aligned} \quad (1.74)$$

The first part is at most quadratic in the fields while the second part contains all interactions. One can now expand the second part in a power series and write the generating functional as

$$Z[J] = \mathcal{N} \int \mathcal{D}\phi \exp \left[ i \int d^4X (\mathcal{L}_0 + J\phi) \right] \sum_{l=0}^{\infty} \frac{1}{l!} \left[ -i \int d^4X gV(\phi) \right] . \quad (1.75)$$

Let us take a closer look at this expansion by considering Feynman diagrams. Obviously it is an expansion in powers of the coupling constant  $g$ . It is called *perturbation expansion*. It is convergent if the summand is smaller than one.

Vertices as shown in fig. 1.4 connect four legs with each other. In Feynman propagators (two-point functions) only two end points exist so the four-vertices can only contribute as loops, where two legs are connected. The most simple form of a loop is shown in fig. 1.5. This one-loop diagram contains one vertex so it

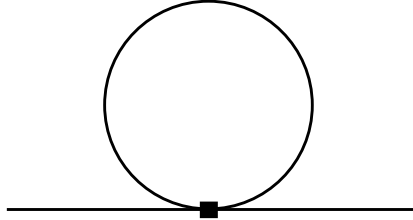


Figure 1.5: Connecting two legs of a vertex gives a one-loop diagram.

is proportional to the first power of the coupling constant  $g$ . Each propagator is associated with a momentum that is carried by the field. Because of momentum conservation it has to be the same at the end points of the propagation. However, the momentum that runs in a loop is not determined. Therefore one has to integrate over all possible momenta. Thus in momentum space a simple tadpole loop in a Feynman diagram is associated with

$$\text{Loop} = \int \frac{d^4P}{(2\pi)^4} \Delta_F(P) . \quad (1.76)$$

The perturbation series of the connected two-point function up to third order is shown diagrammatically in fig. 1.6 as an example. One can re-organize this

$$\begin{aligned}
G_c^{(2)} = & \text{---} + g \text{---} \bigcirc \text{---} + g^2 \left[ \text{---} \bigcirc \bigcirc \text{---} + \right. \\
& \left. \text{---} \bigcirc \bigcirc \text{---} + \text{---} \bigcirc \text{---} \right] + g^3 \left[ \text{---} \bigcirc \bigcirc \text{---} + \right. \\
& \left. \text{---} \bigcirc \bigcirc \bigcirc \text{---} + \text{---} \bigcirc \bigcirc \text{---} + \text{---} \bigcirc \bigcirc \bigcirc \text{---} \right] + O(g^4)
\end{aligned}$$

Figure 1.6: Perturbation series up to third order.

series by introducing the *self-energy*  $\Sigma$ . This self-energy contains the *one-particle irreducible* diagrams without external legs, i. e., those diagrams that do not fall apart when cutting one line. The new series now sorts the contributions according to their number of internal lines which are not part of a loop. In each term the non-loop propagators  $G_0$  are written down explicitly and the loops are summed up in the self-energy. The perturbation series then reads

$$G_c^{(2)}(P) = G_0(P) + G_0(P) \frac{\Sigma(P)}{i} G_0(P) + G_0(P) \frac{\Sigma(P)}{i} G_0(P) \frac{\Sigma(P)}{i} G_0(P) + \dots \quad (1.77)$$

with the self-energy which is shown in fig. 1.7. Obviously the terms in (1.77)

$$\frac{1}{i} \Sigma(P) = \text{---} \bigcirc \text{---} + \text{---} \bigcirc \bigcirc \text{---} + \dots \text{---} \bigcirc \text{---} \dots + \dots \text{---} \bigcirc \bigcirc \text{---} \dots + \dots$$

Figure 1.7: The one-particle irreducible loops in the self-energy.

are not of the same order in  $g$  anymore. Nevertheless, since all diagrams in the perturbation series can be expressed as a product of free propagators and the

self-energy, this expression is the same as in fig. 1.6. The series (1.77) is just a geometric series that can be calculated in a closed form:

$$\begin{aligned} G_c^{(2)}(P) &= G_0 \left( 1 + \frac{\Sigma(P)}{i} G_0 + \frac{\Sigma(P)}{i} G_0 \frac{\Sigma(P)}{i} G_0 + \dots \right) \\ &= G_0 \left( 1 - \frac{\Sigma(P)}{i} G_0 \right)^{-1} \\ &= \frac{i}{P^2 - m^2 - \Sigma(P)} \quad . \end{aligned} \quad (1.78)$$

The perturbation expansion is thus an approximation for two-point functions where each term is composed of free propagators. With this we can define the *two-point vertex function* as

$$\Gamma^{(2)}(P) = P^2 - m^2 - \Sigma(P) \quad . \quad (1.79)$$

### 1.3.2 The loop expansion

A different approximation scheme is the *loop expansion* which is an expansion in the number of loops [CW73, Jac74]. In the perturbation expansion the *two-point* function was assembled from contributions that have two external legs and all possible numbers of loops, which were summarized in the self-energy  $\Sigma$ . In the loop expansion not the two-point function (or a higher order vertex function) is approximated but the *effective action* (1.66). We can expand it in powers of momentum:

$$\Gamma[\phi] = \int d^4X \left[ -U[\phi(X)] + \frac{1}{2} (\partial_\mu \phi)^2 Z[\phi(X)] + \dots \right] \quad . \quad (1.80)$$

If we now assume the field to be constant in space and time

$$\phi(X) = \langle \phi \rangle = a \quad , \quad (1.81)$$

all derivative terms in (1.80) vanish and after evaluating the trivial volume integral one can write

$$\Gamma[a] = -\Omega U[a] \quad , \quad (1.82)$$

where  $\Omega$  is the space-time volume and  $U$  the *effective potential*. The effective action can also be expanded in powers of the field  $\phi$ :

$$\Gamma[\phi] = \sum_{n=0}^{\infty} \frac{1}{n!} \int d^4X_1 \dots \int d^4X_n \Gamma^{(n)}(X_1, \dots, X_n) \phi(X_1) \dots \phi(X_n) \quad , \quad (1.83)$$

or in momentum space

$$\Gamma[\phi] = \sum_{n=0}^{\infty} \frac{1}{n!} \int d^4P_1 \dots \int d^4P_n \delta^4(P_1 + \dots + P_n) \Gamma^{(n)}(P_1, \dots, P_n) \tilde{\phi}(P_1) \dots \tilde{\phi}(P_n) \quad . \quad (1.84)$$

Here,  $\Gamma^{(n)}$  is the  $n$ -point vertex function. The  $\tilde{\phi}$  in the above expression constitute the  $n$  external legs. Since the field has been assumed to be constant in space it is a Dirac delta function in momentum space:

$$\tilde{\phi}(P) = \int d^4X e^{-iPX} \phi(X) = a\delta^4(P) \quad . \quad (1.85)$$

Inserting this into (1.84) together with (1.82) yields for the effective potential

$$U[a] = - \sum_{n=0}^{\infty} \frac{1}{n!} a^n \Gamma^{(n)}(P_i = 0) \quad . \quad (1.86)$$

One can now introduce a parameter  $\alpha$  which multiplies the Lagrange density

$$\mathcal{L}(\phi, \partial_\mu \phi, \alpha) = \alpha^{-1} \mathcal{L}(\phi, \partial_\mu \phi) \quad . \quad (1.87)$$

The loop expansion is then equivalent to a power series in this constant  $\alpha$  which can be seen as follows. The power of  $\alpha$ , denoted by  $P$  in the following, is connected to the number of internal lines  $I$  of a diagram and the number of vertices  $V$  by

$$P = I - V \quad , \quad (1.88)$$

since the propagator is the inverse of the differential operator occurring in the Lagrangian and thus carries a factor of  $\alpha$ . Furthermore each vertex of course carries a factor of  $\alpha^{-1}$ .

Moreover, the number of loops  $L$  in a diagram is

$$L = I - V + 1 \quad , \quad (1.89)$$

because the number of loops is equal to the number of internal momenta that is integrated over. Each internal line contributes an integration over a momentum but each vertex corresponds to a Dirac delta function that reduces the number of momentum integrals by one. The  $+1$  is added for the extra delta function that assures overall momentum conservation. Comparing (1.88) and (1.89) gives

$$P = L - 1 \quad . \quad (1.90)$$

Therefore, an expansion in powers of  $\alpha$  is equivalent to an expansion in the number of momentum loops of the form

$$U[\phi] = U^{(0)}[\phi] + \sum_{n=1}^{\infty} U^{(n)}[\phi] \quad , \quad (1.91)$$

where  $n$  is the number of loops.

The main advantage of expanding the *effective potential* instead of the Green's function is that, according to (1.86), all  $n$ -point vertex functions are considered up to a certain number of loops. In other words all loop diagrams are equipped

with all possible numbers of external legs. The sum over these external legs in (1.86) can be calculated explicitly [CW73].

Let us illustrate the loop expansion for the case that only one loop is taken into account. The one-loop contribution to the effective potential is [Kug97]

$$U^{(1)} = \frac{1}{2} \int \frac{d^4 P}{(2\pi)^4} \ln D^{-1}(P; \phi) \quad . \quad (1.92)$$

Therefore the effective potential is up to first order

$$U(\phi) = U^{(0)}(\phi) + \frac{1}{2} \int \frac{d^4 P}{(2\pi)^4} \ln D^{-1}(P; \phi) \quad , \quad (1.93)$$

where the tree-level propagator, i.e., the propagator without any loops, is according to (1.68)

$$D^{-1}(X_1, X_2; \phi) \equiv - \left. \frac{\delta^2 U^{(0)}[\phi]}{\delta \phi(X_1) \delta \phi(X_2)} \right|_{\phi=\hat{\phi}} \quad . \quad (1.94)$$

### 1.3.3 The Cornwall-Jackiw-Tomboulis formalism

In the loop expansion the effective action is expanded in numbers of loops. However, it turns out that many phenomena cannot be described by only considering lower-order contributions of the loop expansion. In models with spontaneously broken symmetry, for example, the mass of certain particles becomes imaginary when calculated in the loop expansion [LR00]. Furthermore, the loop expansion is not necessarily convergent. Furnstahl et al. showed in 1989 that for the Walecka model the loop expansion does not converge at all up to two-loop order [FPS89]. Most importantly, the expansion schemes presented above fail at non-zero temperature as will be discussed in section 1.4.

Many of these problems can be solved by a different approximation scheme, the *CJT formalism* which was introduced by Cornwall, Jackiw and Tomboulis in 1974 [CJT74] and independently by Luttinger and Ward [LW60] and Baym and Grinstein [BG77] who called it  *$\Phi$  functional formalism*. Here, again the effective action is approximated, but this formalism now leads to a set of self-consistent Schwinger-Dyson equations which are solved by the propagators of the considered particles. These propagators are fully dressed, i.e., they contain diagrams of certain classes up to infinite order in loops.

In (1.41) a disturbing source term was introduced into the generating functional so arbitrary  $n$ -point functions could be calculated by taking the  $n$ th derivative with respect to this source (see (1.46)).

In the CJT formalism another source  $K(X, Y)$  is introduced so the generating

functional becomes <sup>2</sup>

$$\begin{aligned} Z[J, K] &= e^{W[J, K]} \\ &= \int \mathcal{D}\phi \exp \left\{ I[\phi] + \int_X \phi(X) J(X) + \frac{1}{2} \int_{X, Y} \phi(X) K(X, Y) \phi(Y) \right\} \quad , \end{aligned} \quad (1.95)$$

where  $I[\phi] = \int_X \mathcal{L}[\phi(X), \partial_\mu \phi(X)]$  is the classical action. The integration can be seen as the normal four-space integration at this point. In the next section we will expand this formalism to non-zero temperature by replacing the time integration by an integral over imaginary time. We use a notation that does not distinguish these cases.

Some approaches, known as *two-particle point-irreducible expansion schemes*, use a source  $K(X)$  which is local instead of bilocal as here [BM03]. This leads to a local self-energy where only loop corrections are taken into account which are independent of the external momentum. The propagators in these schemes therefore always describe quasi-particles without a width. Here only bilocal sources are considered.

As in the loop expansion the expectation value of the field is calculated as

$$\frac{\delta W[J, K]}{\delta J(X)} = \frac{1}{Z} \frac{\delta Z[J, K]}{\delta J(X)} \equiv \hat{\phi}(X) = \langle \phi \rangle \quad , \quad (1.96)$$

but furthermore the connected two-point function is now calculated by taking the derivative with respect to the additional source  $K$ :

$$\frac{\delta W[J, K]}{\delta K(X, Y)} = \frac{1}{Z} \frac{\delta Z[J, K]}{\delta K(X, Y)} \equiv \frac{1}{2} [G(X, Y) + \hat{\phi}(X) \hat{\phi}(Y)] \quad , \quad (1.97)$$

where

$$G(X, Y) := \frac{\delta^2 W[J, K]}{\delta J(X) \delta J(Y)} \quad . \quad (1.98)$$

The effective action is obtained by eliminating the sources  $J$  and  $K$  in favor of the physical quantities  $\hat{\phi}$  and  $G$  by a double Legendre transformation:

$$\begin{aligned} \Gamma[\hat{\phi}, G] &= W[J, K] - \int_X \hat{\phi}(X) J(X) \\ &\quad - \frac{1}{2} \int_{X, Y} \hat{\phi}(X) K(X, Y) \hat{\phi}(Y) - \frac{1}{2} \int_{X, Y} G(X, Y) K(X, Y) \quad . \end{aligned} \quad (1.99)$$

The stationarity conditions introduced in (1.67) are then

$$\begin{aligned} \frac{\delta \Gamma[\hat{\phi}, G]}{\delta \hat{\phi}(X)} &= -J(X) - \int_Y K(X, Y) \hat{\phi}(Y) \quad , \\ \frac{\delta \Gamma[\hat{\phi}, G]}{\delta G(X, Y)} &= -\frac{1}{2} K(X, Y) \quad . \end{aligned} \quad (1.100)$$

---

<sup>2</sup>This formalism is at non-zero temperature used in a convention where there is no imaginary unit in the exponent. We follow this convention in this section. Physics is not affected by this choice.

The expectation values of  $\hat{\phi}$  and  $G$  are defined at vanishing sources so the stationarity conditions become

$$\left. \frac{\delta \Gamma[\hat{\phi}, G]}{\delta \hat{\phi}(X)} \right|_{\hat{\phi}=\varphi, G=\mathcal{G}} = 0 \quad , \quad (1.101)$$

$$\left. \frac{\delta \Gamma[\hat{\phi}, G]}{\delta G(X, Y)} \right|_{\hat{\phi}=\varphi, G=\mathcal{G}} = 0 \quad . \quad (1.102)$$

While the first equation is the gap equation for the field, the second one is the Schwinger-Dyson equation for the propagator. Here  $\varphi$  and  $\mathcal{G}$  are the physical values of the field and the propagator, respectively. The task is now to find an explicit expression for the effective action  $\Gamma[\hat{\phi}, G]$ . Only the result shall be given here:

$$\Gamma[\hat{\phi}, G] = I(\hat{\phi}) - \frac{1}{2} \text{Tr}(\ln G^{-1}) - \frac{1}{2} \text{Tr}(\mathcal{D}^{-1} G - 1) + \Gamma_2[\hat{\phi}, G] \quad , \quad (1.103)$$

where  $\mathcal{D}^{-1}$  is the inverse tree-level propagator

$$\mathcal{D}^{-1}(X, Y; \hat{\phi}) \equiv - \frac{\delta^2 I[\phi]}{\delta \phi(X) \delta \phi(Y)} \Big|_{\phi=\hat{\phi}} \quad . \quad (1.104)$$

The detailed derivation can be found in [CJT74]. The different terms in (1.103) can be assigned to Feynman graphs with different irreducibility. The classical action  $I[\hat{\phi}]$  corresponds to the tree-level diagrams, i.e., lines without any loops. The second and third term represent the one-particle irreducible diagrams which do not fall apart when cutting only one line but do so when cutting two lines. The last term  $\Gamma_2$  is the sum over all two-particle irreducible (2PI) diagrams which cannot be separated by cutting two internal lines. In principle this term also contains all terms with higher irreducibility. As an approximation only some of these terms are actually taken into account.  $\Gamma_2$  is set up as follows:

- In the classical action  $I[\phi]$  the field  $\phi$  is shifted by its vacuum expectation value  $\hat{\phi}(X)$ , so  $\phi$  now accounts for the quantum fluctuations.
- The new action  $I[\phi + \hat{\phi}]$  contains terms of cubic or higher order in  $\phi$ . Those build an interaction part of the action  $I_{\text{int}}[\phi, \hat{\phi}]$ .
- $\Gamma_2[\hat{\phi}, G]$  is now the sum of all two-particle irreducible vacuum diagrams whose vertices are given by  $I_{\text{int}}[\phi, \hat{\phi}]$ .

In principle one can carry on with this and consider terms with even higher irreducibility (see for example [Car04, Ber04]). However, calculations become very complex then.



For constant fields  $\hat{\phi}(X) = \hat{\phi}$  and homogeneous systems one can, analogously to (1.80), derive an effective potential

$$V = -\frac{\Gamma[\hat{\phi}, G]}{\Omega} \quad , \quad (1.105)$$

where  $\Omega$  is the space-time volume of the system. Inserting the effective action (1.103) into this expression yields

$$V[\hat{\phi}, G] = U(\hat{\phi}) + \frac{1}{2} \int_K \ln G^{-1}(K) + \frac{1}{2} \int_K [\mathcal{D}^{-1}(K; \hat{\phi})G(K) - 1] + V_2[\hat{\phi}, G] \quad (1.106)$$

where  $U(\hat{\phi})$  is the classical potential. The momentum integral at zero temperature is just  $\int d^4K/(2\pi)^4$ . When temperature is introduced, the energy integral will be replaced by a Matsubara sum.

The inverse tree-level propagator can be written as

$$\mathcal{D}^{-1}(K; \hat{\phi}) = -K^2 + U''(\hat{\phi}) \quad . \quad (1.107)$$

Also the stationarity conditions (1.101) and (1.102) can be expressed in terms of the effective potential:

$$\begin{aligned} \left. \frac{\delta V[\hat{\phi}, G]}{\delta \hat{\phi}} \right|_{\hat{\phi}=\varphi, G=\mathcal{G}} &= 0 \quad , \\ \left. \frac{\delta V[\hat{\phi}, G]}{\delta G(K)} \right|_{\hat{\phi}=\varphi, G=\mathcal{G}} &= 0 \quad , \end{aligned} \quad (1.108)$$

where the second is equivalent to

$$\mathcal{G}^{-1}(K) = \mathcal{D}^{-1}(K; \hat{\phi}) + \Pi(K) \quad , \quad (1.109)$$

with the self-energy

$$\Pi(K) \equiv 2 \left. \frac{\delta V_2[\hat{\phi}, G]}{\delta G(K)} \right|_{\hat{\phi}=\varphi, G=\mathcal{G}} \quad . \quad (1.110)$$

The first equation is the field equation which is solved by the expectation value of the field. The second equation is the Schwinger-Dyson equation. Its solution is the fully dressed propagator. In general these equations are coupled, i.e. the field equations are also functions of the propagators and the Schwinger-Dyson equations are functions of the fields. In practice the solution is found numerically. One starts with the tree-level propagators and calculates the self-energies from these. With the self-energies new propagators can be set up which are now dressed with the diagrams considered in the self-energies. These are used to calculate new self-energies. In each step the dressing of the propagators is increased by one level. A solution is found if the results of two iterations do not differ any more. Physically spoken this means that higher-order contributions become too small to influence the result.

### The CJT formalism for fermions

The extension of the CJT formalism to fermions is straightforward [CJT74]. Just replace all factors of  $\frac{1}{2}$  by  $-1$  in the effective action (1.103) and the effective potential (1.106). The effective action becomes

$$\Gamma[\hat{\psi}, G] = I(\hat{\psi}) + \text{Tr}(\ln G^{-1}) + \text{Tr}(\mathcal{D}^{-1}G - 1) + \Gamma_2[\hat{\psi}, G] \quad (1.111)$$

and the effective potential becomes

$$V[\hat{\psi}, G] = U[\hat{\psi}] - \int_K \ln G^{-1}(K) - \int_K [\mathcal{D}^{-1}(K; \hat{\psi})G(K) - 1] + V_2[\hat{\psi}, G] \quad (1.112)$$

accordingly. The stationarity conditions for fermions read

$$\left. \frac{\delta V[\hat{\psi}, G]}{\delta \hat{\psi}} \right|_{\hat{\psi}=\psi, G=\mathcal{G}} = 0 \quad , \quad (1.113)$$

and the Schwinger-Dyson equation is

$$\mathcal{G}^{-1}(K) = \mathcal{D}^{-1}(K; \hat{\psi}) + \Sigma(K) \quad , \quad (1.114)$$

with the self-energy

$$\Sigma(K) \equiv - \left. \frac{\delta V_2[\hat{\psi}, G]}{\delta G(K)} \right|_{\hat{\psi}=\psi, G=\mathcal{G}} \quad . \quad (1.115)$$

## 1.4 Quantum field theory at non-zero temperature

Up to this point, quantum field theory has been formulated without accounting for temperature. However, the intention of this thesis is the investigation of particles at non-zero temperature. In this section we present the *imaginary time formalism* to implement temperature into the path integral technique.

The thermodynamic properties of a system in equilibrium are usually described in terms of the density matrix

$$\hat{\rho}(\beta) = e^{-\beta \hat{\mathcal{H}}} \quad (1.116)$$

and the partition function

$$Z(\beta) = \text{Tr} \rho(\beta) = \int d\phi_1 \langle \phi_1 | e^{-\beta \hat{\mathcal{H}}} | \phi_1 \rangle \quad , \quad (1.117)$$

where  $\hat{\mathcal{H}} = \hat{H} - \mu \hat{N}$  is the Hamiltonian for a grand canonical ensemble and  $\hat{\mathcal{H}} = \hat{H}$  for a canonical ensemble. Here  $\mu$  is the chemical potential,  $\hat{N}$  is the

number operator and  $\beta = 1/T$  is the inverse temperature. The trace operation in (1.117) can be written as an integration over all values of  $\phi_1$ . Comparing this partition function to the transition amplitude (1.26)

$$\langle \phi', t | \phi, 0 \rangle = \langle \phi', t | e^{-i\hat{H}t} | \phi, 0 \rangle = \mathcal{N} \int \mathcal{D}\phi \exp \left( i \int_0^t dt \int d^3x \mathcal{L} \right) \quad , \quad (1.118)$$

one observes a useful similarity. If one identifies

$$t = -i\beta \quad \text{with} \quad \beta = \frac{1}{T} \quad (1.119)$$

the transition amplitude becomes

$$\langle \phi', -i\beta | e^{-\beta \hat{H}} | \phi, 0 \rangle = \mathcal{N} \int \mathcal{D}\phi \exp \left( i \int_0^{-i\beta} d(-i\beta) \int d^3x \mathcal{L} \right) \quad . \quad (1.120)$$

We observe in (1.117) that  $\langle \phi', -i\beta | = \langle \phi, 0 |$  should hold for the identification to be possible so the field is periodic in imaginary time (anti-periodic for fermions). With the notation  $\tau = it$  the partition function is therefore

$$Z(\beta) = \mathcal{N} \int \mathcal{D}\phi \exp \left( - \int_0^\beta d\tau \int d^3x \mathcal{L} \right) \quad . \quad (1.121)$$

With the help of this identification temperature is introduced into the path integral formalism by replacing the time variable. An effective potential can be introduced for homogeneous systems as

$$V = -T \frac{\Gamma[\hat{\phi}, G]}{\mathcal{V}} \quad . \quad (1.122)$$

We have learned that the propagator is periodic in imaginary time (anti-periodic for fermions). A Fourier-transformation with respect to the imaginary time therefore only involves discrete frequencies:

$$\mathcal{G}_\beta(\tau) = \frac{1}{\beta} \sum_n e^{-i\omega_n \tau} \mathcal{G}_\beta(\omega_n) \quad . \quad (1.123)$$

Here  $\omega_n = n\pi T$  with  $n = 0, \pm 1, \pm 2, \dots$  are the so-called *Matsubara frequencies* [Mat55, Kap89]. For bosons only even frequencies contribute, that is  $\omega_n = 2n\pi T$ , while for fermions only the odd modes contribute  $\omega_n = (2n+1)\pi T$ . The sum is usually called *Matsubara sum*.

With the imaginary time formalism it is possible to introduce temperature in a very straightforward way. All expressions maintain their shape, just the time is replaced by the imaginary time and the energy is expressed in terms of a Matsubara frequency. The explicit evaluation of these sums will be shown later when it is done in this work.

However, the time dependence is abandoned, so only time-independent systems in equilibrium can be treated in this formalism. For dynamical calculations based on two-particle effective actions see for example [BS03].

It is worth mentioning that in general the standard perturbation expansion fails at non-zero temperature [Wei74, BP90a, BP90b] which poses a strong motivation for the use of resummation techniques. The reason is that the premise for the convergence of the perturbation expansion is a small coupling constant. At non-zero temperature, however, the temperature can compensate the small coupling constant so the convergence breaks down. An example calculation illustrating this for the simple  $\phi^4$  theory can be found in [CH98]. The Cornwall-Jackiw-Tomboulis formalism, used in this work, solves this problem, because it resums complete classes of diagrams with a certain power in temperature. A simple application within  $\phi^4$  theory can be found in [ACP93].

## 1.5 The standard model

We are now able to describe elementary particles within quantum field theories. But what particles are there? The current answer to this question is given by the *standard model of elementary particles*. The evolution of physics towards the standard model is another beautiful example of the course to simplicity and unification. In fact, the idea of fundamental objects was already followed by Anaximenes of Miletus in ancient Greece (around 850 b.c.) who tried to deduce all forms of matter from four elements, namely air, water, earth and fire. Although his concept was of course wrong, he thereby introduced the idea of elements constituting matter. This notion was followed further on. Real elements, effectively not divisible chemically, were observed in the following centuries and in 1869 Dimitri Mendeleev and Lothar Meyer found independently of each other that these elements show certain systematics when plotted against their atomic masses in the periodic table. Today the periodic table has 112 entries. However, these elements appeared not to be elementary. With further insight into the structure of matter it turned out that elementary particles, the atoms, exist that make up the different elements.

The knowledge that atoms exist certainly did not provide a further simplification in itself. There were as many different atoms as there were elements. But with further investigation the atoms soon revealed their own substructure. It emerged that all atoms are composed of negatively charged *electrons* orbiting a nucleus which consists of positively charged *protons* and neutral *neutrons*. Thus it was possible to think of matter being made up of only three constituents instead of the 112 elements.

Thorough investigation of protons and neutrons in collision experiments lead to the insight that they are able to transform into other particles, never before seen. More and more particles were discovered and in the end hundreds became

known. This was of course a grave setback for an integrative picture of matter but it emerged that some of the new particles were not elementary but could be considered composed from even more elementary particles, the quarks and anti-quarks.

Again, the attempt for unification was successful, eventually leading to the present-day picture of matter, the standard model of elementary particles. Table 1.1 gives a survey of particles in the standard model.

	Quarks			Leptons		
mass family	name	charge	spin	name	charge	spin
light	up	+2/3	1/2	electron	-1	1/2
	down	-1/3	1/2	electron neutrino	0	1/2
medium	strange	-1/3	1/2	muon	-1	1/2
	charm	+2/3	1/2	muon neutrino	0	1/2
heavy	beauty	-1/3	1/2	tau	-1	1/2
	truth	+2/3	1/2	tau neutrino	0	1/2

*Table 1.1: The three families of elementary particles in the standard model.*

Quarks are particles that experience the strong interaction, i.e. , they are hadrons, while leptons do not interact strongly. Quarks can never appear isolated so they always form heavier particles. Three quarks assemble a baryon, a proton or neutron for example, while a quark together with an anti-quark forms a meson. Leptons are only subject to electromagnetic and the weak interaction.

All these particles and their interactions can be described in quantum field theories. Thus, quantum field theory provides a unified framework that covers all forms of matter as well as the three interactions electromagnetic, weak and strong. Only gravity, the fourth interaction, could not yet be expressed in this theory but strong efforts are already being made to unify the theory of general relativity with quantum field theory.

In the following the theory of strong interaction which governs the properties and the behavior of quarks and gluons is briefly presented. It is the theory underlying the model used in this work. For an introduction to the quantum field theories of the other interactions see e.g. [HM84] and [PS95].

## 1.6 Quantum chromodynamics

As mentioned above, the discovery of the proton and the neutron was followed by the observation of more and more strongly interacting particles. It was the merit of Murray Gell-Mann to find the new principle underlying this particle zoo [GM62, GM64]. It arose from symmetry considerations which will be sketched in the following.

Let us assume we discover a number of particles in an experiment and arrange them according to their quantum numbers *hypercharge*  $Y$  and *isospin 3-component*  $I_3$  in a diagram. These quantum numbers seem rather artificial but they can be connected to observable quantities as

$$Y = B + S \quad (1.124)$$

where  $B$  is the baryon number and  $S$  the strangeness as well as

$$Q = I_3 + \frac{Y}{2} \quad (1.125)$$

where  $Q$  is the charge. The choice is historical but it exhibits the symmetries in a very lucid way.

Figure 1.8 shows these diagrams for baryons, baryon resonances and scalar mesons. Apparently, baryons form an octet, baryon resonances a decuplet and

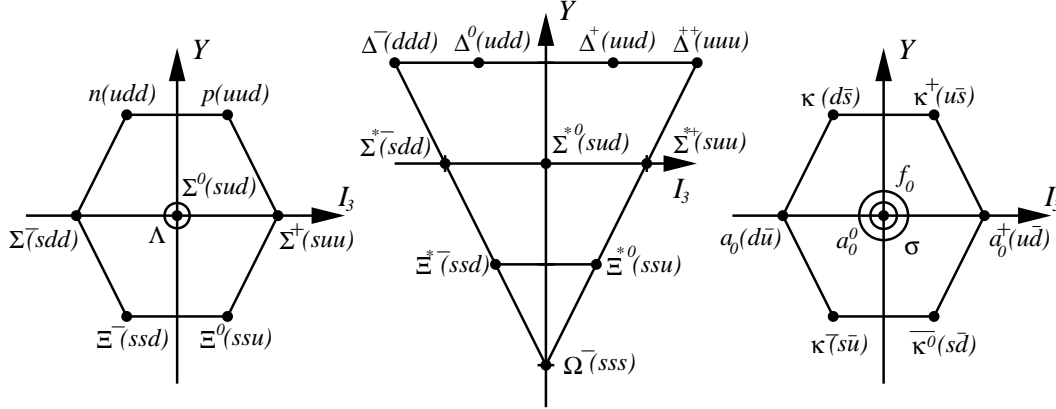


Figure 1.8:  $SU(3)$ -multiplets of baryons (left) baryon resonances (middle) and scalar mesons (right).

the scalar mesons form a nonet when plotted in  $Y - I_3$  space. All three diagrams shown here, as well as all other diagrams of this type which were found in experiments at that time, are multiplets of the group  $SU(3)$ . The fundamental representation of this group, that is the smallest multiplet of which all other multiplets can be assembled, is a triplet, shown in fig. 1.9.

The question arose as to whether these fundamental representations have a physical meaning, and indeed they have. It was possible to identify them with fundamental particles that compose the hadrons, namely the quarks and anti-quarks. Three types of each were sufficient to form all baryons and mesons known at that time: the up, down and strange quark as well as their anti-quarks. The family of quarks was not complete because three more quarks have been discovered since then (see tab. 1.1). The  $SU(3)$  therefore had to be extended to  $SU(6)$ , allowing

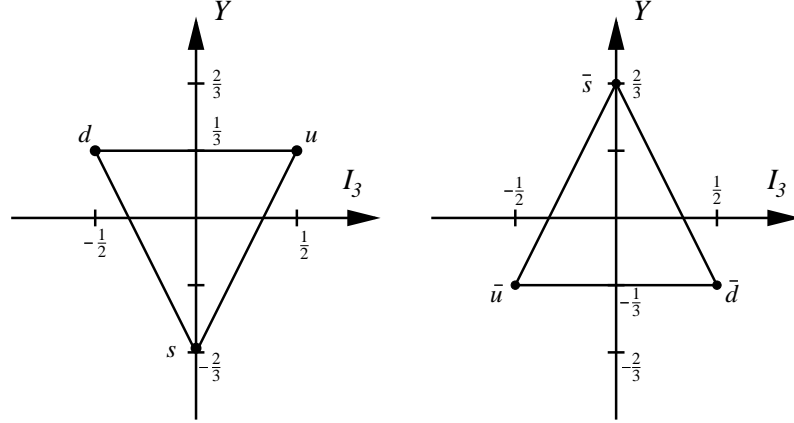


Figure 1.9: Fundamental quark (left) and anti-quark (right) representation of  $SU(3)$ .

for a lot of more multiplets and hadronic particles. The fundamental representations became sextets of six quarks and anti-quarks respectively. For a deeper coverage refer to [Gre05], for example.

We have learned that hadrons consist of quarks. What are the properties of quarks and how do they interact? To answer this question the first approach could be to fall back on something that is known as for example the theory of charged particles. Charged particles are described within quantum electrodynamics (QED) which is the quantum field-theoretical advancement of classical electrodynamics. However, QED is not capable to describe quarks as will be shown in the following.

Quarks are fermions with spin  $\frac{1}{2}$ , so like electrons they should be described by a Dirac Lagrangian. However, the interaction of quarks cannot be transferred from QED so easily. Consider the  $\Delta^{++}$  resonance in fig. 1.8, for example. Its spin  $3/2$  and its charge 2 are obtained by combining three up-quarks (compare table 1.1). Apparently these quarks are indistinguishable and therefore all in the same state although they are fermions. This obviously contradicts the Pauli principle. The conclusion is that there has to be another property which distinguishes the three quarks from each other. This property is called *color charge* and can adopt the values *red*, *green* and *blue*. The Lagrangian for quarks therefore has to carry an extra index counting the color:

$$\mathcal{L}_0 = \bar{q}_j(i\gamma_\mu\partial_\mu - m)q_j \quad . \quad (1.126)$$

In QED the interaction between charged particles is motivated by the fundamental principle of local gauge invariance: It is required that the electron field is invariant under local  $U(1)$  transformations which is an implication of the conserved electrical charge. The analogous requirement in QCD is the conservation of color charge which is a local  $SU(3)$  symmetry. Thus, the demand is that the

quark behavior, defined by the Lagrangian (1.126), is invariant under local  $SU(3)$  transformations

$$q(X) \longrightarrow e^{i\alpha_a(X)T_a}q(X) \quad . \quad (1.127)$$

In the following it is sufficient to consider the infinitesimal transformation

$$\begin{aligned} q(X) &\longrightarrow (1 + i\alpha_a(X)T_a)q(X) \quad , \\ \partial_\mu q(X) &\longrightarrow (1 + i\alpha_a(X)T_a)\partial_\mu q(X) + iT_a q(X)\partial_\mu \alpha_a(X) \quad . \end{aligned} \quad (1.128)$$

Here a summation over  $a = 1, \dots, 8$  is implied.  $T_a$  are the eight generators of  $SU(3)$  and  $\alpha_a$  are the group parameters. Simply inserting the transformed quark field (1.128) into the Lagrangian (1.126) shows that this is not invariant under local  $SU(3)$  transformations, so in its present form the theory does not fulfill the  $SU(3)$  symmetry.

In QED the symmetry can now be repaired by introducing a gauge field (the photon) and a covariant derivative. One could try to proceed in an analogous way in QCD by introducing eight gauge fields  $G_\mu^a$  that transform like the QED gauge field

$$G_\mu^a \longrightarrow G_\mu^a - \frac{1}{g}\partial_\mu \alpha_a \quad (1.129)$$

and defining a covariant derivative

$$D_\mu = \partial_\mu + igT_a G_\mu^a \quad . \quad (1.130)$$

The Lagrangian would then read

$$\mathcal{L} = \bar{q}(i\gamma^\mu \partial_\mu - m)q - g(\bar{q}\gamma^\mu T_a q)G_\mu^a \quad , \quad (1.131)$$

where  $g$  is a coupling constant. However, this expression is still not invariant under  $SU(3)$  transformation because the last term transforms like

$$\begin{aligned} (\bar{q}\gamma^\mu T_a q) &\longrightarrow (\bar{q}\gamma^\mu T_a q) + i\alpha_b \bar{q}\gamma^\mu (T_a T_b - T_b T_a)q \\ &= (\bar{q}\gamma^\mu T_a q) - f_{abc}\alpha_b (\bar{q}\gamma^\mu T_c q) \quad , \end{aligned} \quad (1.132)$$

where  $f_{abc}$  are the  $SU(3)$  structure constants. Apparently, the fact that the  $SU(3)$  generators  $T_a$  do not commute poses an extra problem compared to the abelian theory of QED where the  $U(1)$  generator is just the unit matrix. Nevertheless, gauge invariance can be established in QCD as well by modifying the transformation property of the gauge fields (1.129) as

$$G_\mu^a \longrightarrow G_\mu^a - \frac{1}{g}\partial_\mu \alpha_a - f_{abc}\alpha_b G_\mu^c \quad . \quad (1.133)$$

With this the Lagrangian (1.131) is indeed invariant under  $SU(3)$ . One just has to add a gauge invariant kinetic term for the gauge fields to get the complete description of quarks:

$$\mathcal{L} = \bar{q}(i\gamma^\mu \partial_\mu - m)q - g(\bar{q}\gamma^\mu T_a q)G_\mu^a - \frac{1}{4}G_{\mu\nu}^a G_a^{\mu\nu} \quad , \quad (1.134)$$



where

$$G_{\mu\nu}^a = \partial_\mu G_\nu^a - \partial_\nu G_\mu^a - gf_{abc}G_\mu^b G_\nu^c \quad (1.135)$$

is the field strength tensor. The  $G_\mu^a$  gauge fields of QCD are called *gluons* and like photons they are massless vector particles. In contrast to the photons in QED the gauge-invariance restoration results in a self-interaction term for the gluons, i.e., gluons are not color-charge neutral but interact with each other.

### Asymptotic freedom

Due to this gluon self-coupling the interaction between quarks is much more complicated than the electromagnetic interaction in QED. The difference is most obvious in a property called *running coupling constant*. If one considers the interaction of two electrons, for example, QED tells us that this is mediated by the exchange of a photon. The photon couples to electrons with a coupling constant which is identified with the charge, i.e., the constant  $g$  appearing in the above calculation is the electron charge  $e$  in QED. However, if one actually measures the interaction between two electrons the charge appears to be different. So the measured charge of an electron is different from the constant introduced in the gauge repairing procedure. It turns out that the reason for this is that the exchanged photon is not just a photon but also includes electron-positron creation-annihilation bubbles which lead to a slight increase of the measured coupling constant with higher momenta<sup>3</sup>. However, it remains small, so a perturbative expansion is still possible.

The analogon in QCD is the creation of quark anti-quark pairs that modifies the coupling constant  $g$  of the QCD Lagrangian. However, also the self-interaction of the gluons has to be considered here, leading to a much stronger momentum dependence. The running coupling constant of QCD is

$$\alpha_s(Q^2) = \frac{4\pi}{(11 - \frac{2}{3}n_f) \ln(Q^2/\Lambda^2)} \quad , \quad (1.136)$$

where  $Q$  is the momentum of the gluons,  $n_f$  is the number of quark flavors and  $\Lambda$  is the QCD scale parameter which is determined experimentally. Due to the

---

<sup>3</sup>This effect had already been known before QED was developed. The explanation, though, was different [BD98]: The Dirac equation predicts a continuum of electron states with negative energy. This implies that all electrons with positive energy should fall to the negative continuum and emit light. However, the electrons still exist so the conclusion had to be that the negative continuum is already filled up with electrons (called *Dirac sea*) so Pauli's principle restrains electrons with positive energy from decaying. If now an electron is brought into this Dirac sea (which essentially fills up the vacuum) it interacts electromagnetically with those occupying the Dirac sea. Thus its charge is screened partially due to polarization. Therefore, the *effective charge* should change if measured very close to the electron. This was indeed observed in the hydrogen atom where the *s*-wave states are slightly reduced compared to those with  $l \neq 0$  because they are very close to the nucleus. The term *vacuum polarization* is still used for the corresponding QED diagram.

self-interaction of gluons the running coupling constant of QCD has the opposite momentum dependence to that of QED, i.e., with increasing momentum and smaller distances the coupling gets weaker. This behavior is known as *asymptotic freedom* [GW73b, GW73a]. Furthermore, the momentum dependence is much more important in QCD because for small momenta and large distances the coupling constant gets too large for perturbation theory to be applicable. Perturbative QCD only works at very high momentum transfers (compared to the scale parameter  $\Lambda$ ), i.e., at very high temperatures or densities.

At low temperatures and densities different approaches have to be employed. Two main ideas are usually followed. The first one is to solve QCD on a discretized space-time lattice numerically, i.e., to calculate the grand partition function explicitly. This is a very fundamental approach but it requires a huge computing effort. Furthermore, it is problematic to calculate at non-zero chemical potentials. Only recently some progress has been made in this direction. For a review refer to [Kar02, LP03, Ris04].

Another way to deal with hadronic matter at low densities and temperatures are the so-called effective models of which one is applied in this work. These models exploit the fact that in the regions of interest quarks are well confined in baryons and mesons. So models can be developed which assume that the interaction between baryons is mediated by mesons, both having no substructure. The idea will be explained in more detail in section 1.7.

### 1.6.1 Phases of nuclear matter

Quantum chromodynamics describe the properties of quarks. It is therefore also the theory underlying the behavior of hadrons as well as nuclear matter which are composed of quarks. In fact, hadrons are the only mediator we have to obtain experimental insight into QCD (e.g. [BGSG99, ZGS<sup>+</sup>01]). Quarks themselves can not be measured in principle.

A summary of the bulk properties of nuclear matter is given by its phase diagram where the temperature is plotted against the chemical potential. Its essential features are shown in fig. 1.10 in the plane of temperature and chemical potential. For a free gas at zero temperature the chemical potential can be connected to the baryon density as

$$\rho_i = \gamma_i \int_0^{k_{F_i}} \frac{d^3k}{(2\pi)^3} = \gamma_i \frac{k_{F_i}^3}{6\pi^2} \quad , \quad (1.137)$$

where  $\gamma_i$  is the isospin degeneracy factor of the respective baryon species and  $k_{F_i}$  is the Fermi-momentum which can be calculated with help of the Einstein theorem as

$$k_{F_i} = \sqrt{\mu^2 - m_i^2} \quad . \quad (1.138)$$

The nuclear ground state is located at a quark chemical potential of  $\mu \simeq 308$  MeV and zero temperature. It corresponds to a baryon density of  $\rho_B \simeq 0.17 \text{ fm}^{-3}$

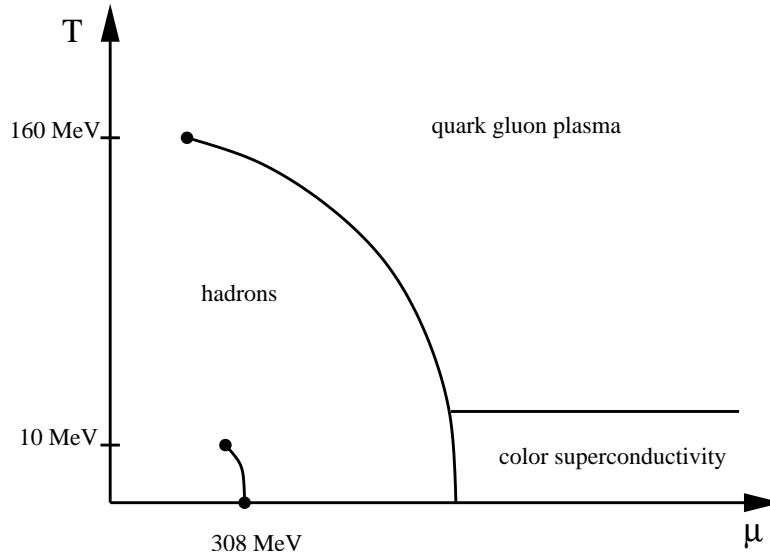


Figure 1.10: Schematic phase diagram of strongly interacting matter.

and a binding energy per nucleon of 16 MeV. The pressure in this state is  $p = 0$  because it is stable. For lower baryon densities one might expect that the pressure decreases below zero so the system would become mechanically unstable. However, this does not happen because the baryons form droplets. In a mixture of droplets and empty space a reduction of density only means that the distance between the droplets becomes larger while the pressure remains zero. Starting from a vapor of baryon droplets, increasing the density brings the droplets closer together until they finally overlap and build an analog to the condensation of water. This *liquid-gas phase transition* is of first order and occurs at the ground state density at  $T = 0$ . It extends to a temperature of around 10 MeV where it ends in a critical point. Physically spoken, with increasing temperature baryons start to evaporate from the droplets so the vapor phase on the left hand side of the phase transition line becomes a mixture of free baryons and droplets. At the critical point the phase boundary disappears and the phase transition becomes of second order.

The ground state of nuclear matter can be understood as the cancellation of an attractive and a repulsive force. Thus the phase transition can be reproduced in models that phenomenologically describe the nuclear force in this way as the *Walecka model* [SW86], for example, which will be introduced in detail in section 1.7.1. For the liquid-gas phase transition also refer to chapter 2.

In the previous section it has been shown that the interaction between quarks weakens at higher momenta and smaller distances, that is at higher temperatures or densities. Thus, one would expect the confinement between quarks to be influenced by this leading to a breakup of hadrons. This is indeed what most

calculations predict. At temperatures of the order of the scale parameter  $\Lambda$  collisions between hadrons start probing the quark structure. Similarly, at high densities the wave functions of hadrons begin to overlap. The phase transition between the hadronic state of matter and the so-called *quark-gluon plasma* in which quarks and gluons are no longer bound to hadrons is believed to be of first order up to a temperature of about 160 MeV. Here it ends in a critical point. At higher temperatures and lower chemical potentials it is expected to become of second order or a crossover.

Finally, the region of low temperatures and high chemical potentials should be mentioned. Here, most quarks are below the fermi surface while the running coupling constant is small because of the high densities. Therefore, the interaction of quarks is dominantly single-gluon exchange leading to the formation of Cooper pairs as in superconductivity in QED. This phase of matter could appear in the interior of neutron stars but it is unclear if their density is sufficient since the chemical potential there is only about 500 MeV.

## Experiments

In practice the phase diagram of nuclear matter is explored in heavy-ion collision experiments. The efforts started in Berkeley at energies of  $E_{\text{lab}} = 0.15 - 2$  AGeV as well as at the *Schwerionen-Synchrotron* (SIS) of the *Gesellschaft für Schwerionenforschung* (GSI) with  $E_{\text{lab}} = 1$  AGeV and the *Alternating Gradient Synchrotron* (AGS) at the Brookhaven National Laboratory providing energies of  $E_{\text{lab}} = 10.6 - 14.5$  AGeV. Here temperatures around 100 MeV and chemical potentials around 250 MeV could be reached. The *Super Proton Synchrotron* (SPS) accelerator at CERN with  $E_{\text{lab}} = 40 - 200$  AGeV followed.

The most recent experiment is the *Relativistic Heavy Ion Collider* (RHIC), which is a collider at Brookhaven that provides center of mass energies of  $E_{\text{cms}} = 100$  AGeV. It is able to probe the high-temperature region at low densities of the phase diagram. It is expected to reach temperatures of about 170 MeV. A similar aim is planned for the new *Large Hadron Collider* (LHC) at CERN. For the exploration of the high-density region at lower temperatures a new facility at GSI is planned.

## 1.7 Effective models

As shown above the running coupling constant of QCD becomes large at low temperatures and densities. Thus, a perturbation expansion in orders of the coupling constant is not convergent. Calculations of strongly interacting matter are therefore difficult in these regions. Some approaches have been mentioned in section 1.6. Here the use of *effective models* shall be reviewed in more detail.

Effective models are employed to model the strong interaction in a way that leads to observable results, that is to say parameters and interactions relevant in the

regime under consideration are taken into account. In the most definite way of driving an effective model is to start with the Lagrangian of QCD and to integrate out certain degrees of freedom until a model is left that is solvable, at least in an approximation scheme. A popular example for this is the *Nambu-Jona-Lasinio model* (*NJL model*) which has the same symmetry properties as QCD and describes quarks with a point-like interaction and a constant coupling strength. The NJL model has been widely applied for the investigation of quark properties (e.g. [SMMR01] study the chiral phase transition, in [ZW92] the time evolution of quarks is investigated using the CJT formalism. An example for an approach of calculating the quark spectral function at zero temperature similarly to this thesis is [FLM03b, FLM02].)

However, most effective models cannot be derived from QCD explicitly. A less stringent but nevertheless very successful way is to regard properties of QCD as for example its symmetries and construct a Lagrangian that reflects these properties. This procedure is widely used for hadronic effective models in which one exploits the fact that the running coupling constant becomes large at large distances. This means that at low temperatures and densities quarks are well confined into hadrons which can be viewed as interacting via the exchange of mesons.

One of the most important features of QCD that enters many effective models is probably *chiral symmetry* (see [Koc95] for a pedagogical introduction). It is a property of QCD at vanishing quark masses. Formally it is the invariance under vector and axial-vector transformations. In illustrative words chirality can be best understood by considering helicity which is the projection of the spin onto the spatial momentum vector. If a particle is massive it propagates with less than the speed of light and therefore a frame of reference can be found where the helicity of the particle changes because the momentum changes its sign. If in contrast the particle is massless it travels with the speed of light and this is not possible. A theory of massless particles is therefore chirally symmetric. It is expected that nuclear matter exhibits a phase transition at around  $T = 160$  MeV where chiral symmetry is restored because the current-quark mass vanishes.

A very popular effective model applied for the investigation of the chiral phase transition is the *linear sigma model* (e.g. [GML60, Lev67, Koc95]). This model incorporates chiral symmetry as a spontaneously broken symmetry which is restored in a phase transition at non-zero temperature and density. In its most simple form it includes a scalar  $\sigma$  and a pseudo scalar  $\pi$  meson which are chiral partners, which means that their masses become degenerate above the chiral phase transition [Pet99, LRSB00, RRR03]. The pion is a *Goldstone boson* which is massless in the phase of broken symmetry but adopts a non-zero mass in the restored symmetry phase. Normally, these models also include a small symmetry breaking term which leads to a small mass of the pion even in the phase of restored symmetry. It accounts for the realistic quark masses which are small but non-vanishing. Numerous extensions of the linear sigma model are used as well.

Worth mentioning among many others are the so-called "chiral  $\sigma$ - $\omega$  models" which include other mesons, in particular the vector  $\omega$  meson, and baryons [KM, NR76b, NR76a, MS82, Bog83b, Bog83a, JRK83, SC85, KMPB86, KMP87, BK89]. In the context of this work these models are particularly interesting because they pose a promising prospect for further investigations within the techniques developed here. It has been discussed in [FS93] that although some of these models are able to reproduce the empirical nuclear matter saturation point they all fail to describe properties of finite nuclei such as spin-orbit splittings, shell structure and charge densities. This could, among others, be achieved in [PZS<sup>+</sup>99, BPZ<sup>+</sup>02]. As an extension [ZPB<sup>+</sup>00, ZPS<sup>+</sup>01] include the SU(3) baryon octet, the baryon resonance decuplet and different kinds of mesons. The Walecka model used in this work stated a basis for these model.

Effective models do not necessarily have to be based on chiral symmetry. Hadronic models are known which describe nuclear interactions in terms of meson exchange modeling a phenomenological potential. In fact this idea is much older than the exact theory, QCD, itself. It was originated by Yukawa who was able to explain the short range of the strong interaction by introducing massive exchange particles [Yuk35] not considering any substructure. More advanced versions of such models are widely used today for the description of hadronic matter in the low-density and momentum regime (e.g. [Wal95]).

A very simple model of this kind in which baryons interact by the exchange of neutral scalar mesons was used by Schiff [Sch51]. It was improved by Johnson, Teller and Duerr [JT55, Due56] who introduced a scalar as well as a vector meson. It was possible to describe nuclear saturation and to reproduce the spin-orbit coupling in finite nuclei with the improved model. These attempts eventually led to the model of Walecka [Wal74] which was very successful in describing nuclear matter, finite nuclei and neutron stars and is still used and extended. A more detailed description will be given below. It should be noted that the coupling constants of the Walecka model are large so a perturbative expansion is not applicable. Most calculations for this model as well as its extensions are therefore done in the so-called *mean-field approximation* where fermions are treated as single-particle operators and bosons as classical fields. These calculations become increasingly valid for higher densities and were very successful in describing nuclear matter, neutron stars and finite nuclei. A detailed description and review can be found in [SW86, RRM<sup>+</sup>86, Rei89, GRT90, Ser92, SNR93, Wal95]. More recent progress in this direction is described in [FS00, SW97].

Other approaches use scattering data for the description of interactions. Here the nonrelativistic Schrödinger equation is used with a two-body potential which can be calculated from nucleon-nucleon interactions or is just obtained phenomenologically. However, perturbation theory is not convergent in this case, so alternative ways of modelling the interaction have to be applied. In particular replacing the bare nucleon-nucleon interaction with the Brückner G-Matrix has turned out to be successful [BLM54, Gol57]. Certain classes of linked diagrams are resummed



up to infinite order, here. However, it is not possible to describe the saturation energy and density for nuclear matter correctly within this ansatz. The reason is that the nucleon interaction is described in free space not considering effects from non-zero density. It is possible to reproduce these quantities within an improved ansatz with a density-dependent interaction, the Density-Dependent Hartree-Fock (DDHF) theory [Sky59]. This can furthermore describe the ground state properties of spherical nuclei and gives the correct ordering of single-particle levels.

The Brückner G-matrix theory has also been extended relativistically. The Relativistic Brückner-Hartree-Fock theory has been proposed by Shakin et al [ACPS83]. These authors used the Dirac equation for the description of the behavior of a single particle in matter with a scalar and a vector potential. The model successfully describes nuclear matter saturation properties as well as finite nuclei (for a review, see [BM96]). However, this approach does not account for the change of the particle properties in medium.

### 1.7.1 The Walecka model

The Walecka model was introduced by Walecka et al. in 1974 [Wal74, SW86] who called it Quantum Hadron Dynamics (QHD I). Originally it had been developed to describe finite nuclei and nuclear matter and incorporated baryons as well as scalar and vector mesons. The stability of the nucleus was achieved by an equilibrium between the attractive force provided by the scalar  $\sigma$  field and the repulsive force of the vector  $\omega$  field. There were two free parameters, namely the coupling constants of the two mesons to the baryons. In the original version, self-interactions of the mesons were not included.

In this work the Walecka model is used in a modified version where the scalar mesons couple to themselves in a quartic term to correct the large incompressibility of the original model [BB77]. Therefore, a new parameter  $\lambda$  is introduced. The Lagrangian of the model is

$$\begin{aligned} \mathcal{L} = & \bar{\psi} (i\gamma_\mu \partial^\mu - m_\psi - g_\sigma \sigma - g_\omega \gamma^\mu \omega_\mu) \psi + \frac{1}{2} \partial^\mu \sigma \partial_\mu \sigma - \frac{1}{2} m_\sigma^2 \sigma^2 \\ & - \lambda \sigma^4 + \frac{1}{2} m_\omega^2 \omega_\mu \omega^\mu - \frac{1}{4} (\partial_\mu \omega_\nu - \partial_\nu \omega_\mu) (\partial^\mu \omega^\nu - \partial^\nu \omega^\mu) \quad . \quad (1.139) \end{aligned}$$

Note that  $g_\sigma < 0$ ,  $g_\omega > 0$  and  $\lambda > 0$ . In this work I use the values  $g_\sigma = -7.197$ ,  $g_\omega = 7.557$  and  $\lambda = 35.56$ . The coupling constants  $g_\sigma$ ,  $g_\omega$  and  $\lambda$  of this model are large so a perturbative expansion is not applicable.

Usually the mean-field approximation is applied instead. For the use of this approximation within the Walecka model see [Wal74, SW86, SW97]. Other examples are [HS81], where pseudo scalar, pseudo vector mesons, and the photon are considered in addition to  $\sigma$  and  $\omega$  mesons, to investigate finite spherical nuclei.

Also self-consistent calculations have been done within the Walecka model. For example Mishra et al. calculated vacuum polarization effects [MPS<sup>+</sup>97] and hadron properties [MPG01] similarly to the first part of this work.

## 1.8 The intention of this work

In the early universe the temperature was high and the net baryon density was close to zero. In order to calculate properties of hadrons under these conditions the correct theory to apply after all would be quantum chromodynamics. However, if one considers a phase in which hadronic matter has already been formed, the running coupling constant of QCD is large so perturbation theory is not applicable (compare section 1.6). On the other hand, the particles can be regarded as being well separated by large distances so the quark structure is not resolved and a hadronic picture is sufficient as discussed in section 1.7.

In this work the hadronic framework applied is the Walecka model also known as *quantum hadrodynamics* (QHD I) as presented in section 1.7.1.

Within this framework the behavior of hadrons is formulated in terms of a quantum field theory in path integral quantization which has been introduced in section 1.2 at zero temperature and has been extended to non-zero temperatures within the imaginary time formalism in section 1.4.

Nuclear matter calculations at non-zero temperature are very common. However, they are normally carried out within the mean-field approximation [FS90, SW86, CW74, Wal95] or at one-loop level in the loop expansion [FS91, HS81]. A perturbative expansion is in general not convergent at non-zero temperature or large coupling constants, as discussed in section 1.4. Furthermore, Furnstahl et al. showed that also the loop expansion does not converge at two-loop order for the Walecka model [FPS89]. Also lattice calculations are not applicable because the Walecka model is not an asymptotically free theory.

In this work the method of choice is the *Cornwall-Jackiw-Tomboulis (CJT) formalism* as introduced in section 1.3.3. Here, a set of self-consistent Schwinger-Dyson equations is derived which is solved by the fully dressed propagators. It takes into account diagrams of certain types with up to an infinite number of loops. Some contributions have to be neglected nevertheless, but since certain classes of diagrams are completely included, every level of approximation is consistent and meaningful as discussed in section 1.3.3. The question of convergence is replaced by the demand that the Schwinger-Dyson equations are solvable.

Attempts have already been made to apply resummation techniques to nuclear matter calculations. For example Korpa et al. studied nucleon spectral functions in nuclear matter at zero temperature [KM93]. They were able to calculate nucleon spectral functions but only assumed the nucleon and the pion propagators to be dressed self-consistently. All other mesons were included only at mean-field level. Phat and Anh actually applied the CJT formalism to nuclear matter within



the Walecka model, albeit at zero temperature [PA97a, PA97b]. But again all mesons only enter with their free propagators which the authors conclude is eventually not sufficient. A non-zero width is not regarded. A similar investigation was done by Nakano et al. in the so called *nuclear Schwinger-Dyson formalism* [NHKK94, NMM<sup>+</sup>94] at zero temperature and non-zero density, where dressed meson propagators are taken into account. However, the authors use a decomposition of the fermion propagator into a free part and a density-dependent part which simplifies the calculations significantly but also poses the restriction that the fermions are quasi-particles. If one wants to consider non-zero width effects, this simplification is not useful.

Another work in this direction was done by Shu and Li who performed nuclear matter calculations within the CJT formalism at non-zero temperature [SL05]. They also considered the meson propagators to be the free ones and non-zero width effects were not regarded.

This work attempts to go beyond these approaches by performing calculations in which the nucleon propagator as well as all meson propagators are fully dressed. Therefore, self-consistent Schwinger-Dyson equations are set up for the nucleon and for all mesons. Two levels of approximation are employed. Both take into account two-particle irreducible diagrams in the effective potential (compare section 1.3.3). The first one is the so-called Hartree approximation where the only regarded two-particle irreducible diagram is the double-bubble diagram for the  $\sigma$  meson. Here all hadrons behave as quasi-particles, that is they have a well defined mass and zero decay-width. A similar work was done by Mishra et al. [MPG01]. In a second step I go beyond this approximation and include sunset diagrams as well. Here the problem is more complicated because now all hadrons acquire a non-zero decay width. Thus, a spectral function has to be introduced that accounts for decays at different energies. Furthermore, decompositions have to be found that project the Lorentz structure of the vector mesons and the Dirac structure of the fermions to achieve scalar quantities that can be solved for numerically. The result is a set of six coupled integral equations whose solutions are the spectral functions of the involved mesons and baryons. The solution is carried out on a discretized energy-momentum lattice. To avoid problems with the renormalization of the appearing integrals only the imaginary parts of the self-energies are taken into account.

Some work for mesonic models has been done in the direction of this thesis. Rupert et al. investigated the broadening of the  $\rho$  meson at non-zero temperature [RR05]. They used a  $\pi - \rho$  model inspired by vector meson dominance and calculated the meson spectral functions within the CJT formalism self-consistently, similar to this work. An analogous analysis was done in [vHK00] and [RK04], the latter also including baryons but neglecting anti-baryons and using a non-relativistic approximation for the meson-baryon coupling.

In addition, self-consistent 2PI resummation schemes have been widely applied for the investigation of the chiral phase transition within chiral effective models.

Some of these computations were done on Hartree level [Pet99, LRSB00, RRR03] while recently Röder et al. went beyond the Hartree approximation by including sunset diagrams [RRR05]. These authors could therefore also calculate spectral functions and investigate the effects of non-zero widths within  $O(N)$  models.

## –II–

# THE HARTREE APPROXIMATION

As a first step the influence of the most simple two-particle irreducible diagram, the double-bubble diagram (fig. 2.1, left), is discussed in this chapter. In the following this approximation is referred to as *Hartree approximation*.

The Hartree approximation is particularly simple because the Schwinger-Dyson equations (1.102) can be solved by a simple quasi-particle ansatz where the particles have well defined masses and no decay widths.

According to the procedure described in section 1.3.3, the first task is to extract the interaction part of the Walecka Lagrangian (1.139). Following the rules presented there, one obtains

$$\mathcal{L}_{\text{int}} = \bar{\Psi} g_{\sigma} \sigma \Psi + \bar{\Psi} g_{\omega} \gamma^{\mu} \omega_{\mu} \Psi + \lambda(\sigma^4 + 4\hat{\sigma}\sigma^3) \quad , \quad (2.1)$$

where the fields have been split into a fluctuation and a vacuum expectation value. The vacuum expectation value is denoted by a hat on the letter, that is  $\sigma \rightarrow \sigma + \hat{\sigma}$  and  $\omega_{\mu} \rightarrow \hat{\omega}_0$ . For the  $\omega$  meson the spatial components cancel in homogeneous, isotropic matter in the mean-field approximation so that only the time-component survives. Quartic terms in the fluctuations correspond to a four-point vertex as shown in the first diagram of fig. 2.1 while cubic terms lead to three-point vertices as depicted in the other three diagrams.

The Hartree approximation only considers the quartic  $\sigma$ -term of the interaction, so according to (1.106) in section 1.3.3 the effective potential is

$$\begin{aligned} V(\hat{\sigma}, \hat{\omega}) = U(\hat{\sigma}, \hat{\omega}) &+ \frac{1}{2} \int_K \ln G_{\sigma}^{-1} + \frac{1}{2} \int_K (\mathcal{D}_{\sigma}^{-1} G_{\sigma} - 1) \\ &+ \frac{1}{2} \int_K \ln G_{\omega}^{-1} + \frac{1}{2} \int_K (\mathcal{D}_{\omega}^{-1} G_{\omega} - 1) \\ &- \text{Tr} \int_K \ln G_{\Psi}^{-1} - \text{Tr} \int_K (\mathcal{D}_{\Psi}^{-1} G_{\Psi} - 1) \\ &+ 3\lambda \left( \int_K G_{\sigma} \right)^2 \quad . \end{aligned} \quad (2.2)$$

The last term corresponds to the double-bubble diagram. Since taking the derivative of the potential with respect to a propagator corresponds to cutting a line in

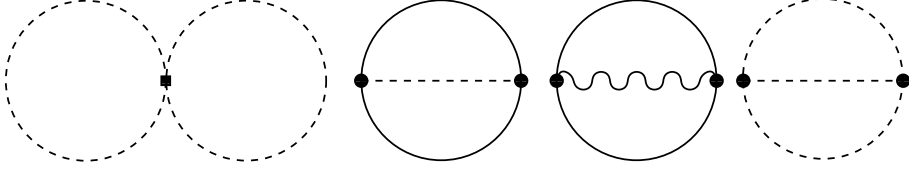


Figure 2.1: The two-particle irreducible diagrams which are considered in this thesis. Dashed lines represent  $\sigma$  propagators, wavy lines  $\omega$  propagators and full lines stand for fermion propagators.

diagrammatic language, the corresponding diagram in the self-energy is the tad-pole (fig. 2.2). The factor of three in this term counts the different possibilities to assemble the double-bubble diagram from a four-point vertex by connecting the four legs. To obtain this symmetry factor, number the lines meeting at the four-point vertex with 1 to 4. The three alternatives to build a double-bubble diagram are to join 1 and 2 as well as 3 and 4, to join 1 and 3, 2 and 4 and finally one can connect 1 with 4 and 2 with 3.

The inverse tree-level propagators read according to (1.104)

$$\begin{aligned}\mathcal{D}_\sigma^{-1} &= -(-m_\sigma^2 + K^2 - 12\lambda\hat{\sigma}^2) \quad , \\ \mathcal{D}_\omega^{-1} &= D_\omega^{-1} \quad , \\ \mathcal{D}_\Psi^{-1} &= D_\Psi^{-1} + g_\sigma\hat{\sigma} + g_\omega\gamma^\mu\hat{\omega}_\mu \quad ,\end{aligned}\tag{2.3}$$

where  $D_\omega$  and  $D_\Psi$  are the propagators of the free particles. The tree-level potential follows from the Lagrangian as

$$U(\hat{\sigma}, \hat{\omega}) = \frac{1}{2}m_\sigma^2\hat{\sigma}^2 + \lambda\hat{\sigma}^4 - \frac{1}{2}m_\omega^2\hat{\omega}^\mu\hat{\omega}_\mu \quad .\tag{2.4}$$

With (1.108) one obtains the following Schwinger-Dyson equations:

$$\begin{aligned}\mathcal{G}_\sigma^{-1}(K) &= \mathcal{D}_\sigma^{-1}(K) + 12\lambda \int_P \mathcal{G}_\sigma(P) \quad , \\ \mathcal{G}_\omega^{-1}(K) &= \mathcal{D}_\omega^{-1}(K) \quad , \\ \mathcal{G}_\Psi^{-1}(K) &= \mathcal{D}_\Psi^{-1}(K) \quad ,\end{aligned}\tag{2.5}$$

and the fields are found as the solution of the gap equations

$$\begin{aligned}0 &= m_\sigma^2\hat{\sigma} + 4\lambda\hat{\sigma}^3 + 12\lambda\hat{\sigma} \int_P \mathcal{G}_\sigma(P) - g_\sigma \int_P \text{Tr} \mathcal{G}_\Psi(P) \quad , \\ 0 &= -m_\omega^2\hat{\omega}_0 - g_\omega \int_K \text{Tr} \mathcal{G}_\Psi(P)\gamma_0 \quad ,\end{aligned}\tag{2.6}$$

where the mean-field approximation has been applied. Thus for the  $\omega$  meson only the time-component contributes. Equations (2.5) and (2.6) can be solved

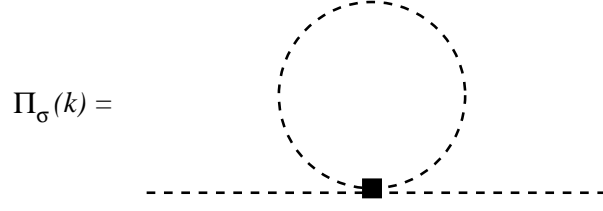


Figure 2.2: The tadpole-diagram which forms the  $\sigma$  meson self-energy in Hartree-approximation.

by an ansatz which assumes that the solutions have the general form of the free propagators but the masses are functions of  $T$  and  $\mu$ . This is possible because the self-energy of the  $\sigma$  meson in (2.5) does not depend on the external momentum. It therefore only contributes as a shift to the mass but does not provide a width in  $K$ . One can then solve the resulting equations for the masses. The same ansatz is used for the solution of the gap-equations (2.6). It is for the inverse  $\sigma$  meson propagator

$$\mathcal{G}_\sigma^{-1}(K) = -K^2 + M_\sigma^2 \quad (2.7)$$

and for the fermion propagator

$$\mathcal{G}_\psi^{-1}(K) = -\gamma_\mu K^\mu + M_\psi \quad . \quad (2.8)$$

Effective masses that are functions of temperature and chemical potential are denoted by capital letters. The  $\omega$  meson propagator is just the free propagator so its mass is that of the free particle. Solving these equations requires the calculation of the Matsubara sums. For the sake of clarity I evaluate the specific terms of the Schwinger-Dyson equations (2.5) and the field-equations (2.6) separately.

### The term $\int_P \mathcal{G}_\sigma$

From the ansatz (2.7) the boson propagator reads

$$\mathcal{G}_\sigma(K) = \frac{1}{-K^2 + M_\sigma^2} \quad , \quad (2.9)$$

so the  $\sigma$  loop to calculate reads

$$\int_P \mathcal{G}_\sigma(P) = \int \frac{d^3\mathbf{p}}{(2\pi)^3} T \sum_{n=-\infty}^{\infty} \mathcal{G}(k_0 = i\omega_n + \mu) \quad . \quad (2.10)$$

The actual calculation of the Matsubara sum follows a trick explained in [LB00]: If  $\mathcal{G}(k_0)$  is a meromorphic function of  $k_0$  which is regular on the vertical line  $\text{Re } k_0 = \mu$  and decreases faster than  $k_0^{-1}$  for  $|k_0| \rightarrow \infty$  one can express the Matsubara sum as an integral in the complex plane over a function whose residua

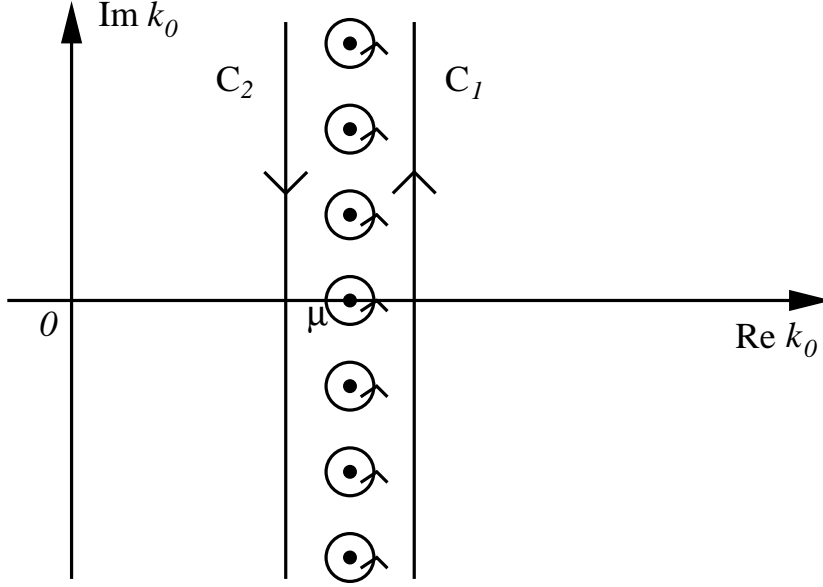


Figure 2.3: The integration contour for the calculation of Matsubara sums. The dots mark the poles of the cotangent.

are just the Matsubara frequencies. The integration contour is chosen to pick up the poles of this function (see fig. 2.3). Since contributions parallel to the real axis cancel each other one can choose the contour running along vertical lines from  $\mu + \eta - i\infty$  to  $\mu + \eta + i\infty$  ( $C_1$ ) and  $\mu - \eta + i\infty$  to  $\mu - \eta - i\infty$  ( $C_2$ ) where  $\eta \rightarrow 0^+$ . If one is able to calculate this integral it yields the value of the Matsubara sum. For bosons the wanted function is the hyperbolic cotangent so

$$\begin{aligned} T \sum_{n=-\infty}^{\infty} \mathcal{G}(k_0 = i\omega_n + \mu) &= \frac{1}{2} \int_{C_1 \cup C_2} \frac{dk_0}{i2\pi} \mathcal{G}(k_0) \coth\left(\frac{\beta(k_0 - \mu)}{2}\right) \\ &= -\frac{1}{2} \sum \text{Res } \mathcal{G}(k_0) \coth\left(\frac{\beta(k_0 - \mu)}{2}\right) . \end{aligned} \quad (2.11)$$

For the second step the contours have to be closed as semicircles to the left and the right, respectively. The residua of the propagator are  $1/(2E(M_\sigma))$  and  $-1/(2E(M_\sigma))$ . Since

$$\coth(x) = 1 + \frac{2}{e^{2x} - 1} , \quad (2.12)$$

For the meson field I restrict myself to the case  $\mu = 0$ . Therefore, the Matsubara sum reads

$$T \sum_{n=-\infty}^{\infty} \frac{1}{-K^2 + M_\sigma^2} = \frac{1}{E(M_\sigma)} \left( \frac{1}{\exp(E(M_\sigma)/T) - 1} + \frac{1}{2} \right) . \quad (2.13)$$

### The scalar density $\text{Tr} \int_P \mathcal{G}_\psi$

Before the Matsubara sum of this term can be calculated with the simple Ansätze (2.7) and (2.8) the inverse fermion propagator (2.8) has to be inverted. For the scalar  $\sigma$  meson the inversion is trivial. For the fermion the inverse propagator is known from (2.3) to be of the form

$$\mathcal{D}^{-1} = \gamma_\mu \ell^\mu + n, \quad (2.14)$$

where

$$\ell_0 = -p_0 + g_\omega \hat{\omega}_0 \quad (2.15)$$

is proportional to  $\gamma_0$ ,

$$\ell_i = -p_i \quad (2.16)$$

is proportional to  $\gamma_i$  and

$$n = m_\psi + g_\sigma \sigma = M_\psi \quad (2.17)$$

is proportional to the unit matrix. The inverse of this structure is just

$$\begin{aligned} (\gamma_\mu \ell^\mu + n)^{-1} &= [(\gamma_\mu \ell^\mu - n)(\gamma_\mu \ell^\mu + n)]^{-1}(\gamma_\mu \ell^\mu - n) \\ &= \frac{1}{(\ell^2 - n^2)}(\gamma_\mu \ell^\mu - n) \end{aligned} \quad (2.18)$$

which is therefore the fermion propagator. The trace over this propagator is

$$\begin{aligned} \text{Tr}(\gamma_\mu \ell^\mu + n)^{-1} &= \frac{1}{\ell^2 - n^2} \text{Tr}(\ell - n \mathbb{1}) = -2 \frac{4n}{\ell^2 - n^2} \\ &= -\frac{8M_\psi}{P^2 - M_\psi^2} \end{aligned} \quad (2.19)$$

where the factor of two that counts the isospin has been written down explicitly (The unit-matrix is an  $8 \times 8$  matrix.). An analogous trick as for  $\int_P \mathcal{G}_\sigma$  is now applied for the calculation of the Matsubara sums [LB00]. For fermions the function which provides the correct poles in the complex plane is the hyperbolic tangent. The full expression is

$$\int_P \mathcal{G}_\psi(P) = \int \frac{d^3 \mathbf{p}}{(2\pi)^3} T \sum_{n=-\infty}^{\infty} \mathcal{G}_\psi(iT(2n+1)\pi, \mathbf{p}) \quad (2.20)$$

Omitting the momentum integration one can write

$$\begin{aligned} T \sum_{n=-\infty}^{\infty} \mathcal{G}_\psi(p_0 = i\omega_n + \mu^*) &= \int_{C_1 \cup C_2} \frac{dp_0}{i4\pi} \mathcal{G}_\psi(p_0) \tanh \left( \frac{\beta(p_0 - \mu^*)}{2} \right) \\ &= -\frac{1}{2} \sum_{n=-\infty}^{\infty} \text{Res} \mathcal{G}_\psi(p_0) \tanh \left( \frac{\beta(p_0 - \mu^*)}{2} \right) \\ &= -\frac{1}{2} \sum_{n=-\infty}^{\infty} \text{Res} \mathcal{G}_\psi(p_0) \frac{e^{\beta(p_0 - \mu^*)} - 1}{e^{\beta(p_0 - \mu^*)} + 1} \\ &= -\frac{1}{2} \sum_{n=-\infty}^{\infty} \text{Res} \mathcal{G}_\psi(p_0) \left( \frac{1}{1 + e^{-\beta(p_0 - \mu^*)}} - \frac{1}{1 + e^{\beta(p_0 - \mu^*)}} \right) \end{aligned} \quad (2.21)$$

where the effective chemical potential  $\mu^* = \mu - g_\omega \hat{\omega}_0$  has been introduced. As before  $\omega_n$  are the Matsubara frequencies. The propagator is known from (2.19) to be

$$\mathcal{G}_\psi(p_0) = -\frac{8M_\psi}{P^2 - M_\psi^2} . \quad (2.22)$$

Its residua are

$$+4\frac{M_\psi}{\sqrt{\mathbf{p}^2 + M_\psi^2}} \quad \text{and} \quad -4\frac{M_\psi}{\sqrt{\mathbf{p}^2 + M_\psi^2}} , \quad (2.23)$$

so finally the Matsubara sum is

$$T \sum_{n=-\infty}^{\infty} \mathcal{G}_\psi(p_0 = i\omega_n + \mu^*) = -2\frac{M_\psi}{\sqrt{\mathbf{p}^2 + M_\psi^2}} (n(p_0) + \bar{n}(p_0) - n(-p_0) - \bar{n}(-p_0)) . \quad (2.24)$$

Here  $n$  and  $\bar{n}$  denote the distribution functions of fermions and anti-fermions respectively:

$$n(p_0) = \frac{1}{1 + e^{\beta(p_0 - \mu^*)}} \quad \text{and} \quad \bar{n}(p_0) = \frac{1}{1 + e^{\beta(p_0 + \mu^*)}} . \quad (2.25)$$

### The fermion density $\text{Tr} \int_P \gamma_0 \mathcal{G}_\psi$

As in the case of the scalar density above the inverse fermion propagator (2.8) has to be inverted for the calculation of this term. The procedure has been explained above but because of the additional  $\gamma_0$  the trace is different. With the definitions following (2.14) one obtains

$$\begin{aligned} \text{Tr}(\gamma_\mu \ell^\mu + n)^{-1} \gamma_0 &= \frac{1}{\ell^2 - n^2} \text{Tr}(\gamma_\mu \ell^\mu + n \mathbb{1}) \gamma_0 \\ &= \frac{1}{\ell^2 - n^2} \text{Tr}(-p_0 + g_\omega \hat{\omega}_0) \\ &= \frac{8}{\ell^2 - n^2} (-p_0 + g_\omega \hat{\omega}_0) . \end{aligned} \quad (2.26)$$

The argument of the trace could be reduced in the second line because an odd number of  $\gamma$  matrices is always traceless and  $\text{Tr}(\gamma_i \gamma_0) = 0$ . Now the same trick is applied as above. The residua of the propagator

$$\mathcal{G}_\psi(p_0) = -\frac{8p_0}{P^2 - M_\psi^2} \quad (2.27)$$

are both  $-4$  so the Matsubara sum finally becomes

$$\begin{aligned} \text{Tr} \int_P \gamma_0 \mathcal{G}_\psi(p_0, \mathbf{p}) &= -4 \left( \frac{1}{1 + e^{\beta(p_0 - \mu^*)}} - \frac{1}{1 + e^{\beta(p'_0 + \mu^*)}} \right) \\ &= -4 (n(p_0) - \bar{n}(p_0)) . \end{aligned} \quad (2.28)$$



Putting everything together and inserting the Ansätze into (2.5) and (2.6) yields the equations for the masses and the fields:

$$M_\sigma^2 = m_\sigma^2 + 12\lambda \left( \hat{\sigma}^2 + \int \frac{d^3\mathbf{p}}{(2\pi)^3} \frac{1}{E(M_\sigma)} \left\{ \frac{1}{\exp\left(\frac{E(M_\sigma)}{T}\right) - 1} + \frac{1}{2} \right\} \right), \quad (2.29)$$

$$M_\omega^2 = m_\omega^2, \quad (2.30)$$

$$M_\psi = m_\psi + g_\sigma \hat{\sigma}, \quad (2.31)$$

$$\begin{aligned} 0 = & m_\sigma^2 \hat{\sigma} + 4\lambda \hat{\sigma}^3 + 12\lambda \hat{\sigma} \int \frac{d^3\mathbf{p}}{(2\pi)^3} \frac{1}{E(M_\sigma)} \left\{ \frac{1}{\exp\left(\frac{E(M_\sigma)}{T}\right) - 1} + \frac{1}{2} \right\} \\ & + 4g_\sigma \int \frac{d^3\mathbf{p}}{(2\pi)^3} \frac{M_\psi}{E(M_\psi)} (n + \bar{n} - 1) \quad , \end{aligned} \quad (2.32)$$

$$0 = -m_\omega^2 \hat{\omega}_0 + 4g_\omega \int \frac{d^3\mathbf{p}}{(2\pi)^3} (n - \bar{n}) \quad . \quad (2.33)$$

Under the assumption of spherical symmetry the momentum integrals can be reduced to one-dimensional integrals. The above set of equations (2.29)–(2.33) is solved numerically for the masses and the expectation value of the  $\sigma$  field. The integrands in (2.29) and (2.32) contain additive constants  $\frac{1}{2}$  and 1. The corresponding integrals are divergent and thus omitted in the calculations. Actually the divergences would require thorough renormalization as done in [MPG01] but the effect is expected to be small. It should be kept in mind that this approach is still approximate and it is not the aim here to bring this rough ansatz to highest precision.

The parameters of the model were fitted to the properties of infinite nuclear matter as described in appendix B. I obtained the values  $g_\sigma = -7.197$ ,  $g_\omega = 7.557$  and  $\lambda = 35.56$ .

## 2.1 Results in Hartree approximation

Equations (2.29)–(2.33) are solved numerically for the masses and the fields. In this section the influence of the tadpole diagram on these quantities as well as the thermodynamical properties of nuclear matter are discussed. The results are compared to those of the theory on tree-level.

The only contribution of the tadpole-term is the integral term in the equation for the  $\sigma$ -meson mass (2.29). On *tree-level* this term is omitted while in *Hartree approximation* it is taken into account for the following investigation.

Accordingly, the most obvious difference between tree-level and Hartree-approximation is observed in the mass of the  $\sigma$  meson. It is up to 15-20 % higher in Hartree approximation at zero chemical potential than on tree-level as shown in fig. 2.4. At small temperatures the tadpole diagram does not affect the

results. With rising  $T$  its influence becomes stronger and reduces again at very high temperatures. This is because also the field equation of the  $\sigma$  meson (2.32) includes a temperature-dependent term similar to the one emerging from the tadpole diagram. However, it does not originate from the two-particle irreducible part of the potential and is therefore also present on tree-level. The influence of this term on the  $\sigma$  field increases with higher temperature. Because the  $\sigma$  field enters the mass equation, the  $\sigma$  mass is influenced as well and the relative effect of the tadpole diagram is reduced.

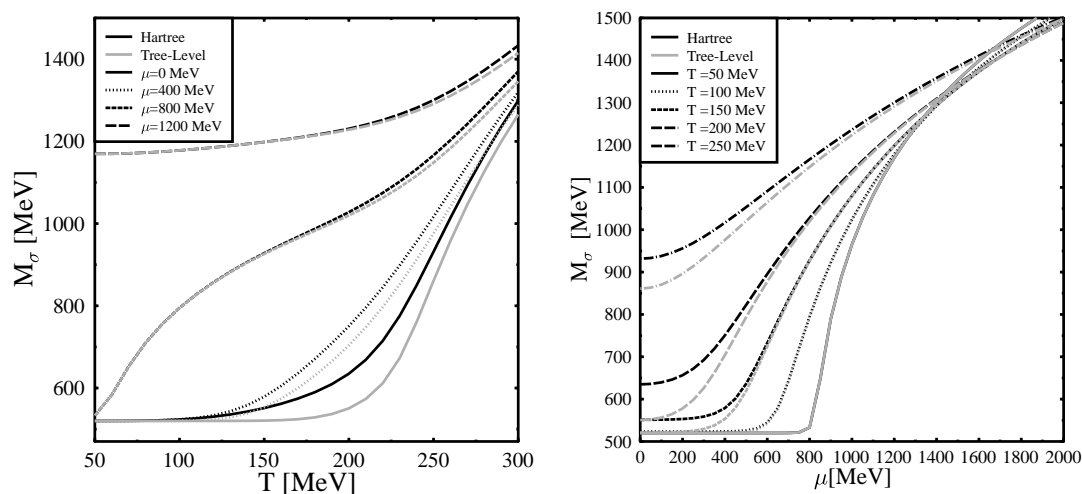


Figure 2.4: The mass of the  $\sigma$  field in Hartree approximation compared to tree-level approximation. At low temperatures the curves lie on top of each other so only the grey lines are visible.

The results strongly depend on the chemical potential. Only at zero chemical potential the influence of the tadpole diagram is significant. At higher  $\mu$  the temperature dependence is less pronounced and the correction term has less impact.

It should be noted that in models where the  $\sigma$  field is the chiral partner of a pseudoscalar meson, the  $\sigma$ -mass drops with increasing temperature and becomes degenerate with the mass of the pseudoscalar meson if explicit symmetry breaking is absent (e.g. [Pet99, LRSB00, RRR05]). This behavior is a consequence of the chiral symmetry restoration which is observed in these models. In the Walecka model, however, the  $\sigma$  meson plays a different role and chiral symmetry is absent. It turns out that the mass does not drop but rises with temperature.

The rise is too smooth to be associated with a phase transition.

However, at low temperatures the  $\sigma$  mass rises rapidly with increasing chemical potential.

Figure 2.5 shows the mass of the fermion as a function of temperature and chemical potential. Its behavior is directly connected to that of the  $\sigma$  field (see (2.31)) shown in fig. 2.6. With increasing temperature the mass of the fermion decreases. This behavior is triggered by the scalar density which is essentially the sum of the particle and the anti-particle number. A higher scalar density increases the  $\sigma$  field which on its part lowers the fermion mass. A lower fermion mass supports the creation of particle-anti-particle pairs which increases the scalar density. Here the transition is a smooth crossover. If, however, more baryon species are taken into account it becomes a first-order phase transition as shown in [WTM<sup>+</sup>87].

In the direction of the chemical potential the fermion mass drops very quickly in a narrow range of chemical potentials, as shown in the right-hand panels of figures 2.5 and 2.6. As above, the influence of the tadpole term is most pronounced at high temperatures and low chemical potentials. However, the difference between the two approximations is minor which is plausible because the tadpole term does not enter the  $\sigma$ -field strength directly but only via the  $\sigma$  mass. For non-zero chemical potentials the two approximations again differ even less.

It is a known behavior of the Walecka model that it shows a liquid-gas phase transition at temperatures below approximately  $T \simeq 25$  MeV (see for example [MPG01, PSS<sup>+</sup>97]) which leads to a step in the value of the  $\sigma$  field at around  $\mu = 923$  MeV. The temperatures in my calculation are too high to be in the region of this transition but the step is suggested here, although smoothed. The liquid-gas transition is not studied further in this context since the focus of this thesis lies on the high-temperature region where the influence of the higher-order diagrams is significant.

### 2.1.1 Thermodynamic properties

The thermodynamic properties of nuclear matter can be derived from the grand canonical potential  $\Omega$ . It is the effective potential (1.106) times the volume  $\mathcal{V}$ , evaluated at the physical values of the field and the propagators which are the solutions of eqns. (2.29)–(2.33).

$$\begin{aligned} \Omega[\hat{\sigma}, \hat{\omega}_0, \mathcal{G}_\sigma, \mathcal{G}_\omega, \mathcal{G}_\psi] &= V[\hat{\sigma}, \hat{\omega}_0, \mathcal{G}_\sigma, \mathcal{G}_\omega, \mathcal{G}_\psi] \cdot \mathcal{V} \\ &= \mathcal{V} \left[ \frac{1}{2} m_\sigma^2 \hat{\sigma}^2 + \lambda \hat{\sigma}^4 - \frac{1}{2} m_\omega^2 \hat{\omega}_0^2 + \frac{1}{2} \int_P \ln \mathcal{G}_\sigma^{-1} \right. \\ &\quad \left. + \frac{1}{2} \int_P [\mathcal{D}_\sigma^{-1} \mathcal{G}_\sigma - 1] + \frac{1}{2} \int_P \ln \mathcal{G}_\omega^{-1} - \text{Tr} \int_P \ln \mathcal{G}_\psi^{-1} \right] \end{aligned}$$

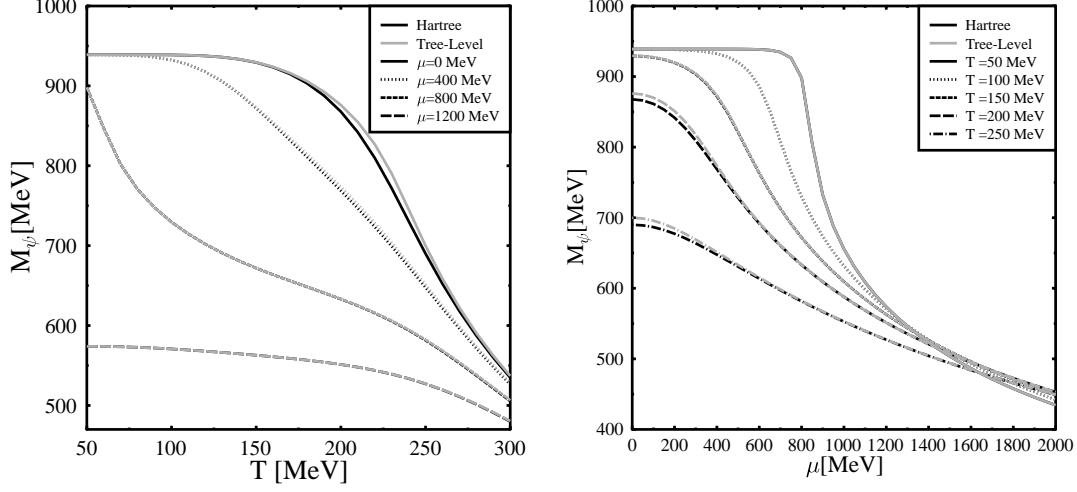


Figure 2.5: The mass of the fermion in Hartree approximation (black lines) and on tree-level (grey lines). At high chemical potentials in the left diagram and low temperatures in the right one the curves lie on top of each other so only the grey lines are visible.

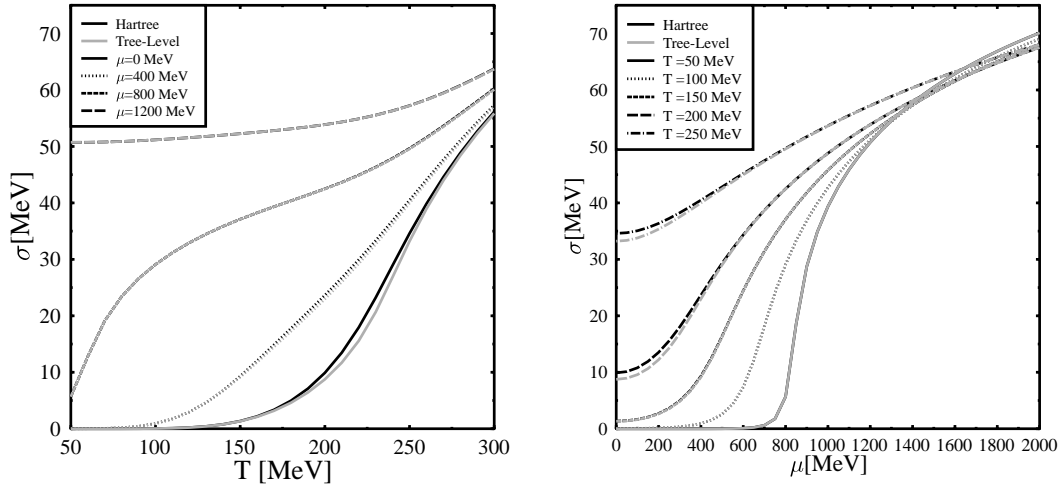


Figure 2.6: The  $\sigma$  field in Hartree approximation (black lines) and on tree-level (grey lines). At high chemical potentials in the left diagram and low temperatures in the right one the curves lie on top of each other so only the grey lines are visible.

$$+3\lambda \left[ \int_P \mathcal{G}_\sigma \right]^2 \quad . \quad (2.34)$$

Note that the terms containing  $\int_P [\mathcal{D}^{-1}\mathcal{G} - 1]$  vanish for the fermion and the  $\omega$  meson because their full propagator is the tree-level propagator. Beside the terms whose Matsubara sums were calculated above, two more sums have to be evaluated here. I show the calculation of each term separately.

**The term  $\int_P \ln \mathcal{G}_\sigma^{-1}$**

The calculation of the Matsubara sum in  $\int_P \ln \mathcal{G}_\sigma^{-1}$  follows an idea from [DJ74]. Assume the sum to be a function of the energy  $E$ . Then one can write

$$v(E) = \sum_{n=-\infty}^{\infty} \ln(-p_0^2 + \mathbf{p}^2 + M_\sigma^2) = \sum_{n=-\infty}^{\infty} \ln[4\pi^2 n^2 T^2 + E^2(M_\sigma)] \quad , \quad (2.35)$$

where as usual  $p_0 = i\omega_n = i2n\pi T$ . The trick is to consider the first derivative of this function with respect to the energy

$$\frac{\partial v(E)}{\partial E} = \sum_{n=-\infty}^{\infty} \frac{2E}{4\pi^2 n^2 T^2 + E^2} \quad . \quad (2.36)$$

It is known that

$$\sum_{n=1}^{\infty} \frac{y}{y^2 + n^2} = -\frac{1}{2y} + \frac{1}{2}\pi \coth \pi y \quad , \quad (2.37)$$

which is of the same form as (2.36) if one identifies  $y = E/(2\pi T)$ . The summation index enters squared so the negative part of the sum (2.36) gives a factor of two and the term  $n = 0$  has to be added by hand. Using the relation

$$\coth \left( \frac{\beta E}{2} \right) = \frac{e^{\beta E} - 1 + 2}{e^{\beta E} - 1} = 1 + \frac{2}{e^{\beta E} - 1} \quad , \quad (2.38)$$

the derivative of  $v(E)$  is therefore

$$\frac{\partial v(E)}{\partial E} = 2\beta \left( \frac{1}{2} + \frac{1}{e^{\beta E} - 1} \right) \quad . \quad (2.39)$$

The original function  $v(E)$  with the sum evaluated is now obtained by integrating over  $E$ . The final result is

$$\int_P \ln(-P^2 + M_\sigma^2) = \int \frac{d^3\mathbf{p}}{(2\pi)^3} \frac{E(M_\sigma)}{2} + \int \frac{d^3\mathbf{p}}{(2\pi)^3} T \ln(1 - \exp(-\beta E)) \quad . \quad (2.40)$$

The first term on the right-hand side is obviously divergent but it vanishes in all physical quantities which are derivatives of the grand canonical potential. The respective term for the vector mesons is calculated analogously but with a factor of three in front [RG94].

**The term**  $\int_P (\mathcal{D}_\sigma^{-1} \mathcal{G}_\sigma - 1)$

The calculation of this Matsubara sum can be reduced to the case of a single propagator with an effective mass which has been described above:

$$\begin{aligned}
\frac{1}{2} \int_P (\mathcal{D}_\sigma^{-1} \mathcal{G}_\sigma - 1) &= \frac{1}{2} \int_P [(m_\sigma^2 - P^2 + 12\lambda\hat{\sigma}^2) \mathcal{G}_\sigma - 1] \\
&= \frac{1}{2} \left[ \int_P (m_\sigma^2 + 12\lambda\hat{\sigma}^2) \mathcal{G}_\sigma + \int_P (-P^2 \mathcal{G}_\sigma - 1) \right] \\
&= \frac{1}{2} \left[ \int_P (m_\sigma^2 + 12\lambda\hat{\sigma}^2) \mathcal{G}_\sigma + \int_P \left( -\frac{P^2}{-P^2 + M_\sigma^2} - 1 \right) \right] \\
&= \frac{1}{2} \int_P (-M_\sigma^2 + m_\sigma^2 + 12\lambda\hat{\sigma}^2) \mathcal{G}_\sigma \\
&= \frac{1}{2} (-M_\sigma^2 + m_\sigma^2 + 12\lambda\hat{\sigma}^2) \int_P \frac{1}{-P^2 + M_\sigma^2} \quad . \quad (2.41)
\end{aligned}$$

This Matsubara sum has already been calculated above. The final result is

$$\begin{aligned}
\frac{1}{2} \int_P (\mathcal{D}_\sigma^{-1} \mathcal{G}_\sigma - 1) &= \frac{1}{2} (-M_\sigma^2 + m_\sigma^2 + 12\lambda\hat{\sigma}^2) \\
&\times \int \frac{d^3 \mathbf{p}}{(2\pi)^3} \frac{1}{E(M_\sigma)} \left( \frac{1}{\exp(E(M_\sigma)/T) - 1} + \frac{1}{2} \right) \quad . \quad (2.42)
\end{aligned}$$

**The term**  $\text{Tr} \int_P \ln \mathcal{G}_\psi^{-1}(P)$

For the calculation of this term I apply the relation

$$\text{Tr} \ln D = \ln \det D \quad . \quad (2.43)$$

With this one obtains

$$\begin{aligned}
\text{Tr} \int_P \ln \mathcal{G}_\psi^{-1} &= \text{Tr} \int_P \ln (-P_\mu \gamma^\mu + M_\psi) \\
&= \int_P \ln \det (-P_\mu \gamma^\mu + M_\psi) \\
&= 4 \int_P \ln (-P^2 + M_\psi^2) \\
&= 4T \sum_n \int \frac{d^3 \mathbf{p}}{(2\pi)^3} \ln (-(i\omega_n^F + \mu)^2 + E(M_\psi)^2) \\
&= 2T \sum_n \int \frac{d^3 \mathbf{p}}{(2\pi)^3} \left[ \ln(\omega_n^{F2} + (E(M_\psi) - \mu)^2) \right. \\
&\quad \left. + \ln(\omega_n^{F2} + (E(M_\psi) + \mu)^2) \right] \quad , \quad (2.44)
\end{aligned}$$

where  $\omega_n^F = (2n+1)\pi T$  are the fermionic Matsubara frequencies that enter for the energy component of the momentum. The energy is  $E(M_\psi) = \sqrt{\mathbf{p}^2 + M_\psi^2}$ . In

the last step it has been used that the sum runs over positive as well as negative frequencies. I now apply the general relation

$$\ln(a^2 + b^2) = \int_1^{b^2} \frac{1}{a^2 + \Theta^2} d\Theta^2 + \ln(1 + a^2) \quad (2.45)$$

on the two terms in the last line of (2.44). With this the Matsubara sum can be carried out using the general summation formula

$$\sum_{n=-\infty}^{\infty} \frac{1}{(n-x)(n-y)} = \frac{\pi(\cot \pi x - \cot \pi y)}{y-x} \quad (2.46)$$

The summation is performed for the two terms separately so one obtains

$$\sum_{n=-\infty}^{\infty} \frac{1}{(2n+1)^2 T^2 \pi^2 + \Theta^2} = \frac{1}{\Theta} \left( \frac{1}{2} - \frac{1}{e^{\Theta} + 1} \right) \quad (2.47)$$

Performing the  $\Theta$  integration and dropping the divergent contributions one obtains

$$\begin{aligned} \text{Tr} \int_Q \ln \mathcal{G}_{\psi}^{-1} = & \\ & 4 \int \frac{d^3 \mathbf{p}}{(2\pi)^3} T \left[ \ln \left( 1 + \exp \left( -\frac{E(M_{\psi}) - \mu}{T} \right) \right) + \ln \left( 1 + \exp \left( -\frac{E(M_{\psi}) + \mu}{T} \right) \right) \right] \quad (2.48) \end{aligned}$$

### The grand canonical potential

Putting all terms together we obtain the final result for the grand canonical potential:

$$\begin{aligned} \Omega[\hat{\sigma}, \hat{\omega}_0, M_{\sigma}, M_{\omega}, M_{\psi}] = & \mathcal{V} \left\{ \frac{1}{2} m_{\sigma}^2 \hat{\sigma}^2 + \lambda \hat{\sigma}^4 - \frac{1}{2} m_{\omega}^2 \hat{\omega}_0^2 \right. \\ & + \int \frac{d^3 \mathbf{p}}{(2\pi)^3} T \ln \left( 1 - \exp \left( -\frac{E(M_{\sigma})}{T} \right) \right) \\ & + \frac{1}{2} (-M_{\sigma}^2 + m_{\sigma}^2 + 12\lambda \hat{\sigma}^2) \int \frac{d^3 \mathbf{p}}{(2\pi)^3} \frac{1}{E(M_{\sigma})} \left( \frac{1}{\exp \left( \frac{E(M_{\sigma})}{T} \right) - 1} \right) \\ & + 3 \int \frac{d^3 \mathbf{p}}{(2\pi)^3} T \ln \left( 1 - \exp \left( -\frac{E(M_{\omega})}{T} \right) \right) \\ & - 4 \int \frac{d^3 \mathbf{p}}{(2\pi)^3} T \left[ \ln \left( 1 + \exp \left( -\frac{E(M_{\psi}) - \mu}{T} \right) \right) + \ln \left( 1 + \exp \left( -\frac{E(M_{\psi}) + \mu}{T} \right) \right) \right] \\ & \left. + 3\lambda \left[ \int \frac{d^3 \mathbf{p}}{(2\pi)^3} \frac{1}{E(M_{\sigma})} \left( \frac{1}{\exp \left( \frac{E(M_{\sigma})}{T} \right) - 1} \right) \right]^2 \right\} \quad (2.49) \end{aligned}$$

where  $E(M) = \sqrt{\mathbf{p}^2 + M^2}$ .

Figure 2.7 shows on the right-hand side the equation of state in terms of pressure as a function of fermion density in Hartree approximation and on tree-level. The pressure is derived from the grand canonical potential as

$$p = -\frac{\Omega}{\mathcal{V}} \quad . \quad (2.50)$$

The influence of the tadpole term is only very small. All lines lie on top of each other for all temperatures and densities. The maximal deviation of around 2-3 % is observed very low densities and a temperature of 200 MeV which is consistent with the above observations. The left plot of fig. 2.8 highlights this. It should be emphasized that in both calculations the quartic self-interaction of the  $\sigma$  field is present. If one switches off this term by setting the coupling constant  $\lambda$  to zero one obtains an equation of state that is stiffer in the temperature direction. That is, the pressure rises more quickly with temperature at a given density as compared to the case where the self-interaction is present.

Also the entropy density, shown on the right hand side of fig. 2.7, can be derived from the grand canonical potential as

$$S = -\frac{\partial \Omega}{\partial T} \quad . \quad (2.51)$$

As the pressure it only varies very slightly with the inclusion of the tadpole diagram. The maximal difference of around 2 % is again observed at 200 MeV as shown in fig. 2.8 on the right-hand side. However, if one drops the quartic self-interaction completely, again the temperature dependence becomes more pronounced. The results agree very well with the findings in [MPG01]. However, these authors adapt the parameters of their model to a higher incompressibility which leads to a slightly stiffer equation of state. In the tree-level case they drop the quartic self-coupling of the  $\sigma$  field completely.



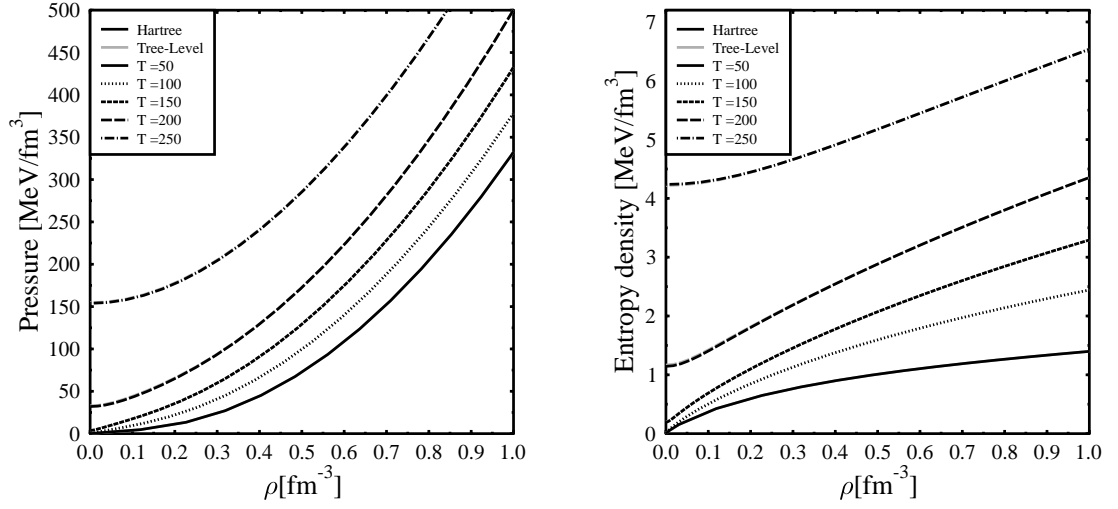


Figure 2.7: The pressure (left) and the entropy density (right) in Hartree and tree-level approximation. The differences between the approximations are almost invisible.

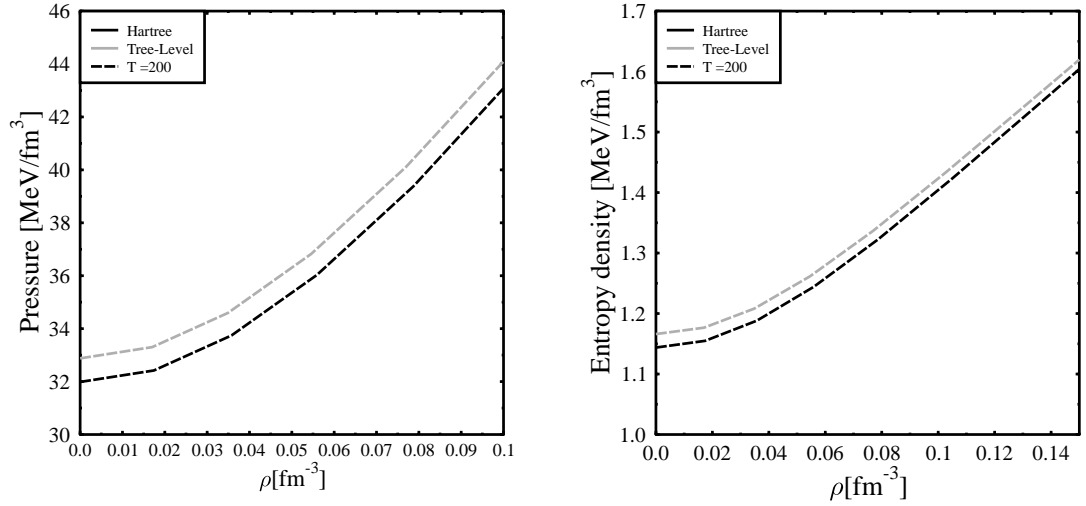


Figure 2.8: The pressure (left) and the entropy density (right) in Hartree and tree-level approximation at  $T = 200$  MeV. The figure highlights the differences between the approximations.



## –III–

# BEYOND THE HARTREE APPROXIMATION

The Hartree approximation presented in the previous chapter leads to a shift of the particle's masses but not to a non-zero decay width. This is because the integrals in the self-energies do not depend on the external momentum and therefore do not adopt an imaginary part. The situation changes if one takes into account all diagrams of fig. 2.1. Now the full propagators, which are solutions of the Schwinger-Dyson equations, acquire non-zero decay widths, so the simple Ansätze (2.7) and (2.8) are not longer feasible. Instead of effective masses which are independent of the external momentum now spectral functions have to be introduced. The calculations become much more complicated here, both analytically and numerically but on the other hand this approach allows to study the energy dependence of the decay and therefore discloses a broad field of phenomena.

To keep the effort limited I restrict myself to the *imaginary parts* of the sunset diagrams. Considering the real parts as well would lead to serious difficulties because in contrast to the imaginary parts the real parts contain divergences that have to be renormalized. Nevertheless, I consider an effective mass for the fermion and the  $\sigma$  meson on Hartree level.

## 3.1 General prerequisites

### 3.1.1 The spectral function

On tree-level or in Hartree approximation one can assign a particle a fixed mass. It is that of the free particle modified by a real-valued self-energy. The propagator only contributes at energies where it has poles. For example the boson propagator

$$G = -\frac{1}{k_0^2 - \mathbf{k}^2 - M^2 + \Pi} \quad (3.1)$$

has poles at  $k_0 = \pm\sqrt{\mathbf{k}^2 + M^2 - \Pi}$ . Plotting the 'strength' of the propagator in the energy-momentum plane would therefore show a delta function at these energies while it is zero everywhere else. It will be discussed later what exactly the strength is.

The general situation is more complicated because the self-energy can assume an imaginary part as well. This leads to a non-zero width for the strength of the propagator in the energy-momentum plane. In order to cover this effect more precisely, in the following the *spectral function* or *spectral density* is introduced. Consider the advanced and retarded two-point functions

$$D^>(t, t') = \langle \hat{\phi}(t) \hat{\phi}(t') \rangle_\beta \quad , \quad (3.2)$$

and

$$D^<(t', t) = \langle \hat{\phi}(t') \hat{\phi}(t) \rangle_\beta \quad , \quad (3.3)$$

where  $t > t'$ . Here  $\hat{\phi}$  is a field operator and the subscript  $\beta$  denotes that the thermal average is taken as

$$\langle \hat{A} \rangle_\beta = \frac{1}{Z(\beta)} \text{Tr}(\hat{A} e^{-\beta \hat{A}}) \quad . \quad (3.4)$$

$Z(\beta)$  is defined as in (1.117).

Because of the homogeneity of time the two-point functions only depend on differences of times  $t - t'$ . I therefore write them in short terms as  $D^>(t) = D^>(t, 0)$  and  $D^<(t) = D^<(t, 0)$ .

The Fourier transform of the two-point functions are

$$D^>(k_0) = \int_{-\infty}^{\infty} dt e^{ik_0 t} D^>(t) \quad (3.5)$$

and

$$D^<(k_0) = \int_{-\infty}^{\infty} dt e^{ik_0 t} D^<(t) \quad . \quad (3.6)$$

One can show that physically the upper function corresponds to the mean density of unoccupied states in momentum space while the lower function is the mean density of occupied states [Frö01]. Now the *spectral function* can be defined as

$$\rho(k_0) = D^>(k_0) - D^<(k_0) \quad , \quad (3.7)$$

which gives the total number of states at a certain momentum.

The meaning of the spectral function can be clarified further. Consider the operator  $\exp(-\beta \hat{H})$ . According to section 1.4 this is not only the density matrix but, following the idea of the imaginary time formalism, it is also the time-evolution operator in imaginary time direction. One can therefore use it to shift the time argument of a field:

$$e^{-\beta \hat{H}} \hat{\phi}(t) e^{\beta \hat{H}} = \hat{\phi}(t + i\beta) \quad . \quad (3.8)$$

With the cyclicity of the trace the Kubo-Martin-Schwinger relation (KMS) follows:

$$D^>(t) = D^<(t + i\beta) \quad . \quad (3.9)$$

Inserting this into the Fourier transform of the retarded propagator (3.6) yields the relation

$$D^<(k_0) = \int_{-\infty}^{\infty} dt e^{-ik_0 t} D^>(t - i\beta) \quad (3.10)$$

and inserting the inverse Fourier transform of (3.5) on the right-hand side gives

$$D^<(k_0) = D^>(-k_0) = e^{\beta k_0} D^>(k_0) \quad . \quad (3.11)$$

Hereby one can now express the retarded and advanced propagators in terms of the spectral density:

$$D^>(k_0) = (1 + f(k_0))\rho(k_0) \quad \text{and} \quad D^<(k_0) = f(k_0)\rho(k_0) \quad , \quad (3.12)$$

where

$$f(k_0) = \frac{1}{e^{\beta k_0} - 1} \quad (3.13)$$

is the Bose distribution function.

Above it has been stated in a quite hand-waving way that the propagator has 'strength' at different momenta and energies whenever the self-energy is complex. Energy and momentum are not linked by a  $\delta$  function as for the free field. This property can be put in more precise words with help of the spectral function. Let us consider the imaginary time propagator

$$\Delta(\tau) = \langle T[\hat{\phi}(-i\tau)\hat{\phi}(0)] \rangle_{\beta} \quad , \quad (3.14)$$

where  $T$  is the time-ordering operator for imaginary times:

$$T[\hat{\phi}(-i\tau_1)\hat{\phi}(-i\tau_2)] = \begin{cases} \hat{\phi}(-i\tau_1)\hat{\phi}(-i\tau_2) & \text{if } \tau_1 > \tau_2 \\ \hat{\phi}(-i\tau_2)\hat{\phi}(-i\tau_1) & \text{if } \tau_2 > \tau_1 \end{cases} \quad . \quad (3.15)$$

One can then define its Fourier transform through

$$\Delta(i\omega_n) = \int_0^{\beta} d\tau e^{i\omega_n \tau} \Delta(\tau) \quad (3.16)$$

and inversely

$$\Delta(\tau) = T \sum_n e^{-i\omega_n \tau} \Delta(i\omega_n) \quad . \quad (3.17)$$

Here, it has been used that  $\Delta(\tau)$  is periodic as shown in section 1.4. The periodicity makes it sufficient to integrate over a finite temperature interval in (3.16) and to replace the integral in the inverse transformation (3.17) by a sum over

discrete energies. The discrete energies  $\omega_n$  are called *Matsubara frequencies*. For bosons they take the values

$$\omega_n = \frac{2\pi n}{\beta} \quad . \quad (3.18)$$

From the definition of  $\Delta(\tau)$  it follows that  $\Delta(\tau) = D^>(-i\tau)$ . With the Fourier transform (3.5) one can write this as

$$\Delta(\tau) = \int \frac{dk_0}{2\pi} e^{-k_0\tau} D^>(k_0) \quad , \quad (3.19)$$

which can be inserted into (3.16). After expressing  $D^>(k_0)$  in terms of the spectral function (3.12) and performing the  $\tau$  integration one obtains

$$\Delta(i\omega_n) = - \int_{-\infty}^{\infty} \frac{dk_0}{2\pi} \frac{\rho(k_0)}{i\omega_n - k_0} \quad . \quad (3.20)$$

This expression clarifies what was meant by 'strength' above: The spectral function weights the contributions to the full imaginary-time propagator at each value of the energy  $k_0$ . This can be highlighted even further when looking at free particles. As mentioned above a fixed relation between energy and momentum exists here, so one would expect the spectral function to be a delta function in energy direction. In fact the respective function is

$$\rho_{\text{free}}(k_0) = 2\pi \text{sig}(k_0) \delta(k_0^2 - \omega^2) \quad . \quad (3.21)$$

Inserting this into (3.20) gives the propagator of the free particle

$$\Delta_{\text{free}}(i\omega_n) = \frac{1}{\omega_n^2 + \omega^2} \quad . \quad (3.22)$$

Finally, one can calculate the spectral function from the propagator. Therefore one defines the retarded propagator as

$$D_R(t) = i \langle \Theta(t) [\hat{\phi}(t), \hat{\phi}(0)] \rangle_{\beta} \quad . \quad (3.23)$$

The  $\Theta$ -function can be expressed as

$$\Theta(y) = i \int_{-\infty}^{\infty} \frac{dk'_0}{2\pi} \frac{e^{-ik'_0 t}}{k'_0 + i\eta} \quad , \quad (3.24)$$

so the retarded propagator becomes

$$D_R(k_0) = - \int_{-\infty}^{\infty} \frac{dk'_0}{2\pi} \frac{\rho(k'_0)}{k_0 - k'_0 + i\eta} \quad . \quad (3.25)$$

where the commutator in (3.23) has been written in terms of the spectral function. This can be extracted from this expression with help of the *Dirac identity*

$$\text{Im} \left( \frac{1}{k_0 - k'_0 + i\eta} \right) = -i\pi \delta(k_0 - k'_0). \quad (3.26)$$

One obtains

$$\rho(k_0) = 2 \text{Im} D_R(k_0) \quad . \quad (3.27)$$

### The fermionic spectral function

For fermions some differences in the definition of the spectral function occur, because these obey anti-commutation relations instead of commutation relations like the bosons. So the advanced and retarded two-point functions are now defined as

$$S_{ab}^>(t, t') = \langle \psi_a(t) \bar{\psi}_b(t') \rangle_\beta \quad , \quad (3.28)$$

as well as

$$S_{ab}^<(t, t') = -\langle \bar{\psi}_b(t') \psi_a(t) \rangle_\beta \quad , \quad (3.29)$$

respectively, where the indices  $a$  and  $b$  account for the spinor structure. As above one can derive the *Kubo-Martin-Schwinger relation* by applying the evolution operator in imaginary time  $\exp(-\beta \hat{H})$  :

$$S_{ab}^>(t, t') = -S_{ab}^<(t + i\beta, t') \quad . \quad (3.30)$$

Its Fourier transform is

$$S_{ab}^>(k_0) = \int dt e^{ik_0 t} S^>(t, 0) \quad , \quad (3.31)$$

where  $t' = 0$  assumes homogeneity of time. For  $S_{ab}^<$  a similar relation holds. The spectral function can now again be defined as

$$\rho_{ab}(k_0) = S_{ab}^>(k_0) - S_{ab}^<(k_0) \quad . \quad (3.32)$$

Observing that analogous to (3.11)

$$S_{ab}^<(k_0) = -e^{-\beta k_0} S_{ab}^>(k_0) \quad , \quad (3.33)$$

one can express the two-point functions in terms of the spectral function as

$$S_{ab}^>(k_0) = (1 - \tilde{f}(k_0)) \rho_{ab}(k_0) \quad \text{and} \quad S_{ab}^<(k_0) = -\tilde{f}(k_0) \rho_{ab}(k_0) \quad , \quad (3.34)$$

with the Fermi-distribution function

$$\tilde{f}(k_0) = \frac{1}{e^{\beta k_0} + 1} \quad . \quad (3.35)$$

As for bosons one can derive a spectral representation of the imaginary-time propagator:

$$S_{ab}(i\omega_n) = - \int_{-\infty}^{\infty} \frac{dk_0}{2\pi} \frac{\rho_{ab}(k_0)}{i\omega_n - k_0} \quad (3.36)$$

with the Matsubara frequencies

$$\omega_n = \frac{(2n+1)\pi}{\beta} \quad . \quad (3.37)$$

The interpretation as strength of the propagator at different energies  $k_0$  holds as for bosons. Again the spectral function of a free fermion is a delta function

$$\rho_{\text{free}} = 2\pi \text{sig}(k_0)(K_\mu \gamma^\mu + m)\delta(K^2 - m^2) \quad , \quad (3.38)$$

which yields the free propagator when entered into (3.36):

$$S_{ab}(i\omega_n) = \frac{m - K_\mu \gamma^\mu}{\omega_n^2 + E_k^2} \quad . \quad (3.39)$$

### 3.1.2 Projection operators for the vector mesons

The vector meson self-energy is a second-order tensor. To make it accessible for numerical evaluation one has to find a set of projectors which express it as a combination of projection tensors with scalar prefactors. The presentation here follows [Ris04].

We start with defining a projector

$$E^{\mu\nu} \equiv \frac{P^\mu P^\nu}{P^2} \quad , \quad (3.40)$$

which projects on the subspace parallel to the four-momentum  $P^\mu$ . Furthermore, one defines a vector which is orthogonal to  $P^\mu$

$$N^\mu \equiv \left( \frac{p_0 \mathbf{P}^2}{P^2}, \frac{p_0^2 \mathbf{P}}{P^2} \right) \quad . \quad (3.41)$$

The respective projector, which projects on a subspace parallel to  $N^\mu$ , is

$$B^{\mu\nu} \equiv \frac{N^\mu N^\nu}{N^2} \quad . \quad (3.42)$$

The other two projectors that are necessary can then be defined as

$$C^{\mu\nu} \equiv N^\mu P^\nu + P^\mu N^\nu \quad \text{and} \quad A^{\mu\nu} \equiv g^{\mu\nu} - B^{\mu\nu} - E^{\mu\nu} \quad . \quad (3.43)$$

With these four projectors a tensor of second order can be decomposed as

$$\Pi^{\mu\nu} = \Pi^a A^{\mu\nu} + \Pi^b B^{\mu\nu} + \Pi^c C^{\mu\nu} + \Pi^e E^{\mu\nu} \quad . \quad (3.44)$$

For calculations it is useful to regard the explicit structure of these projectors. The projector  $A^{\mu\nu}$  only has spatial components while all time components vanish:

$$A^{00} = A^{0i} = 0 \quad \text{and} \quad A^{ij} = -(\delta^{ij} - \hat{p}^i \hat{p}^j) \quad . \quad (3.45)$$

Obviously it projects onto a subspace transverse to the spatial components of  $P$ . I will therefore also use the definition

$$\Pi^t = -\Pi^a \quad (3.46)$$



for the *transverse* part of the self-energy. The projector  $B^{\mu\nu}$  projects on a subspace parallel to  $\mathbf{p}$ :

$$B^{00} = -\frac{\mathbf{p}^2}{P^2} \quad , \quad B^{0i} = -\frac{p_0 p^i}{P^2} \quad \text{and} \quad B^{ij} = -\frac{p_0^2}{P^2} \hat{p}^i \hat{p}^j \quad . \quad (3.47)$$

In my later calculations I use a compact notation for  $B^{\mu\nu}$  which summarizes the above terms

$$B^{\mu\nu} = g^{\mu\nu} + \delta^{ij} - \frac{P^\mu P^\nu}{P^2} - \hat{p}^i \hat{p}^j \quad . \quad (3.48)$$

Here the roman indices  $i$  and  $j$  only run over the spatial components  $i, j = 1, 2, 3$  and quantities indicated by them are zero if one or more of its roman indices are zero. The index  $i$  corresponds to the four-index  $\mu$  while the index  $j$  corresponds to  $\nu$ .

The projector  $C^{\mu\nu}$  reads in terms of momenta

$$C^{00} = 2\frac{p_0^2 \mathbf{p}^2}{P^2} \quad , \quad C^{0i} = \frac{|\mathbf{p}| p_0 (p_0^2 + \mathbf{p}^2)}{P^2} \hat{p}^i \quad , \quad \text{and} \quad C^{ij} = 2\frac{p_0^2 \mathbf{p}^2}{P^2} \hat{p}^i \hat{p}^j \quad , \quad (3.49)$$

and the  $E^{\mu\nu}$  projector is

$$E^{00} = \frac{p_0^2}{P^2} \quad , \quad E^{0i} = \frac{p_0 |\mathbf{p}|}{P^2} \hat{p}^i \quad , \quad \text{and} \quad E^{ij} = \frac{\mathbf{p}^2}{P^2} \hat{p}^i \hat{p}^j \quad . \quad (3.50)$$

However, not all of the above projections are physical. Eventually it will turn out that only two projections have to be considered. To eliminate the unphysical components Stückelberg's trick is applied. The idea is to introduce an additional term into the Proca-Lagrangian for massive vector particles which leads to the *Stückelberg Lagrangian*

$$\mathcal{L} = -\frac{1}{4} F_{\mu\nu} F^{\mu\nu} + \frac{1}{2} m_\omega^2 \omega_\mu \omega^\mu - \frac{1}{2\xi} (\partial_\mu \omega^\mu)^2 \quad . \quad (3.51)$$

In the end  $\xi$  will be sent to infinity so the physical situation remains unchanged. It emerges that certain projections are vanishing. With the modified Lagrangian one can deduce the modified inverse free propagator in momentum space:

$$D_\omega^{-1}(K) = -(m_\omega^2 - K^2) g_{\mu\nu} - \left(1 - \frac{1}{\xi}\right) K_\mu K_\nu \quad , \quad (3.52)$$

so the inverse full propagator is

$$\mathcal{G}_\omega^{-1\mu\nu}(K) = D_\omega^{-1}(K) + \Pi_\omega^{\mu\nu}(K) \quad . \quad (3.53)$$

I now want to invert the full propagator with help of the tensor decomposition as presented in [LB00]. Therefore the different projections for the free inverse propagator are determined, first. The  $A^{\mu\nu}$  projection is

$$\begin{aligned} (D_\omega^a)^{-1}(K) &= -\frac{1}{2} (\delta^{ij} - \hat{k}^i \hat{k}^j) (D_\omega^{-1})^{ij}(K) \\ &= K^2 - m_\omega^2 \quad . \end{aligned} \quad (3.54)$$

For the  $B^{\mu\nu}$  projection one obtains

$$\begin{aligned} (D_\omega^b)^{-1}(K) &= \frac{1}{N^2} \left[ (K^2 - m_\omega^2) N^2 - \left(1 - \frac{1}{\xi}\right) (N_\mu K^\mu)^2 \right] \\ &= K^2 - m_\omega^2 \quad , \end{aligned} \quad (3.55)$$

and the  $C^{\mu\nu}$  projection is

$$\begin{aligned} (D_\omega^c)^{-1}(K) &= \left[ (K^2 - m_\omega^2) N_\mu K^\mu - 2 \left(1 - \frac{1}{\xi}\right) N_\mu K^\mu K^2 \right] \\ &= 0 \quad . \end{aligned} \quad (3.56)$$

Finally, the  $E^{\mu\nu}$  projection is

$$\begin{aligned} (D_\omega^e)^{-1}(K) &= (K^2 - m_\omega^2) - \left(1 - \frac{1}{\xi}\right) K^2 \\ &= \frac{K^2 - \xi m_\omega^2}{\xi} \quad . \end{aligned} \quad (3.57)$$

As shown in [LB00] the inverse of a structure

$$X_{\mu\nu} = X^a A_{\mu\nu} + X^b B_{\mu\nu} + X^c C_{\mu\nu} + X^e E_{\mu\nu} \quad (3.58)$$

is given as

$$X_{\mu\nu}^{-1} = \alpha A_{\mu\nu} + \beta B_{\mu\nu} + \gamma C_{\mu\nu} + \eta E_{\mu\nu} \quad , \quad (3.59)$$

with

$$\alpha = \frac{1}{X^a} \quad , \quad \beta = \frac{X^e}{\delta} \quad , \quad \gamma = -\frac{X^c}{\delta} \quad , \quad \eta = \frac{\beta}{\delta} \quad (3.60)$$

and

$$\delta = X^b X^e - K^2 N^2 X^{c2} \quad . \quad (3.61)$$

With this the full propagator becomes

$$\begin{aligned} \mathcal{G}_{\omega\mu\nu}(K) &= \frac{1}{K^2 - m_\omega^2 + \Pi_\omega^a} A_{\mu\nu} + \frac{1}{K^2 - m_\omega^2 + \Pi_\omega^b - K^2 N^2 \frac{\Pi_\omega^{c2}}{K^2 - \xi m_\omega^2 + \Pi_\omega^e}} B_{\mu\nu} \\ &\quad - \frac{\Pi_\omega^c}{(K^2 - m_\omega^2 + \Pi_\omega^b)(K^2 - \xi m_\omega^2 + \Pi_\omega^e) - K^2 N^2 (\Pi_\omega^c)^2} C_{\mu\nu} \\ &\quad + \frac{1}{K^2 - \xi m_\omega^2 + \Pi_\omega^e - K^2 N^2 \frac{\Pi_\omega^{c2}}{K^2 - m_\omega^2 + \Pi_\omega^b}} E_{\mu\nu} \quad . \end{aligned} \quad (3.62)$$

One can now eliminate the contributions from the Stückelberg term by sending  $\xi \rightarrow \infty$ . Obviously the  $C_{\mu\nu}$  term and the  $E_{\mu\nu}$  term vanish and one obtains

$$\mathcal{G}_{\omega\mu\nu}(K) = \frac{1}{K^2 - m_\omega^2 + \Pi_\omega^a} A_{\mu\nu} + \frac{1}{K^2 - m_\omega^2 + \Pi_\omega^b} B_{\mu\nu} \quad . \quad (3.63)$$

With this result I can restrict my later considerations to the  $A_{\mu\nu}$  and  $B_{\mu\nu}$  projection. The transverse projection is defined as

$$\Pi^t(K) = \frac{1}{2}(\delta^{ij} - \hat{k}^i \hat{k}^j) \Pi^{ij}(K) \quad , \quad (3.64)$$

while the longitudinal projection is

$$\Pi^\ell(K) = \hat{k}_i \Pi^{ij}(K) \hat{k}_j \quad . \quad (3.65)$$

Since in my case the  $C$  and  $E$  projections vanish the following relations hold for the  $A$  and  $B$  projections

$$\begin{aligned} \Pi^a(K) &= -\Pi^t(K) \quad , \\ \Pi^b(K) &= -\frac{|\mathbf{k}|^2}{K^2} \left( \Pi^{00}(K) + 2\frac{k_0}{|\mathbf{k}|} \Pi^{0i}(K) \hat{k}_i + \frac{k_0^2}{|\mathbf{k}|^2} \Pi^\ell(K) \right) \quad . \end{aligned} \quad (3.66)$$

In this work I assume that  $\Pi_\omega^{\mu\nu}$  is transverse, that is  $\Pi_\omega^{\mu\nu} K_\nu = 0$ .

### 3.1.3 The Dirac structure of the fermions

The self-energy and the spectral function of the fermions have a Dirac structure that is they are  $4 \times 4$  matrices. To extract scalar quantities from these one can expand them into products of  $\gamma$  matrices. There are 16 linearly independent structures built from  $\gamma$  matrices. In general a Dirac-matrix can therefore be written as

$$\begin{aligned} \rho(K) &= \mathbb{1} \rho_m(k_0, |\mathbf{k}|) + \gamma^0 \rho_0(k_0, |\mathbf{k}|) - (\boldsymbol{\gamma} \cdot \hat{\mathbf{k}}) \rho_v(k_0, |\mathbf{k}|) \\ &\quad + \sigma^{\mu\nu} K_\mu K_\nu \rho_t(k_0, |\mathbf{k}|) + \gamma^5 \tilde{\rho}(K) + (\gamma^\mu \gamma^5) \tilde{\rho}_\mu(K) \quad . \end{aligned} \quad (3.67)$$

However, not all of these structures contribute to the self-energies and spectral functions in this work. Some of the terms vanish for parity symmetric systems. The term  $\sigma^{\mu\nu} K_\mu K_\nu \rho_t(K)$  consists of a symmetric structure  $K_\mu K_\nu$  and the anti-symmetric  $\sigma^{\mu\nu}$  so the product of both vanishes.

In the following it is shown that terms including  $\gamma_5$  break parity invariance and therefore do not contribute to my spectral functions. The spectral function is from its definition

$$\rho_\psi(K) = \langle \psi_a(K) \bar{\psi}_b(K') \rangle_\beta + \langle \bar{\psi}_b(K') \psi_a(K) \rangle_\beta \quad . \quad (3.68)$$

Applying a parity transformation to the single field yields

$$P\psi(t, \mathbf{x})P^{-1} = \eta\gamma^0\psi(t, -\mathbf{x}) \quad (3.69)$$

where  $\eta$  is a phase factor that is a power of the imaginary unit. For the adjoint field one obtains

$$P\bar{\psi}(t, \mathbf{x})P^{-1} = P\psi^\dagger(t, \mathbf{x})P^{-1}\gamma^0 = (P\psi(t, \mathbf{x})P^{-1})^\dagger\gamma^0 = \eta^*\bar{\psi}(t, -\mathbf{x})\gamma^0 \quad . \quad (3.70)$$

Therefore, the spectral function transforms as

$$P\rho_\psi(k_0, \mathbf{k})P^{-1} = \underbrace{\eta\eta^*}_{=1}\gamma^0\rho_\psi(k_0, -\mathbf{k})\gamma^0 \quad . \quad (3.71)$$

One can now insert the respective terms of (3.67) into this to find

$$\gamma^0\gamma^5\tilde{\rho}(k_0, \mathbf{k})\gamma^0 = -\gamma^5\tilde{\rho}(k_0, -\mathbf{k}) \quad , \quad (3.72)$$

because  $\gamma^5$  anti-commutes with  $\gamma^0$ . Analogously,

$$\gamma^0\gamma^\mu\gamma^5\tilde{\rho}_\mu(k_0, \mathbf{k})\gamma^0 = \begin{cases} -\gamma^\mu\gamma^5\tilde{\rho}_\mu(k_0, -\mathbf{k}) & \text{for } \mu = 0 \\ +\gamma^\mu\gamma^5\tilde{\rho}_\mu(k_0, -\mathbf{k}) & \text{for } \mu = 1, 2, 3 \end{cases} \quad . \quad (3.73)$$

Obviously those parts of the spectral function which include  $\gamma^5$  change their sign under parity transformation. The spatial terms change their sign because of the factor  $\mathbf{k}$  in front. So if I assume that the spectral function is invariant under parity transformation those terms should not contribute.

If one drops these symmetry breaking terms the structure of the spectral function becomes considerably simpler:

$$\rho(K) = \mathbb{1}\rho_m(|\mathbf{k}|) + \gamma_0\rho_0(|\mathbf{k}|) - (\boldsymbol{\gamma} \cdot \hat{\mathbf{k}})\rho_v(|\mathbf{k}|) \quad . \quad (3.74)$$

The single parts of this can be extracted from a given Dirac matrix by applying the trace operation in the following way (Isospin adds a further factor  $\frac{1}{2}$ ):

$$\begin{aligned} \rho_0(k_0, |\mathbf{k}|) &= \frac{1}{4}\text{Tr}\gamma_0\rho(K) \quad , \\ \rho_v(k_0, |\mathbf{k}|) &= \frac{1}{4}\text{Tr}(\boldsymbol{\gamma} \cdot \hat{\mathbf{k}})\rho(K) \quad , \\ \rho_m(k_0, |\mathbf{k}|) &= \frac{1}{4}\text{Tr}\rho(K) \quad . \end{aligned} \quad (3.75)$$

## 3.2 The self-energies, masses, and fields

In this section I present the self-energies which are obtained if the *sunset diagrams* are taken into account within the CJT formalism. First the effective potential is assembled according to the rules given in section 1.3.3.

Special attention has to be given to the symmetry factors that count the possibilities to connect the vertices in the diagrams. For diagrams containing fermion lines there is only one way to connect two vertices because the fermion propagators depend on the direction of the momentum they carry. Thus there is only one fermion line with incoming and one line with outgoing momentum. A line with outgoing momentum from one vertex has to be connected to a line with incoming momentum at the other vertex (compare fig. 3.1).

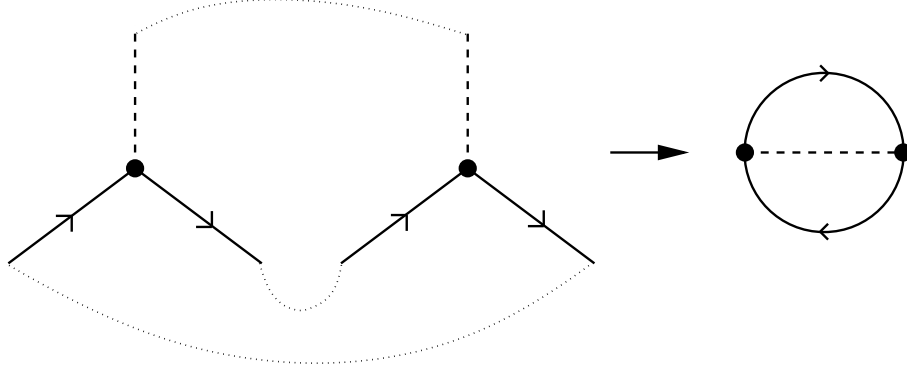


Figure 3.1: Vertices containing fermion lines can be connected only in one way.

For the sunset diagram composed of three  $\sigma$  propagators the symmetry factor is six because there are six different possibilities to connect the lines meeting at the vertices. To see this imagine two vertices merging three  $\sigma$  lines each. Assume they are connected via one line. Three lines could be chosen for this first connection so the symmetry factor of this composition is three. At each vertex there are now two lines left to be connected so there are two possibilities for the second connection. The last line is fixed then. The overall symmetry factor is therefore  $3 \cdot 2 = 6$ .

Before one can write down the effective potential resulting from the two-particle irreducible diagrams one has to state how the momenta are running in the diagrams. There are different possibilities, the only restraint being that momentum is conserved at the vertices. Here and in the following  $K$  will denote the external momentum while  $P$  and  $Q$  stand for momenta which are integrated over. In this work I assume the momenta to run as shown in fig. 3.2. If all diagrams of fig. 2.1 are taken into account the two-particle irreducible part of the effective potential therefore becomes

$$\begin{aligned}
 V_2[\hat{\sigma}, G_\sigma, G_\omega, G_\psi] &= \frac{1}{2} g_\sigma^2 \text{Tr} \int_P \int_Q G_\sigma(P-Q) G_\psi(P) G_\psi(Q) \\
 &+ \frac{1}{2} g_\omega^2 \text{Tr} \int_P \int_Q \gamma^\mu G_\psi(P) \gamma^\nu G_\psi(Q) G_{\omega\mu\nu}(P-Q) \\
 &- 3 (4\lambda\hat{\sigma})^2 \int_P \int_Q G_\sigma(P-Q) G_\sigma(P) G_\sigma(Q) \\
 &+ 3\lambda \left[ \int_P G_\sigma(P) \right]^2 .
 \end{aligned} \tag{3.76}$$

The first three terms correspond to the sunset diagrams in fig. 2.1 while the last term is the double-bubble diagram known from the Hartree approximation. With (1.108) this leads to the following self-energies.

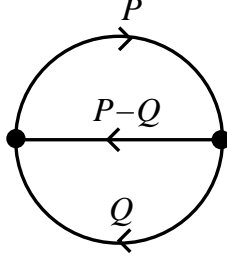


Figure 3.2: Distribution of momenta in sunset diagrams.

### 3.2.1 The self-energy of the $\sigma$ meson

For the  $\sigma$  meson the self-energy reads

$$\begin{aligned}
 \Pi_\sigma(K) &= 2 \frac{\delta V_2[\hat{\sigma}, G_\sigma, G_{\omega\mu\nu}, G_\psi]}{\delta G_\sigma(K)} \\
 &= g_\sigma^2 \text{Tr} \int_Q \mathcal{G}_\psi(Q+K) \mathcal{G}_\psi(Q) - 18 (4\lambda\hat{\sigma})^2 \int_Q \mathcal{G}_\sigma(Q+K) \mathcal{G}_\sigma(Q) \\
 &\quad + 12\lambda \int_P \mathcal{G}_\sigma(P) \quad .
 \end{aligned} \tag{3.77}$$

For lucidity this is shown diagrammatically in fig. 3.3. Note that the functional derivative with respect to the propagator leads to a Dirac delta function whereby the external momentum  $K$  enters the integrands. Furthermore the product rule has to be applied where two or more  $\sigma$  propagators occur. This leads to an additional factor of three in the respective part of the self-energy.

The self-energy (3.77) has a complicated substructure which has to be resolved before explicit calculations can be carried out. The task is to evaluate the Matsubara sums, account for the Dirac substructure of the fermions, and simplify the momentum integrations as far as possible to keep the numerical effort limited. Since the last term of (3.77) does not carry an imaginary part it will not be discussed any further in the following. To keep track of the calculations they are presented term by term in the following.

#### The term $\int_Q \mathcal{G}_\sigma(Q+K) \mathcal{G}_\sigma(Q)$

The first term presented here is the  $\sigma$  loop sunset term. I start with evaluating the Matsubara sum and introducing the spectral function for the  $\sigma$  field. The first step is to express the propagator  $\mathcal{G}_\sigma$  in the *mixed representation*:

$$\mathcal{G}_\sigma(i\omega, |\mathbf{k}|) = \int_0^\beta d\tau \exp(i\omega\tau) \mathcal{G}_\sigma(\tau, |\mathbf{k}|) \quad , \tag{3.78}$$

that is the Matsubara frequency is replaced by an imaginary time in the argument of the propagator via a Fourier transformation. With this the respective part of

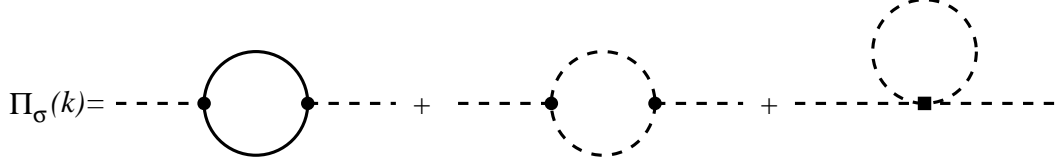


Figure 3.3: The self-energy of the  $\sigma$  meson in diagrammatic language.

the self-energy becomes

$$\begin{aligned} \int_Q \mathcal{G}_\sigma(Q+K) \mathcal{G}_\sigma(Q) &= T \sum_n \int \frac{d^3 \mathbf{q}}{(2\pi)^3} \mathcal{G}_\sigma(i(\omega_n + \omega), |\mathbf{q} + \mathbf{k}|) \mathcal{G}_\sigma(i\omega_n, |\mathbf{q}|) \\ &= T \sum_n \int \frac{d^3 \mathbf{q}}{(2\pi)^3} \int_0^\beta d\tau \int_0^\beta d\tau' \exp[i\omega_n(\tau + \tau')] \exp(i\omega\tau) \mathcal{G}_\sigma(\tau, |\mathbf{q} + \mathbf{k}|) \mathcal{G}_\sigma(\tau', |\mathbf{q}|) \end{aligned} \quad (3.79)$$

where  $\omega$  is the Matsubara frequency of the external momentum  $K$ . The Matsubara sum can now be evaluated with help of the relation

$$T \sum_n \exp(i\omega_n \tau) = \sum_p \delta(\tau - p\beta) \quad \text{with} \quad p = 0, \pm 1, \pm 2, \dots, \quad (3.80)$$

applied to the exponential function of (3.79). The result is

$$\int_Q \mathcal{G}_\sigma(Q+K) \mathcal{G}_\sigma(Q) = \int \frac{d^3 \mathbf{q}}{(2\pi)^3} \int_0^\beta d\tau \exp(i\omega\tau) \mathcal{G}_\sigma(\tau, |\mathbf{q} + \mathbf{k}|) \mathcal{G}_\sigma(\beta - \tau, |\mathbf{q}|). \quad (3.81)$$

One can then introduce spectral functions according to (3.19) with (3.12) inserted:

$$\mathcal{G}_\sigma(\tau, |\mathbf{q}|) = \int_{-\infty}^{\infty} \frac{d\ell}{2\pi} [1 + f(\ell)] \exp(-\ell\tau) \rho_\sigma(\ell, |\mathbf{q}|), \quad (3.82)$$

with the bosonic distribution function

$$f(\ell) = \frac{1}{e^{\beta\ell} - 1}. \quad (3.83)$$

Thus the self-energy becomes

$$\begin{aligned} \int_Q \mathcal{G}_\sigma(Q+K) \mathcal{G}_\sigma(Q) &= \int \frac{d^3 \mathbf{q}}{(2\pi)^3} \int_0^\beta d\tau \int_{-\infty}^{\infty} \frac{d\ell_1}{2\pi} \int_{-\infty}^{\infty} \frac{d\ell_2}{2\pi} [1 + f(\ell_1)] f(\ell_2) \\ &\quad \times \exp(-\ell_1 \tau) \exp(\ell_2 \tau) \exp(i\omega\tau) \rho_\sigma(\ell_1, |\mathbf{q} + \mathbf{k}|) \rho_\sigma(\ell_2, |\mathbf{q}|) \\ &= \int \frac{d^3 \mathbf{q}}{(2\pi)^3} \int_{-\infty}^{\infty} \frac{d\ell_1}{2\pi} \int_{-\infty}^{\infty} \frac{d\ell_2}{2\pi} [1 + f(\ell_1)] f(\ell_2) \\ &\quad \times \frac{\exp[(\ell_2 - \ell_1)\beta] - 1}{i\omega - \ell_1 + \ell_2} \rho_\sigma(\ell_1, |\mathbf{q} + \mathbf{k}|) \rho_\sigma(\ell_2, |\mathbf{q}|). \end{aligned} \quad (3.84)$$

Here it has been used that  $(1 + f(\ell_2)) \exp(-\ell_2 \beta) = f(\ell_2)$ . In the second step the  $\tau$  integration has been carried out explicitly.

The numerical calculation of the self-energies will be performed on a discretized space-time lattice. This comes along with a huge effort in computing power so it is desirable to reduce the analytical expressions as much as possible. Here it is in particular useful to carry out some of the three-dimensional spatial integrations. This will be shown in the following.

The term under consideration has a momentum dependence of the form

$$\int \frac{d^3 \mathbf{q}}{(2\pi)^3} \rho_\sigma(|\mathbf{q} + \mathbf{k}|) \rho_\sigma(|\mathbf{q}|) \quad , \quad (3.85)$$

where all factors that do not depend on the momentum have been omitted. If one assumes spherical symmetry one can switch to spherical coordinates to obtain

$$\int \frac{d^3 \mathbf{q}}{(2\pi)^3} \rho_\sigma(|\mathbf{q} + \mathbf{k}|) \rho_\sigma(|\mathbf{q}|) = \frac{1}{(2\pi)^3} \int |\mathbf{q}|^2 d|\mathbf{q}| d\cos\Theta d\varphi \rho_\sigma(|\mathbf{q} + \mathbf{k}|) \rho_\sigma(|\mathbf{q}|) \quad , \quad (3.86)$$

where  $\Theta$  is the angle between  $\mathbf{q}$  and  $\mathbf{k}$ . A proper substitution for the absolute value  $|\mathbf{q} + \mathbf{k}|$  can be found as follows. The square of this absolute value is

$$|\mathbf{q} + \mathbf{k}|^2 = \mathbf{q}^2 + \mathbf{k}^2 + 2|\mathbf{q}||\mathbf{k}| \cos\Theta \quad . \quad (3.87)$$

With setting  $\ell = |\mathbf{q} + \mathbf{k}|$  one finds that

$$\cos\Theta = \frac{|\ell|^2 - |\mathbf{q}|^2 - |\mathbf{k}|^2}{2|\mathbf{k}||\mathbf{q}|} \quad (3.88)$$

and therefore

$$d\cos\Theta = \frac{|\ell|}{|\mathbf{k}||\mathbf{q}|} d|\ell| \quad . \quad (3.89)$$

So the integral can be written as

$$\begin{aligned} \int \frac{d^3 \mathbf{q}}{(2\pi)^3} \rho_\sigma(|\mathbf{q} + \mathbf{k}|) \rho_\sigma(|\mathbf{q}|) &= \frac{1}{(2\pi)^2 |\mathbf{k}|} \int |\mathbf{q}| d|\mathbf{q}| \int |\ell| d|\ell| \rho_\sigma(|\ell|) \rho_\sigma(|\mathbf{q}|) \\ &\quad \times \Theta(|\mathbf{k}| - |\mathbf{q}| \leq |\ell| \leq |\mathbf{k}| + |\mathbf{q}|) \quad , \quad (3.90) \end{aligned}$$

where the  $\Theta$ -function provides the limits of the integral so that the cosine exists between  $-1$  and  $1$ .

With the Matsubara sum evaluated and the momentum integration simplified one can now write down the second term in (3.77) in the most explicit form by assembling everything calculated above:

$$\begin{aligned} \int_Q \mathcal{G}_\sigma(Q + K) \mathcal{G}_\sigma(Q) &= \frac{1}{(2\pi)^2 |\mathbf{k}|} \int |\mathbf{q}| d|\mathbf{q}| \int |\ell| d|\ell| \int_{-\infty}^{\infty} \frac{d\ell_1}{2\pi} \int_{-\infty}^{\infty} \frac{d\ell_2}{2\pi} [1 + f(\ell_1)] f(\ell_2) \\ &\quad \times \frac{\exp[(\ell_2 - \ell_1)\beta] - 1}{i\omega - \ell_1 + \ell_2} \rho_\sigma(\ell_1, |\ell|) \rho_\sigma(\ell_2, |\mathbf{q}|) \\ &\quad \times \Theta(|\mathbf{k}| - |\mathbf{q}| \leq |\ell| \leq |\mathbf{k}| + |\mathbf{q}|) \quad . \quad (3.91) \end{aligned}$$



**The term**  $\text{Tr} \int_Q \mathcal{G}_\psi(K+Q) \mathcal{G}_\psi(Q)$

The next term to evaluate is  $\text{Tr} \int_Q \mathcal{G}_\psi(K+Q) \mathcal{G}_\psi(Q)$ . Written down explicitly it reads

$$\text{Tr} \int_Q \mathcal{G}_\psi(K+Q) \mathcal{G}_\psi(Q) = T \text{Tr} \sum_n \int \frac{d^3 \mathbf{q}}{(2\pi)^3} \mathcal{G}_\psi(i(\omega_n^F + \omega^B), \mathbf{k} + \mathbf{q}) \mathcal{G}_\psi(i\omega^F, \mathbf{q}) \quad . \quad (3.92)$$

Here  $\omega^F$  indicates that the frequencies are fermionic as in (3.37) while  $\omega^B$  denotes bosonic Matsubara frequencies of the form (3.18). The external lines of the self-energy are certainly bosonic because they belong to the  $\sigma$  self-energy. The internal lines of the loop are fermionic, so the internal Matsubara frequencies have to be fermionic. The trace runs over Dirac indices which are suppressed in the following. Again I start with going to the mixed representation

$$\mathcal{G}_\psi(i\omega, \mathbf{q}) = \int_0^\beta d\tau \exp(i\omega\tau) \mathcal{G}_\psi(\tau, \mathbf{q}) \quad , \quad (3.93)$$

which gives

$$\begin{aligned} \text{Tr} \int_Q \mathcal{G}_\psi(K+Q) \mathcal{G}_\psi(Q) &= \text{Tr} \int \frac{d^3 \mathbf{q}}{(2\pi)^3} \int_0^\beta d\tau \int_0^\beta d\tau' \mathcal{G}(\tau, \mathbf{q} + \mathbf{k}) \mathcal{G}(\tau', \mathbf{q}) \\ &\quad \times T \sum_n \exp[i(\omega_n^F + \omega^B)\tau] \exp(i\omega_n^F \tau') \quad . \end{aligned} \quad (3.94)$$

It is possible to carry out one  $\tau$  integration by using the relation (3.80). However, above it has been given for bosonic Matsubara-frequencies only, while here we have a mixture of fermionic and bosonic frequencies. To apply the relation nevertheless one can rearrange the exponentials of (3.94) in the following way:

$$\begin{aligned} T \sum_n \exp[i(\omega_n^F + \omega^B)\tau] \exp(i\omega_n^F \tau') &= T \sum_n \exp[i\omega_n^F(\tau + \tau') + i\omega^B \tau] \\ &= T \sum_n \exp\{i[(2n+1)\pi T(\tau + \tau') + 2\pi m T \tau]\} \\ &= T \sum_n \exp\{i[2n\pi T(\tau + \tau') + 2\pi m T \tau + \pi T(\tau + \tau')]\} \\ &= T \sum_n \exp[i\omega_n^B(\tau + \tau')] \exp(i\omega^B \tau) \exp[i\pi T(\tau + \tau')] \quad . \end{aligned} \quad (3.95)$$

The new index  $m$  counts the external Matsubara-frequencies. Now that the sum runs over a bosonic frequency the relation (3.80) can be applied with the result

$$T \sum_n \exp[i\omega_n^B(\tau + \tau')] = \sum_p \delta(\tau + \tau' - p\beta) \quad . \quad (3.96)$$

I can now carry out the  $\tau'$  integral by replacing  $\tau' = \beta - \tau$  because the sum only contributes for  $p = 1$ . The second exponential in the last line of (3.95) remains untouched but the third one becomes

$$\exp[i\pi T(\tau + \beta - \tau)] = e^{i\pi} = -1 \quad . \quad (3.97)$$

Therefore, the self-energy reads

$$\text{Tr} \int_Q \mathcal{G}_\psi(K+Q) \mathcal{G}_\psi(Q) = -T \text{Tr} \int \frac{d^3 \mathbf{q}}{(2\pi)^3} \int_0^\beta d\tau \mathcal{G}_\psi(\tau, \mathbf{k}+\mathbf{q}) \mathcal{G}_\psi(\beta-\tau, \mathbf{q}) \exp(i\omega^B \tau). \quad (3.98)$$

Now spectral functions can be introduced according to (3.34) as

$$\mathcal{G}_\psi(\tau, \mathbf{q}) = \int_{-\infty}^{\infty} \frac{d\ell}{2\pi} [1 - \tilde{f}(\ell)] \rho_\psi(\ell, \mathbf{q}) \exp(-\ell\tau) \quad (3.99)$$

with the fermi distribution function

$$\tilde{f}(\ell) = \frac{1}{e^{\beta\ell} + 1} \quad . \quad (3.100)$$

The result is thus

$$\begin{aligned} \text{Tr} \int_Q \mathcal{G}_\psi(K+Q) \mathcal{G}_\psi(Q) = & -\text{Tr} \int \frac{d^3 \mathbf{q}}{(2\pi)^3} \int_0^\beta d\tau \int_{-\infty}^{\infty} \frac{d\ell_1}{2\pi} \int_{-\infty}^{\infty} \frac{d\ell_2}{2\pi} [1 - \tilde{f}(\ell_1)] \tilde{f}(\ell_2) \\ & \times \rho_\psi(\ell_1, \mathbf{k} + \mathbf{q}) \rho_\psi(\ell_2, \mathbf{q}) \exp[i(\omega^B - \ell_1 + \ell_2)\tau] \quad . \end{aligned} \quad (3.101)$$

As before the  $\tau$  integration can be performed explicitly and one obtains

$$\begin{aligned} \text{Tr} \int_Q \mathcal{G}_\psi(K+Q) \mathcal{G}_\psi(Q) = & -\text{Tr} \int \frac{d^3 \mathbf{q}}{(2\pi)^3} \int_{-\infty}^{\infty} \frac{d\ell_1}{2\pi} \int_{-\infty}^{\infty} \frac{d\ell_2}{2\pi} [1 - \tilde{f}(\ell_1)] \tilde{f}(\ell_2) \\ & \times \rho_\psi(\ell_1, \mathbf{k} + \mathbf{q}) \rho_\psi(\ell_2, \mathbf{q}) \frac{\exp[(-\ell_1 + \ell_2)\beta] - 1}{i\omega^B - \ell_1 + \ell_2} \quad . \end{aligned} \quad (3.102)$$

The next step is to care for the momentum integration. This is a little bit more complicated than in the above case of the  $\sigma$  loop because the fermion spectral functions are functions of the momentum itself, not only its absolute value. Fortunately, the momentum dependence is known explicitly from the decomposition in  $\gamma$  matrices (3.74). For clarity I only consider the momentum structure of the term in question

$$\Pi(\mathbf{k}) = \text{Tr} \int \frac{d^3 \mathbf{q}}{(2\pi)^3} \rho_\psi(\mathbf{k} + \mathbf{q}) \rho_\psi(\mathbf{q}) \quad . \quad (3.103)$$

Inserting the decomposition (3.74) and evaluating the trace gives

$$\begin{aligned} \Pi(\mathbf{k}) = 4 \int \frac{d^3 \mathbf{q}}{(2\pi)^3} \left[ \rho_0(|\mathbf{k} + \mathbf{q}|) \rho_0(|\mathbf{q}|) - \frac{\mathbf{q} + \mathbf{k}}{|\mathbf{q} + \mathbf{k}|} \cdot \hat{\mathbf{q}} \rho_v(|\mathbf{k} + \mathbf{q}|) \rho_v(|\mathbf{q}|) \right. \\ \left. + \rho_m(|\mathbf{k} + \mathbf{q}|) \rho_m(|\mathbf{q}|) \right] \quad , \end{aligned} \quad (3.104)$$

so that the occurring spectral functions are no matrices any longer and only depend on the absolute value of the momentum. The following rules for the trace have been used [BRS95] (Note that the isospin adds an additional factor of  $\frac{1}{2}$ .)

$$\begin{aligned}\text{Tr}(\mathbb{1}) &= 4 \quad , \\ \text{Tr}(\text{odd number of } \gamma) &= 0 \quad , \\ \text{Tr}(\gamma^\mu \gamma^\nu) &= 4g^{\mu\nu} \quad , \\ \text{Tr}(\gamma^\mu \gamma^\nu \gamma^\rho \gamma^\sigma) &= 4(g^{\mu\nu}g^{\rho\sigma} - g^{\mu\rho}g^{\nu\sigma} + g^{\mu\sigma}g^{\nu\rho}) \quad .\end{aligned}\quad (3.105)$$

The integrals in (3.104) can now be integrated term by term. One observes that the first and the last term are of the same form as the second term in the  $\sigma$  self-energy (3.77). It was shown below (3.85) how to simplify it.

The second term in (3.104) is treated as follows: First I carry out the inner product

$$\begin{aligned}\int \frac{d^3\mathbf{q}}{(2\pi)^3} \rho_v(|\mathbf{k} + \mathbf{q}|) \rho_v(|\mathbf{q}|) \frac{\mathbf{q} + \mathbf{k}}{|\mathbf{q} + \mathbf{k}|} \cdot \frac{\mathbf{q}}{|\mathbf{q}|} \\ = \int \frac{d^3\mathbf{q}}{(2\pi)^3} \rho_v(|\mathbf{k} + \mathbf{q}|) \rho_v(|\mathbf{q}|) \frac{|\mathbf{q}|^2 + |\mathbf{k}||\mathbf{q}| \cos \Theta(\mathbf{k}, \mathbf{q})}{|\mathbf{q}| \sqrt{|\mathbf{k}|^2 + |\mathbf{q}|^2 + 2|\mathbf{k}||\mathbf{q}| \cos \Theta(\mathbf{k}, \mathbf{q})}} \quad .\end{aligned}\quad (3.106)$$

Again one can switch to spherical coordinates and substitute  $\ell = \mathbf{k} + \mathbf{q}$  where

$$\begin{aligned}|\ell|^2 &= \sqrt{|\mathbf{k}|^2 + |\mathbf{q}|^2 + 2|\mathbf{k}||\mathbf{q}| \cos \Theta(\mathbf{k}, \mathbf{q})} \\ \implies \cos \Theta &= \frac{|\ell|^2 - |\mathbf{k}|^2 - |\mathbf{q}|^2}{2|\mathbf{k}||\mathbf{q}|}\end{aligned}\quad (3.107)$$

and

$$d \cos \Theta = \frac{|\ell|}{|\mathbf{k}||\mathbf{q}|} d|\ell| \quad .\quad (3.108)$$

With this (3.106) becomes

$$\frac{1}{2(2\pi)^2|\mathbf{k}|} \int d|\mathbf{q}| \int d|\ell| \rho_v(|\mathbf{q}|) \rho_v(|\ell|) (|\ell|^2 - |\mathbf{k}|^2 + |\mathbf{q}|^2) \Theta(|\mathbf{k}| - |\mathbf{q}| \leq |\ell| \leq |\mathbf{k}| + |\mathbf{q}|) \quad (3.109)$$

where the  $\Theta$ -function restricts the integrals so that  $-1 \leq \cos \Theta \leq 1$ .

### Summary of the $\sigma$ self-energy

Now that all Matsubara sums are evaluated and all momentum integrals are reduced I can summarize the results and write down the self-energy of the  $\sigma$

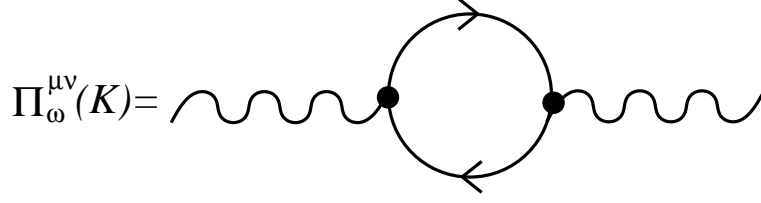


Figure 3.4: The self-energy of the  $\omega$ -meson in diagrammatic language.

meson explicitly

$$\begin{aligned}
 \Pi_\sigma(\omega, |\mathbf{k}|) = & -g_\sigma^2 \frac{4}{(2\pi)^4 |\mathbf{k}|} \int_{-\infty}^{\infty} d\ell_1 \int_{-\infty}^{\infty} d\ell_2 \frac{\exp[-(\ell_1 - \ell_2)\beta] - 1}{i\omega - \ell_1 + \ell_2} [1 - \tilde{f}(\ell_1)] \tilde{f}(\ell_2) \\
 & \times \int d|\mathbf{q}| \int d|\ell| \Theta(|\mathbf{k}| - |\mathbf{q}| \leq |\ell| \leq |\mathbf{k}| + |\mathbf{q}|) \\
 & \times \left[ |\mathbf{q}||\ell| \rho_0(\ell_1, |\ell|) \rho_0(\ell_2, |\mathbf{q}|) - \frac{1}{2} (|\ell|^2 - |\mathbf{k}|^2 + |\mathbf{q}|^2) \rho_v(\ell_1, |\ell|) \rho_v(\ell_2, |\mathbf{q}|) \right. \\
 & \quad \left. + |\mathbf{q}||\ell| \rho_m(\ell_1, |\ell|) \rho_m(\ell_2, |\mathbf{q}|) \right] \\
 & - 18 (4\lambda\hat{\sigma})^2 \frac{1}{(2\pi)^4 |\mathbf{k}|} \int_{-\infty}^{\infty} d\ell_1 \int_{-\infty}^{\infty} d\ell_2 \frac{\exp[-(\ell_1 - \ell_2)\beta] - 1}{i\omega - \ell_1 + \ell_2} [1 + f(\ell_1)] f(\ell_2) \\
 & \times \int d|\mathbf{q}| \int d|\ell| \Theta(|\mathbf{k}| - |\mathbf{q}| \leq |\ell| \leq |\mathbf{k}| + |\mathbf{q}|) |\mathbf{q}||\ell| \rho_\sigma(\ell_1, |\ell|) \rho_\sigma(\ell_2, |\mathbf{q}|) \\
 & + \frac{3}{\pi^3} \lambda \int_{-\infty}^{\infty} d\ell (1 + f(\ell)) \int_0^\infty d|\mathbf{q}| |\mathbf{q}|^2 \rho_\sigma(\ell, |\mathbf{q}|) \quad .
 \end{aligned} \tag{3.110}$$

The last term is the tadpole term which I do not discuss in detail here since it does not have an imaginary part.

### 3.2.2 The self-energy of the $\omega$ meson

The  $\omega$  meson self-energy consists of one term, only. It corresponds to the sunset diagram shown in fig. 3.4. From the Schwinger-Dyson equation it follows as

$$\begin{aligned}
 \Pi_\omega^{\mu\nu}(K) &= 2 \frac{\delta V_2[\hat{\sigma}, G_\sigma, G_{\omega\mu\nu}, G_\psi]}{\delta G_{\omega\mu\nu}(K)} \\
 &= g_\omega^2 \text{Tr} \int_Q \gamma^\mu \mathcal{G}_\psi(K+Q) \gamma^\nu \mathcal{G}_\psi(Q) \quad .
 \end{aligned} \tag{3.111}$$

The energy structure of this term is the same as that of the sunset diagram of the  $\sigma$  self-energy. The results can thus be transferred from above. One obtains

$$\text{Tr} \int_Q \gamma^\mu \mathcal{G}_\psi(K+Q) \gamma^\nu \mathcal{G}_\psi(Q) = -\text{Tr} \int \frac{d^3\mathbf{q}}{(2\pi)^3} \int_{-\infty}^{\infty} \frac{d\ell_1}{2\pi} \int_{-\infty}^{\infty} \frac{d\ell_2}{2\pi} [1 - \tilde{f}(\ell_1)] \tilde{f}(\ell_2)$$

$$\times \gamma^\mu \rho_\psi(\ell_1, \mathbf{k} + \mathbf{q}) \gamma^\nu \rho_\psi(\ell_2, \mathbf{q}) \frac{\exp[(-\ell_1 + \ell_2)\beta] - 1}{i\omega^B - \ell_1 + \ell_2} \quad . \quad (3.112)$$

In the following it is shown how to simplify the momentum integration. The general form of the momentum dependence, neglecting all factors that are independent of momentum, is

$$\Pi_\omega^{\mu\nu}(\mathbf{k}) = \text{Tr} \int \frac{d^3\mathbf{q}}{(2\pi)^3} \gamma^\mu \rho_\psi(\mathbf{k} + \mathbf{q}) \gamma^\nu \rho_\psi(\mathbf{q}) \quad . \quad (3.113)$$

As before the fermionic spectral functions are Dirac matrices which are decomposed according to (3.74). Expanding the product gives terms with different numbers of  $\gamma$  matrices. When the trace is built all terms with an odd number of  $\gamma$  matrices vanish. Leaving away these terms the  $\omega$  self-energy reads

$$\begin{aligned} \Pi_\omega^{\mu\nu}(\mathbf{k}) = & \text{Tr} \int \frac{d^3\mathbf{q}}{(2\pi)^3} \left[ \gamma^\mu \gamma_0 \gamma^\nu \gamma_0 \rho_0(|\mathbf{k} + \mathbf{q}|) \rho_0(|\mathbf{q}|) \right. \\ & - \gamma^\mu \gamma_0 \gamma^\nu \gamma^i \hat{q}^i \rho_0(|\mathbf{k} + \mathbf{q}|) \rho_v(|\mathbf{q}|) - \gamma^\mu \gamma^i \frac{(k^i + q^i)}{|\mathbf{k} + \mathbf{q}|} \gamma^\nu \gamma_0 \rho_v(|\mathbf{k} + \mathbf{q}|) \rho_0(|\mathbf{q}|) \\ & \left. + \gamma^\mu \gamma^i \frac{(k^i + q^i)}{|\mathbf{k} + \mathbf{q}|} \gamma^\nu \gamma^j \hat{q}^j \rho_v(|\mathbf{k} + \mathbf{q}|) \rho_v(|\mathbf{q}|) + \gamma^\mu \gamma^\nu \rho_m(|\mathbf{k} + \mathbf{q}|) \rho_m(|\mathbf{q}|) \right] \quad (3.114) \end{aligned}$$

where greek indices run over all four Lorentz components,  $\mu, \nu = 0, 1, 2, 3$ , while roman indices  $i$  and  $j$  run over the three spatial components,  $i, j = 1, 2, 3$ , only. The roman indices form the standard inner product. The next step is to evaluate the traces according to (3.105). The  $\omega$  self-energy then reads

$$\begin{aligned} \Pi_\omega^{\mu\nu}(\mathbf{k}) = & \int \frac{d^3\mathbf{q}}{(2\pi)^3} \left[ (2g^{\mu 0} g^{\nu 0} - g^{\mu\nu}) \rho_0(|\mathbf{k} + \mathbf{q}|) \rho_0(|\mathbf{q}|) \right. \\ & - (g^{\mu 0} g^{\nu i} + g^{\mu i} g^{\nu 0}) \frac{q^i}{|\mathbf{q}|} \rho_0(|\mathbf{k} + \mathbf{q}|) \rho_v(|\mathbf{q}|) \\ & - (g^{\mu i} g^{\nu 0} + g^{\mu 0} g^{\nu i}) \frac{k^i + q^i}{|\mathbf{k} + \mathbf{q}|} \rho_v(|\mathbf{k} + \mathbf{q}|) \rho_0(|\mathbf{q}|) \\ & + (g^{\mu i} g^{\nu k} - g^{\mu\nu} g^{ik} + g^{\mu k} g^{\nu i}) \frac{k^i + q^i}{|\mathbf{k} + \mathbf{q}|} \frac{q^k}{|\mathbf{q}|} \rho_v(|\mathbf{k} + \mathbf{q}|) \rho_v(|\mathbf{q}|) \\ & \left. + g^{\mu\nu} \rho_m(|\mathbf{k} + \mathbf{q}|) \rho_m(|\mathbf{q}|) \right] \quad (3.115) \end{aligned}$$

With this I can now calculate the necessary components of the  $\Pi_a$  and  $\Pi_b$  projection.

### The transverse projection

I start with the transverse projection of the  $\omega$  meson self-energy which is the negative of the  $\Pi_a$  projection. According to (3.64) it is defined as

$$\Pi^t(K) = \frac{1}{2}(\delta^{ij} - \hat{k}^i \hat{k}^j) \Pi_{\omega}^{ij}(K) \quad . \quad (3.116)$$

The actual calculation is straightforward. The substitution

$$\cos \Theta(\mathbf{k}, \mathbf{q}) = \frac{|\boldsymbol{\ell}|^2 - |\mathbf{q}|^2 - |\mathbf{k}|^2}{2|\mathbf{k}||\mathbf{q}|} \quad (3.117)$$

allows to simplify the integration as above and in the end the final result is

$$\begin{aligned} \Pi^t(k_0, |\mathbf{k}|) &= -g_{\omega}^2 \frac{2}{(2\pi)^4 |\mathbf{k}|} \int_{-\infty}^{\infty} d\ell_1 \int_{-\infty}^{\infty} d\ell_2 \frac{\exp[-(\ell_1 - \ell_2)\beta] - 1}{i\omega - \ell_1 + \ell_2} [1 - \tilde{f}(\ell_1)] \tilde{f}(\ell_2) \\ &\times \int d|\mathbf{q}| \int d|\boldsymbol{\ell}| \Theta(|\mathbf{k}| - |\mathbf{q}| \leq |\boldsymbol{\ell}| \leq |\mathbf{k}| + |\mathbf{q}|) \\ &\times |\mathbf{q}||\boldsymbol{\ell}| \left[ 2\rho_0(\ell_1, |\boldsymbol{\ell}|) \rho_0(\ell_2, |\mathbf{q}|) - \frac{1}{|\boldsymbol{\ell}|} (2|\mathbf{k}| \cos \Theta + 2|\mathbf{q}| \cos^2 \Theta) \right. \\ &\quad \left. \times \rho_v(\ell_1, |\boldsymbol{\ell}|) \rho_v(\ell_2, |\mathbf{q}|) - 2\rho_m(\ell_1, |\boldsymbol{\ell}|) \rho_m(\ell_2, |\mathbf{q}|) \right] \quad . \quad (3.118) \end{aligned}$$

### The longitudinal projection

The longitudinal projection is part of  $\Pi_b$ . It is defined as

$$\Pi^{\ell}(K) = \hat{k}_i \Pi_{\omega}^{ij}(K) \hat{k}_j \quad . \quad (3.119)$$

Again, a straightforward calculation leads to

$$\begin{aligned} \Pi^{\ell}(k_0, \mathbf{k}) &= -g_{\omega}^2 \frac{4}{(2\pi)^4 |\mathbf{k}|} \int_{-\infty}^{\infty} d\ell_1 \int_{-\infty}^{\infty} d\ell_2 \frac{\exp[-(\ell_1 - \ell_2)\beta] - 1}{i\omega - \ell_1 + \ell_2} [1 - \tilde{f}(\ell_1)] \tilde{f}(\ell_2) \\ &\times \int d|\mathbf{q}| \int d|\boldsymbol{\ell}| \Theta(|\mathbf{k}| - |\mathbf{q}| \leq |\boldsymbol{\ell}| \leq |\mathbf{k}| + |\mathbf{q}|) \\ &\times |\mathbf{q}||\boldsymbol{\ell}| \left[ \rho_0(\ell_1, |\boldsymbol{\ell}|) \rho_0(\ell_2, |\mathbf{q}|) + \frac{1}{|\boldsymbol{\ell}|} (-|\mathbf{q}| + 2|\mathbf{q}| \cos^2 \Theta + |\mathbf{k}| \cos \Theta) \right. \\ &\quad \left. \times \rho_v(\ell_1, |\boldsymbol{\ell}|) \rho_v(\ell_2, |\mathbf{q}|) - \rho_m(\ell_1, |\boldsymbol{\ell}|) \rho_m(\ell_2, |\mathbf{q}|) \right] \quad , \quad (3.120) \end{aligned}$$

where the same substitution as in (3.117) has been performed.

### The $\Pi_{\omega}^{00}$ component

Another part of the  $\Pi_b$  projection is the  $\Pi_{\omega}^{00}$  component of the vector-meson self-energy. It can be obtained from (3.115) by just inserting the respective indices

while all calculations are the same as for the above projections. The result is

$$\begin{aligned}
\Pi_{\omega}^{00}(k_0, \mathbf{k}) = & -g_{\omega}^2 \frac{4}{(2\pi)^4 |\mathbf{k}|} \int_{-\infty}^{\infty} d\ell_1 \int_{-\infty}^{\infty} d\ell_2 \frac{\exp[-(\ell_1 - \ell_2)\beta] - 1}{i\omega - \ell_1 + \ell_2} \\
& \times [1 - \tilde{f}(\ell_1)] \tilde{f}(\ell_2) \int d|\mathbf{q}| \int d|\ell| \Theta(|\mathbf{k}| - |\mathbf{q}| \leq |\ell| \leq |\mathbf{k}| + |\mathbf{q}|) \\
& \times [|\mathbf{q}||\ell| \rho_0(\ell_1, |\ell|) \rho_0(\ell_2, |\mathbf{q}|) \\
& + \frac{1}{2} (|\ell|^2 - |\mathbf{k}|^2 + |\mathbf{q}|^2) \rho_v(\ell_1, |\ell|) \rho_v(\ell_2, |\mathbf{q}|) \\
& + |\mathbf{q}||\ell| \rho_m(\ell_1, |\ell|) \rho_m(\ell_2, |\mathbf{q}|)] \quad .
\end{aligned} \tag{3.121}$$

**The component  $\hat{\mathbf{k}}^m \Pi_{\omega}^{0m}$**

Finally, the complete  $\Pi_b$  projection requires the determination of the term  $\hat{\mathbf{k}}^m \Pi_{\omega}^{0m}$ . Since the calculation is straightforward with the techniques described above, only the result is given here:

$$\begin{aligned}
\hat{\mathbf{k}}^m \Pi_{\omega}^{0m}(k_0, \mathbf{k}) = & -g_{\omega}^2 \frac{2}{(2\pi)^4 |\mathbf{k}|} \int_{-\infty}^{\infty} d\ell_1 \int_{-\infty}^{\infty} d\ell_2 \frac{\exp[-(\ell_1 - \ell_2)\beta] - 1}{i\omega - \ell_1 + \ell_2} \\
& \times [1 - \tilde{f}(\ell_1)] \tilde{f}(\ell_2) \int d|\mathbf{q}| \int d|\ell| \Theta(|\mathbf{k}| - |\mathbf{q}| \leq |\ell| \leq |\mathbf{k}| + |\mathbf{q}|) \\
& \times [|\ell|(|\ell|^2 - |\mathbf{q}|^2 - |\mathbf{k}|^2) \rho_0(\ell_1, |\ell|) \rho_v(\ell_2, |\mathbf{q}|) \\
& + |\mathbf{q}|(|\ell|^2 - |\mathbf{q}|^2 + |\mathbf{k}|^2) \rho_v(\ell_1, |\ell|) \rho_0(\ell_2, |\mathbf{q}|)] \quad .
\end{aligned} \tag{3.122}$$

### 3.2.3 The fermion self-energy

The self-energy of the fermions is obtained from the two-particle irreducible part of the potential (3.76) as

$$\begin{aligned}
\Sigma_{\psi}(k_0, \mathbf{k}) = & -\frac{\delta V_2[\hat{\sigma}, G_{\sigma}, G_{\omega\mu\nu}, G_{\psi}]}{\delta G_{\psi}(k_0, \mathbf{k})} \\
= & -g_{\sigma}^2 \int_Q \mathcal{G}_{\sigma}(K - Q) \mathcal{G}_{\psi}(Q) - g_{\omega}^2 \int_P \gamma^{\mu} \mathcal{G}_{\psi}(Q) \gamma^{\nu} \mathcal{G}_{\omega\mu\nu}(K - Q) \quad .
\end{aligned} \tag{3.123}$$

Thus there are two sunset diagrams corresponding to loops of the  $\sigma$  and the  $\omega$  meson as shown in fig. 3.5. Above the compact notation of a more complex substructure is given. It should be noted in particular that the fermion self-energy has a Dirac structure which requires decomposition as shown in (3.74). Again I treat the two terms separately.

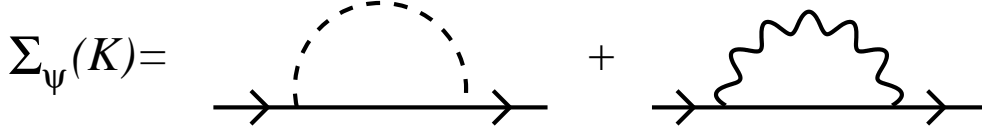


Figure 3.5: The self-energy of the fermion in diagrammatic language.

**The term**  $\int_Q \mathcal{G}_\sigma(K-Q) \mathcal{G}_\psi(Q)$

I start with the evaluation of the Matsubara sum

$$\Sigma_1(K) = \int_Q \mathcal{G}_\sigma(K-Q) \mathcal{G}_\psi(Q) = T \sum_n \int \frac{d^3 \mathbf{q}}{(2\pi)^3} \mathcal{G}_\sigma(i(\omega^F - \omega_n^F), |\mathbf{k} - \mathbf{q}|) \mathcal{G}_\psi(i\omega_n^F, \mathbf{q}) \quad . \quad (3.124)$$

The momenta  $K$  and  $Q$  both run on fermion lines so their Matsubara frequencies are fermionic. The difference  $K-Q$  runs on a boson line and in fact its frequency is bosonic because

$$\omega^F - \omega_n^F = (2m+1)\pi T - (2n+1)\pi T = 2(m-n)\pi T \quad (3.125)$$

is an even number where  $m$  counts the frequency of the external energy. As before I introduce the mixed representation

$$\mathcal{G}(i\omega, |\mathbf{q}|) = \int_0^\beta d\tau \exp(i\omega\tau) \mathcal{G}(\tau, |\mathbf{q}|) \quad (3.126)$$

to obtain

$$\begin{aligned} \Sigma_1(K) &= T \sum_n \int \frac{d^3 \mathbf{q}}{(2\pi)^3} \int_0^\beta d\tau \int_0^\beta d\tau' \mathcal{G}_\sigma(\tau, |\mathbf{k} - \mathbf{q}|) \mathcal{G}_\psi(\tau', \mathbf{q}) \\ &\quad \times \exp[i(\omega^F - \omega_n^F)\tau] \exp(i\omega_n^F \tau') \\ &= T \sum_n \int \frac{d^3 \mathbf{q}}{(2\pi)^3} \int_0^\beta d\tau \int_0^\beta d\tau' \mathcal{G}_\sigma(\tau, |\mathbf{k} - \mathbf{q}|) \mathcal{G}_\psi(\tau', \mathbf{q}) \\ &\quad \times \exp(i\omega^F \tau) \exp[i\omega_n^B(\tau' - \tau)] \exp(i\pi T(\tau' - \tau)) \\ &= \int \frac{d^3 \mathbf{q}}{(2\pi)^3} \int_0^\beta d\tau \mathcal{G}_\sigma(\tau, |\mathbf{k} - \mathbf{q}|) \mathcal{G}_\psi(\tau, \mathbf{q}) \exp(i\omega^F \tau) \quad . \quad (3.127) \end{aligned}$$

Here the fermionic Matsubara sum is combined with a bosonic one as in (3.125) so that relation (3.80) can be applied. Now spectral functions for bosons and fermions have to be introduced according to (3.12) and (3.34), respectively:

$$\begin{aligned} \mathcal{G}_\sigma(\tau, |\mathbf{k} - \mathbf{q}|) &= \int_{-\infty}^{\infty} \frac{d\ell_1}{2\pi} [1 + f(\ell_1)] \exp(-\ell_1 \tau) \rho_\sigma(\ell_1, |\mathbf{k} - \mathbf{q}|) \quad , \\ \mathcal{G}_\psi(\tau, \mathbf{q}) &= \int_{-\infty}^{\infty} \frac{d\ell_2}{2\pi} [1 - \tilde{f}(\ell_2)] \exp(-\ell_2 \tau) \rho_\psi(\ell_2, \mathbf{q}) \quad . \quad (3.128) \end{aligned}$$



The self-energy therefore becomes

$$\begin{aligned} \Sigma_1(K) = & \int \frac{d^3\mathbf{q}}{(2\pi)^3} \int_0^\beta d\tau \int_{-\infty}^\infty \frac{d\ell_1}{2\pi} \int_{-\infty}^\infty \frac{d\ell_2}{2\pi} [1 + f(\ell_1)][1 - \tilde{f}(\ell_2)] \\ & \times \exp(-\ell_1\tau) \exp(-\ell_2\tau) \rho_\sigma(\ell_1, |\mathbf{k} - \mathbf{q}|) \rho_\psi(\ell_2, \mathbf{q}) \quad . \end{aligned} \quad (3.129)$$

The  $\tau$  integration can be carried out explicitly and one obtains

$$\begin{aligned} \Sigma_1(K) = & - \int \frac{d^3\mathbf{q}}{(2\pi)^3} \int_{-\infty}^\infty \frac{d\ell_1}{2\pi} \int_{-\infty}^\infty \frac{d\ell_2}{2\pi} [1 + f(\ell_1)][1 - \tilde{f}(\ell_2)] \\ & \times \frac{\exp[(-\ell_1 - \ell_2)\beta] + 1}{i\omega^F - \ell_1 - \ell_2} \rho_\sigma(\ell_1, |\mathbf{k} - \mathbf{q}|) \rho_\psi(\ell_2, \mathbf{q}) \quad . \end{aligned} \quad (3.130)$$

The next step is to simplify the momentum integration. Therefore I only consider the momentum structure of the above term which is

$$\Sigma_1(\mathbf{k}) = \int \frac{d^3\mathbf{q}}{(2\pi)^3} \rho_\sigma(|\mathbf{k} - \mathbf{q}|) \rho_\psi(\mathbf{q}) \quad . \quad (3.131)$$

Note that the fermion spectral function depends on the momentum including its direction while the  $\sigma$  spectral function only depends on the absolute value of the momentum. However, the momentum structure of the fermion spectral function is known explicitly from the decomposition (3.74). I can therefore insert it here

$$\Sigma_1(\mathbf{k}) = \int \frac{d^3\mathbf{q}}{(2\pi)^3} \rho_\sigma(|\mathbf{k} - \mathbf{q}|) [\gamma^0 \rho_0(|\mathbf{q}|) - \boldsymbol{\gamma} \cdot \hat{\mathbf{q}} \rho_v(|\mathbf{q}|) + \rho_m(|\mathbf{q}|)] \quad . \quad (3.132)$$

The self-energy of the fermions obviously has a Dirac structure. Since I am interested in the components in the end, at some point the decomposition in this structure has to be performed. The momentum integration gets considerably easier when this decomposition is done now. The respective rules were summarized in (3.75).

First the *scalar part* is

$$\Sigma_{1m}(\mathbf{k}) = \frac{1}{4} \text{Tr} \Sigma_1(\mathbf{k}) = \int \frac{d^3\mathbf{q}}{(2\pi)^3} \rho_\sigma(|\mathbf{k} - \mathbf{q}|) \rho_m(|\mathbf{q}|) \quad . \quad (3.133)$$

The momentum integral of this expression is easily simplified as in the above cases with the substitution  $\boldsymbol{\ell} = \mathbf{k} - \mathbf{q}$  after switching to spherical coordinates so that

$$\cos \Theta = \frac{|\mathbf{k}|^2 + |\mathbf{q}|^2 - |\boldsymbol{\ell}|^2}{2|\mathbf{k}||\mathbf{q}|} \quad (3.134)$$

and

$$d \cos \Theta = - \frac{|\boldsymbol{\ell}|}{|\mathbf{k}||\mathbf{q}|} d|\boldsymbol{\ell}| \quad . \quad (3.135)$$

Note the different sign compared to the bosonic case, above. The result is

$$\Sigma_{1m}(\mathbf{k}) = \frac{1}{(2\pi)^2|\mathbf{k}|} \int |\mathbf{q}|d|\mathbf{q}| \int |\ell|d|\ell| \rho_\sigma(|\ell|) \rho_m(|\mathbf{q}|) \Theta(|\mathbf{k}| - |\mathbf{q}| \leq |\ell| \leq |\mathbf{k}| + |\mathbf{q}|) \quad . \quad (3.136)$$

The *time part*

$$\Sigma_{10}(\mathbf{k}) = \frac{1}{4} \text{Tr} \gamma_0 \Sigma_1(\mathbf{k}) = \int \frac{d^3\mathbf{q}}{(2\pi)^3} \rho_\sigma(|\mathbf{k} - \mathbf{q}|) \rho_0(|\mathbf{q}|) \quad (3.137)$$

is treated in an analogous way. With the same substitution as for the scalar part one obtains

$$\Sigma_{10}(\mathbf{k}) = \frac{1}{(2\pi)^2|\mathbf{k}|} \int |\mathbf{q}|d|\mathbf{q}| \int |\ell|d|\ell| \rho_\sigma(|\ell|) \rho_0(|\mathbf{q}|) \Theta(|\mathbf{k}| - |\mathbf{q}| \leq |\ell| \leq |\mathbf{k}| + |\mathbf{q}|) \quad . \quad (3.138)$$

Finally I calculate the *spatial component* as

$$\Sigma_{1v}(\mathbf{k}) = \frac{1}{4} \text{Tr}(\boldsymbol{\gamma} \cdot \hat{\mathbf{k}}) \Sigma_1(\mathbf{k}) = -\frac{1}{4} \text{Tr} \int \frac{d^3\mathbf{q}}{(2\pi)^3} \rho_\sigma(|\mathbf{k} - \mathbf{q}|) \rho_v(\mathbf{q}) (\boldsymbol{\gamma} \cdot \hat{\mathbf{k}}) (\boldsymbol{\gamma} \cdot \hat{\mathbf{q}}) \quad . \quad (3.139)$$

The two scalar products in this expression can be reduced to a cosine because

$$\frac{1}{4} \text{Tr}[(\boldsymbol{\gamma} \cdot \hat{\mathbf{k}})(\boldsymbol{\gamma} \cdot \hat{\mathbf{q}})] = \frac{1}{4} \text{Tr}[\gamma^i \gamma^j \hat{k}^i \hat{q}^j] = g^{ij} \hat{k}^i \hat{q}^j = -(\hat{k} \cdot \hat{q}) = -\cos \Theta \quad . \quad (3.140)$$

Now the same substitution  $\ell = \mathbf{k} - \mathbf{q}$  as for the other two parts can be performed and one obtains

$$\begin{aligned} \Sigma_{1v}(\mathbf{k}) &= \frac{1}{(2\pi)^2|\mathbf{k}|} \int |\mathbf{q}|d|\mathbf{q}| \int |\ell|d|\ell| \cos \Theta \rho_\sigma(|\ell|) \rho_v(|\mathbf{q}|) \\ &\quad \times \Theta(|\mathbf{k}| - |\mathbf{q}| \leq |\ell| \leq |\mathbf{k}| + |\mathbf{q}|) \quad , \end{aligned} \quad (3.141)$$

where the cosine is given by (3.134).

**The term**  $\int_P \gamma^\mu \mathcal{G}_\psi(Q) \gamma^\nu \mathcal{G}_{\omega\mu\nu}(K - Q)$

The evaluation of the Matsubara sum is exactly the same as for the other term, shown above. The result is therefore

$$\begin{aligned} \Sigma_2(K) &= \int_P \gamma^\mu \mathcal{G}_\psi(Q) \gamma^\nu \mathcal{G}_{\omega\mu\nu}(K - Q) \\ &= T \sum_n \int \frac{d^3\mathbf{q}}{(2\pi)^3} \gamma^\mu \mathcal{G}_\psi(i\omega_n^F, \mathbf{q}) \gamma^\nu \mathcal{G}_{\omega\mu\nu}(i(\omega^F - \omega_n^F), \mathbf{k} - \mathbf{q}) \\ &= - \int \frac{d^3\mathbf{q}}{(2\pi)^3} \int_{-\infty}^{\infty} \frac{d\ell_1}{2\pi} \int_{-\infty}^{\infty} \frac{d\ell_2}{2\pi} [1 + f(\ell_1)][1 - \tilde{f}(\ell_2)] \\ &\quad \times \frac{\exp[(-\ell_1 - \ell_2)\beta] + 1}{i\omega^F - \ell_1 - \ell_2} \gamma^\mu \rho_\psi(\ell_2, \mathbf{q}) \gamma^\nu \rho_{\omega\mu\nu}(\ell_1, \mathbf{k} - \mathbf{q}) \quad . \end{aligned} \quad (3.142)$$

For the further calculations the fermion spectral function is decomposed according to (3.75):

$$\begin{aligned}\Sigma_2(K) &= \int \frac{d^3\mathbf{q}}{(2\pi)^3} \gamma^\mu \rho_\psi(\mathbf{q}) \gamma^\nu \rho_{\omega\mu\nu}(\mathbf{k} - \mathbf{q}) \\ &= \int \frac{d^3\mathbf{q}}{(2\pi)^3} \gamma^\mu \left[ \underbrace{\gamma_0 \rho_0(|\mathbf{q}|)}_A - \underbrace{\boldsymbol{\gamma} \cdot \hat{\mathbf{q}} \rho_v(|\mathbf{q}|)}_B + \underbrace{\mathbb{1} \rho_m(|\mathbf{q}|)}_C \right] \gamma^\nu \rho_{\omega\mu\nu}(\mathbf{k} - \mathbf{q}) \quad .\end{aligned}\tag{3.143}$$

Eventually, I am interested in the different Dirac structures of this expression. As before it makes sense to do the decomposition first and calculate the momentum integral afterwards. For the sake of clarity the terms  $A$ ,  $B$  and  $C$  in (3.143) are treated separately in the following.

### Term A

I start with term  $A$  by decomposing it into the different Dirac structures. Term A reads

$$\Sigma_2^A(\mathbf{k}) = \int \frac{d^3\mathbf{q}}{(2\pi)^3} \gamma^\mu \gamma_0 \rho_0(|\mathbf{q}|) \gamma^\nu \rho_{\omega\mu\nu}(\mathbf{k} - \mathbf{q}) \quad .\tag{3.144}$$

The *scalar part*, which is proportional to the unit matrix, is zero because three  $\gamma$  matrices appear under the trace and the trace of an odd number of  $\gamma$  matrices is zero:

$$\Sigma_{2m}^A(\mathbf{k}) = \frac{1}{4} \text{Tr} \Sigma_2^A(\mathbf{k}) = 0 \quad .\tag{3.145}$$

Next I evaluate the *time part* of  $A$  which is

$$\begin{aligned}\Sigma_{20}^A(\mathbf{k}) &= \frac{1}{4} \text{Tr} \gamma^0 \Sigma_2^A(\mathbf{k}) \\ &= \frac{1}{4} \text{Tr} \int \frac{d^3\mathbf{q}}{(2\pi)^3} \gamma^0 \gamma^\mu \gamma^0 \gamma^\nu \rho_0(|\mathbf{q}|) \rho_{\omega\mu\nu}(\mathbf{k} - \mathbf{q}) \\ &= \int \frac{d^3\mathbf{q}}{(2\pi)^3} \rho_0(|\mathbf{q}|) \left( 2\rho_\omega^{00}(\mathbf{k} - \mathbf{q}) - \rho_{\omega\mu}^\mu(\mathbf{k} - \mathbf{q}) \right) \quad .\end{aligned}\tag{3.146}$$

The two components of the  $\omega$  spectral density can be reduced to the projections  $\rho_a$  and  $\rho_b$  by their definition:

$$\begin{aligned}\rho^{\mu\nu}(K) &= A^{\mu\nu} \rho_a(k_0, |\mathbf{k}|) + B^{\mu\nu} \rho_b(k_0, |\mathbf{k}|) \\ &= (-\delta^{ij} + \hat{k}^i \hat{k}^j) \rho_a(k_0, |\mathbf{k}|) + \left( g^{\mu\nu} + \delta^{ij} - \frac{K^\mu K^\nu}{K^2} - \hat{k}^i \hat{k}^j \right) \rho_b(k_0, |\mathbf{k}|)\end{aligned}\tag{3.147}$$

implying

$$\rho^{00}(K) = \left( 1 - \frac{k^{02}}{K^2} \right) \rho_b(k_0, |\mathbf{k}|)\tag{3.148}$$

and

$$\rho_\mu^\mu(K) = 2\rho_a(k_0, |\mathbf{k}|) + \rho_b(k_0, |\mathbf{k}|) \quad . \quad (3.149)$$

Hereby one obtains

$$\Sigma_{20}^A(\mathbf{k}) = \int \frac{d^3\mathbf{q}}{(2\pi)^3} \rho_0(|\mathbf{q}|) \left[ \left( 1 - 2 \frac{(k_0 - q_0)^2}{(K - Q)^2} \right) \rho_b(|\mathbf{k} - \mathbf{q}|) - 2\rho_a(|\mathbf{k} - \mathbf{q}|) \right] \quad . \quad (3.150)$$

Note that here the energy components of the momenta  $k_0$  and  $q_0$  enter from the  $\omega$  spectral density in the term proportional to  $\rho_b$ . In my calculation energies are Matsubara sums which were replaced by  $\ell_1 = k_0 - q_0$  when introducing the spectral functions in (3.129). Doing this replacement, introducing spherical coordinates and integrating the angles with the substitution (3.134) the term proportional to  $\rho_b$  in (3.150) becomes

$$\begin{aligned} \Sigma_{20b}^A(\mathbf{k}) &= \frac{2}{(2\pi)^2 |\mathbf{k}|} \int d|\mathbf{q}||\mathbf{q}| \int d|\ell||\ell| \frac{\ell_1^2}{\ell_1^2 - |\ell|^2} \rho_0(|\mathbf{q}|) \rho_b(|\ell|) \\ &\quad \times \Theta(|\mathbf{k}| - |\mathbf{q}| \leq |\ell| \leq |\mathbf{k}| + |\mathbf{q}|) \quad . \end{aligned} \quad (3.151)$$

The other terms of (3.150) are integrated with the substitution (3.134) as above. Putting everything together one obtains for the  $\gamma_0$  part of  $A$

$$\begin{aligned} \Sigma_{20}^A(\mathbf{k}) &= \frac{1}{(2\pi)^2 |\mathbf{k}|} \int d|\mathbf{q}||\mathbf{q}| \int d|\ell||\ell| \rho_0(|\mathbf{q}|) \left[ \left( 1 - \frac{2\ell_1^2}{\ell_1^2 - |\ell|^2} \right) \rho_b(|\ell|) - 2\rho_a(|\ell|) \right] \\ &\quad \times \Theta(|\mathbf{k}| - |\mathbf{q}| \leq |\ell| \leq |\mathbf{k}| + |\mathbf{q}|) \quad . \end{aligned} \quad (3.152)$$

Similar considerations can be done for the *spatial part* of  $\Sigma_A$  which is

$$\begin{aligned} \Sigma_{2v}^A(\mathbf{k}) &= \frac{1}{4} \text{Tr}(\boldsymbol{\gamma} \cdot \hat{\mathbf{k}} \Sigma_2^A(\mathbf{k})) \\ &= \frac{1}{4} \text{Tr}(\gamma^i \gamma^\mu \gamma^0 \gamma^\nu) \hat{k}^i \int \frac{d^3\mathbf{q}}{(2\pi)^3} \rho_0(|\mathbf{q}|) \rho_{\omega\mu\nu}(\mathbf{k} - \mathbf{q}) \\ &= 2 \int \frac{d^3\mathbf{q}}{(2\pi)^3} \hat{k}^i \rho_0(|\mathbf{q}|) \rho_\omega^{i0}(\mathbf{k} - \mathbf{q}) \quad . \end{aligned} \quad (3.153)$$

From (3.147) it follows that

$$\rho_\omega^{i0}(K - Q) = - \frac{(k^i - q^i)(k^0 - q^0)}{(K - Q)^2} \rho_b(K - Q) \quad . \quad (3.154)$$

Using  $(k^i - q^i)\hat{k}^i = |\mathbf{k}| - |\mathbf{q}| \cos \Theta$ , identifying  $k^0 - q^0 = \ell_1$  and doing the usual substitution (3.134) yields

$$\begin{aligned} \Sigma_{2v}^A(\mathbf{k}) &= - \frac{2}{(2\pi)^2 |\mathbf{k}|} \int d|\mathbf{q}||\mathbf{q}| \int d|\ell||\ell| \left[ \frac{\ell_1}{\ell_1^2 - |\ell|^2} (|\mathbf{k}| - |\mathbf{q}| \cos \Theta) \right] \\ &\quad \times \rho_b(|\ell|) \rho_0(|\mathbf{q}|) \Theta(|\mathbf{k}| - |\mathbf{q}| \leq |\ell| \leq |\mathbf{k}| + |\mathbf{q}|) \quad . \end{aligned} \quad (3.155)$$

**Term B**

Next I want to consider term  $B$  of (3.143) which reads

$$\Sigma_2^B(\mathbf{k}) = \int \frac{d^3\mathbf{q}}{(2\pi)^3} \gamma^\mu \boldsymbol{\gamma} \cdot \hat{\mathbf{q}} \rho_v(|\mathbf{q}|) \gamma^\nu \rho_{\omega\mu\nu}(\mathbf{k} - \mathbf{q}) \quad . \quad (3.156)$$

Again the number of  $\gamma$  matrices is odd so the part proportional to  $\mathbb{1}$  vanishes:

$$\Sigma_{2m}^B(\mathbf{k}) = \frac{1}{4} \text{Tr} \Sigma_2^B(\mathbf{k}) = 0 \quad . \quad (3.157)$$

The part proportional to  $\gamma_0$  is

$$\begin{aligned} \Sigma_{20}^B(\mathbf{k}) &= \frac{1}{4} \text{Tr} \gamma_0 \Sigma_2^B(\mathbf{k}) \\ &= 2 \int \frac{d^3\mathbf{q}}{(2\pi)^3} \hat{q}^i \rho_v(|\mathbf{q}|) \rho_\omega^{0i}(\mathbf{k} - \mathbf{q}) \\ &= -\frac{2}{(2\pi)^2 |\mathbf{k}|} \int d|\mathbf{q}| |\mathbf{q}| \int d|\boldsymbol{\ell}| |\boldsymbol{\ell}| \left[ \frac{\ell_1 (|\mathbf{k}| \cos \Theta - |\mathbf{q}|)}{\ell_1^2 - |\boldsymbol{\ell}|^2} \right] \\ &\quad \times \rho_b(|\boldsymbol{\ell}|) \rho_v(|\mathbf{q}|) \Theta(|\mathbf{k}| - |\mathbf{q}| \leq |\boldsymbol{\ell}| \leq |\mathbf{k}| + |\mathbf{q}|) \quad , \end{aligned} \quad (3.158)$$

where the calculations are analogous to those of term A.

The last part of  $B$  is the spatial component. It is given by

$$\begin{aligned} \Sigma_{2v}^B(\mathbf{k}) &= \frac{1}{4} \text{Tr}(\boldsymbol{\gamma} \cdot \hat{\mathbf{k}}) \Sigma_2^B(\mathbf{k}) \\ &= \frac{1}{4} \text{Tr}(\gamma^i \gamma^\mu \gamma^j \gamma^\nu) \int \frac{d^3\mathbf{q}}{(2\pi)^3} \hat{k}^i \hat{q}^j \rho_v(|\mathbf{q}|) \rho_{\omega\mu\nu}(\mathbf{k} - \mathbf{q}) \\ &= \int \frac{d^3\mathbf{q}}{(2\pi)^3} \hat{k}^i \hat{q}^j \rho_v(|\mathbf{q}|) \left[ 2\rho_\omega^{ij}(\mathbf{k} - \mathbf{q}) - g^{ij} \rho_{\omega\mu}^\mu(\mathbf{k} - \mathbf{q}) \right] \quad . \end{aligned} \quad (3.159)$$

For the further calculation the tensor decomposition (3.147) is inserted for the  $\omega$  spectral density. The product with  $\hat{k}^i$  and  $\hat{q}^j$  can then be calculated straightforwardly and one obtains

$$\begin{aligned} \Sigma_{2v}^B(\mathbf{k}) &= \frac{1}{(2\pi)^2 |\mathbf{k}|} \int d|\mathbf{q}| |\mathbf{q}| \int d|\boldsymbol{\ell}| |\boldsymbol{\ell}| \rho_v(|\mathbf{q}|) \\ &\quad \left[ \frac{2}{|\boldsymbol{\ell}|^2} (|\mathbf{k}| - |\mathbf{q}| \cos \Theta) (|\mathbf{k}| \cos \Theta - |\mathbf{q}|) \rho_a(|\boldsymbol{\ell}|) \right. \\ &\quad \left. + \left( \left( -\frac{2}{\ell_1^2 - |\boldsymbol{\ell}|^2} - \frac{2}{|\boldsymbol{\ell}|} \right) (|\mathbf{k}| - |\mathbf{q}| \cos \Theta) (|\mathbf{k}| \cos \Theta - |\mathbf{q}|) \right. \right. \\ &\quad \left. \left. + \cos \Theta \right) \rho_b(|\boldsymbol{\ell}|) \right] \Theta(|\mathbf{k}| - |\mathbf{q}| \leq |\boldsymbol{\ell}| \leq |\mathbf{k}| + |\mathbf{q}|) \quad , \end{aligned} \quad (3.160)$$

where the substitution (3.134) has performed.

### Term C

The last term to consider is term  $C$  from (3.143) which is

$$\Sigma_2^C(\mathbf{k}) = \int \frac{d^3\mathbf{q}}{(2\pi)^3} \gamma^\mu \mathbb{1}_{\rho_m(|\mathbf{q}|)} \gamma^\nu \rho_{\omega\mu\nu}(\mathbf{k} - \mathbf{q}) \quad . \quad (3.161)$$

Since this term contains two  $\gamma$  matrices, only the scalar component, proportional to the unit matrix contributes. The time component

$$\Sigma_{20}^C(\mathbf{k}) = \frac{1}{4} \text{Tr} \gamma_0 \Sigma_2^C(\mathbf{k}) = 0 \quad , \quad (3.162)$$

and the space component

$$\Sigma_{2v}^C(\mathbf{k}) = \frac{1}{4} \text{Tr}(\boldsymbol{\gamma} \cdot \mathbf{k}) \Sigma_2^C(\mathbf{k}) = 0 \quad (3.163)$$

vanish. The scalar component is straightforwardly derived as

$$\begin{aligned} \Sigma_{2m}^C(\mathbf{k}) &= \frac{1}{4} \text{Tr} \Sigma_2^C(\mathbf{k}) \\ &= \int \frac{d^3\mathbf{q}}{(2\pi)^3} \gamma^\mu \gamma^\nu \rho_m(|\mathbf{q}|) \rho_{\omega\mu\nu}(\mathbf{k} - \mathbf{q}) \\ &= \frac{1}{(2\pi)^2 |\mathbf{k}|} \int d|\mathbf{q}| |\mathbf{q}| \int d|\boldsymbol{\ell}| |\boldsymbol{\ell}| \rho_m(|\mathbf{q}|) [2\rho_a(|\boldsymbol{\ell}|) + \rho_b(|\boldsymbol{\ell}|)] , \end{aligned} \quad (3.164)$$

where again the substitution (3.134) has been performed.

Now that all fermion terms have been calculated I can put them together to obtain the complete fermion self-energies.

### Summary of the fermion self-energy

I now summarize all terms calculated above, sorting together those proportional to the different Dirac structures. Both terms of the self-energy are taken into account.

The part proportional to  $\gamma_0$  is

$$\begin{aligned} \Sigma_0(i\omega^F, \mathbf{k}) &= \frac{1}{(2\pi)^4 |\mathbf{k}|} \int |\mathbf{q}| d|\mathbf{q}| \int |\boldsymbol{\ell}| d|\boldsymbol{\ell}| \Theta(|\mathbf{k}| - |\mathbf{q}| \leq |\boldsymbol{\ell}| \leq |\mathbf{k}| + |\mathbf{q}|) \\ &\times \int_{-\infty}^{\infty} d\ell_1 \int_{-\infty}^{\infty} d\ell_2 [1 + f(\ell_1)] [1 - \tilde{f}(\ell_2)] \frac{\exp[(-\ell_1 - \ell_2)\beta] + 1}{i\omega^F - \ell_1 - \ell_2} \\ &\times \left\{ g_\sigma^2 \rho_\sigma(\ell_1, |\boldsymbol{\ell}|) \rho_0(\ell_2, |\mathbf{q}|) \right. \\ &+ g_\omega^2 \left[ \left( 1 - \frac{2\ell_1^2}{\ell_1^2 - |\boldsymbol{\ell}|^2} \right) \rho_b(\ell_1, |\boldsymbol{\ell}|) - 2\rho_a(\ell_1, |\boldsymbol{\ell}|) \right] \rho_0(\ell_2, |\mathbf{q}|) \\ &\left. + 2g_\omega^2 \rho_b(\ell_1, |\boldsymbol{\ell}|) \rho_v(\ell_2, |\mathbf{q}|) \left( \frac{\ell_1 (|\mathbf{k}| \cos \Theta - |\mathbf{q}|)}{\ell_1^2 - |\boldsymbol{\ell}|^2} \right) \right\} , \end{aligned} \quad (3.165)$$

where

$$\cos \Theta = \frac{|\mathbf{k}|^2 + |\mathbf{q}|^2 - |\boldsymbol{\ell}|^2}{2|\mathbf{k}||\boldsymbol{\ell}|} . \quad (3.166)$$

The part proportional to the spatial components of the gamma matrices  $\boldsymbol{\gamma}$  is

$$\begin{aligned} \Sigma_v(i\omega^F, \mathbf{k}) = & -\frac{1}{(2\pi)^4|\mathbf{k}|} \int |\mathbf{q}|d|\mathbf{q}| \int |\boldsymbol{\ell}|d|\boldsymbol{\ell}| \Theta(|\mathbf{k}| - |\mathbf{q}| \leq |\boldsymbol{\ell}| \leq |\mathbf{k}| + |\mathbf{q}|) \\ & \times \int_{-\infty}^{\infty} d\ell_1 \int_{-\infty}^{\infty} d\ell_2 [1 + f(\ell_1)][1 - \tilde{f}(\ell_2)] \frac{\exp[(-\ell_1 - \ell_2)\beta] + 1}{i\omega^F - \ell_1 - \ell_2} \\ & \times \left\{ -g_\sigma^2 \cos \Theta \rho_\sigma(\ell_1, |\boldsymbol{\ell}|) \rho_v(\ell_2, |\mathbf{q}|) \right. \\ & + g_\omega^2 \left[ 2 \left( \frac{\ell_1^2}{\ell_1^2 - |\boldsymbol{\ell}|^2} (|\mathbf{k}| - |\mathbf{q}| \cos \Theta) \right) \rho_b(\ell_1, |\boldsymbol{\ell}|) \rho_0(\ell_2, |\mathbf{q}|) \right. \\ & + \left[ \frac{2}{|\boldsymbol{\ell}|^2} (|\mathbf{k}| - |\mathbf{q}| \cos \Theta) (|\mathbf{k}| \cos \Theta - |\mathbf{q}|) \rho_a(\ell_1, |\boldsymbol{\ell}|) \right. \\ & + \left( 2 \left( -\frac{1}{\ell_1^2 - |\boldsymbol{\ell}|^2} - \frac{1}{|\boldsymbol{\ell}|^2} \right) (|\mathbf{k}| - |\mathbf{q}| \cos \Theta) (|\mathbf{k}| \cos \Theta - |\mathbf{q}|) + \cos \Theta \right) \\ & \left. \left. \left. \times \rho_b(\ell_1, |\boldsymbol{\ell}|) \right] \rho_v(\ell_2, |\mathbf{q}|) \right] \right\} . \end{aligned} \quad (3.167)$$

Finally the scalar part which is proportional to the unit matrix is

$$\begin{aligned} \Sigma_m(i\omega^F, \mathbf{k}) = & \frac{1}{(2\pi)^4|\mathbf{k}|} \int |\mathbf{q}|d|\mathbf{q}| \int |\boldsymbol{\ell}|d|\boldsymbol{\ell}| \Theta(|\mathbf{k}| - |\mathbf{q}| \leq |\boldsymbol{\ell}| \leq |\mathbf{k}| + |\mathbf{q}|) \\ & \times \int_{-\infty}^{\infty} d\ell_1 \int_{-\infty}^{\infty} d\ell_2 [1 + f(\ell_1)][1 - \tilde{f}(\ell_2)] \frac{\exp[(-\ell_1 - \ell_2)\beta] + 1}{i\omega^F - \ell_1 - \ell_2} \\ & \left[ g_\sigma^2 \rho_\sigma(\ell_1, |\boldsymbol{\ell}|) \rho_m(\ell_2, |\mathbf{q}|) + g_\omega^2 [2\rho_a(\ell_1, |\boldsymbol{\ell}|) + \rho_b(\ell_1, |\boldsymbol{\ell}|)] \rho_m(\ell_2, |\mathbf{q}|) \right] . \end{aligned} \quad (3.168)$$

### 3.2.4 The imaginary parts of the self-energies

In all self-energies calculated above the imaginary unit occurs only in the denominator. Therefore, the imaginary part of the self-energies can be calculated with help of the Dirac identity

$$\text{Im} \left( \frac{1}{R + i\epsilon} \right) = -i\pi \delta(R) , \quad (3.169)$$

where  $R$  is a real number. One energy integral breaks down in the imaginary part because of the delta function.

### 3.2.5 Self-energies and spectral functions

The above set of equations is self-consistent because the spectral functions are connected to the full propagators via

$$\rho(K) = 2 \text{Im} \mathcal{G}(K) \quad (3.170)$$

as shown in (3.27). With the self-energies the inverse of the propagators are

$$\mathcal{G}^{-1}(K) = \mathcal{D}^{-1} + \text{Re}\Pi(K) + i \text{Im}\Pi(K) \quad (3.171)$$

where the self-energy consists of a real and an imaginary part. As mentioned above the treatment of the real part is rather difficult because it contains divergences which have to be renormalized. I therefore restrict myself to the case where they are set to zero by hand.

To actually calculate the spectral density according to (3.170) it is necessary to invert the inverse propagator first. This is trivial for bosons but a little more complicated for fermions. Afterwards the imaginary part is determined.

The bosonic spectral function is obtained straightforwardly as

$$\begin{aligned} \rho_{\text{Boson}}(K) &= 2 \text{Im} \frac{1}{-K^2 + m^2 + i \text{Im}\Pi(K)} \\ &= -2 \frac{\text{Im}\Pi(K)}{(K^2 - m^2)^2 + \text{Im}\Pi(K)^2} \quad . \end{aligned} \quad (3.172)$$

For the fermions I carry out the inversion first. The inverse propagator is

$$\begin{aligned} \mathcal{G}_\psi^{-1}(K) &= -K_\mu \gamma^\mu + M_\psi + i \text{Im}\Sigma(K) \quad \underbrace{[+\text{Re}\Sigma(K)]}_{:=0} \\ &= -k_0 \gamma^0 + \mathbf{k} \cdot \boldsymbol{\gamma} + M_\psi + i \left( \text{Im}\Sigma_0 \gamma^0 - \text{Im}\Sigma_v(\hat{\mathbf{k}} \cdot \boldsymbol{\gamma}) + \text{Im}\Sigma_m \mathbb{1} \right) \quad , \end{aligned} \quad (3.173)$$

where the real part is again set to zero. One observes that this expression is of the form

$$\mathcal{G}_\psi^{-1} = -\ell_\mu \gamma^\mu + n \quad (3.174)$$

where

$$\begin{aligned} \ell_0 &= k_0 - i \text{Im}\Sigma_0(K) \quad , \\ \boldsymbol{\ell} &= \mathbf{k} - i \text{Im}\Sigma_v(K) \hat{\mathbf{k}} \quad , \\ n &= M_\psi + i \text{Im}\Sigma_m(K) \quad . \end{aligned} \quad (3.175)$$

This structure can be inverted as

$$\mathcal{G}_\psi(K) = (-\ell_\mu \gamma^\mu + n)^{-1} = \left[ \underbrace{(-\ell_\mu \gamma^\mu - n)(-\ell_\mu \gamma^\mu + n)}_{(\ell^2 - n^2)} \right]^{-1} (-\ell_\mu \gamma^\mu - n) \quad (3.176)$$

so the full propagator of the fermions is

$$\mathcal{G}_\psi(K) = \frac{-k_0 \gamma^0 + \mathbf{k} \cdot \boldsymbol{\gamma} - M_\psi + i \text{Im}\Sigma_0 \gamma^0 - i \text{Im}\Sigma_v(\hat{\mathbf{k}} \cdot \boldsymbol{\gamma}) - i \text{Im}\Sigma_m}{(k_0 - i \text{Im}\Sigma_0)^2 - (\mathbf{k} - i \text{Im}\Sigma_v \hat{\mathbf{k}})^2 - (M_\psi + i \text{Im}\Sigma_m)^2} \quad . \quad (3.177)$$



The imaginary part of this can be determined as usual by multiplying the numerator and denominator by the complex conjugated of the denominator. Afterwards the decomposition into the Dirac structure is performed as in (3.75). The actual calculation is straightforward but comprises some lengthy expressions so I only state the results. With the denominator

$$N := \left( K^2 - M_\psi^2 - \text{Im } \Sigma_0^2 + \text{Im } \Sigma_v^2 + \text{Im } \Sigma_m^2 \right)^2 + 4 \left( |\mathbf{k}| \text{Im } \Sigma_v - k_0 \text{Im } \Sigma_0 - M_\psi \text{Im } \Sigma_m \right)^2, \quad (3.178)$$

the part proportional to  $\gamma_0$  is

$$\begin{aligned} \frac{1}{2} \rho_0(K) &= \text{Im } \mathcal{G}_0(K) \\ &= \frac{1}{N} \left( 2k_0 |\mathbf{k}| \text{Im } \Sigma_v - 2k_0^2 \text{Im } \Sigma_0 - 2M_\psi k_0 \text{Im } \Sigma_m + k_0^2 \text{Im } \Sigma_0 \right. \\ &\quad \left. - \mathbf{k}^2 \text{Im } \Sigma_0 - \text{Im } \Sigma_0^3 + \text{Im } \Sigma_0 \text{Im } \Sigma_v^2 + \text{Im } \Sigma_0 \text{Im } \Sigma_m^2 - M_\psi^2 \text{Im } \Sigma_0 \right). \end{aligned} \quad (3.179)$$

The  $\gamma$  part turns out to be

$$\begin{aligned} \frac{1}{2} \rho_v(K) &= \text{Im } \mathcal{G}_v(K) \\ &= -\frac{1}{N} \left( -2\mathbf{k}^2 \text{Im } \Sigma_v + 2|\mathbf{k}|k_0 \text{Im } \Sigma_0 + 2|\mathbf{k}|M_\psi \text{Im } \Sigma_m - k_0^2 \text{Im } \Sigma_v \right. \\ &\quad \left. + \mathbf{k}^2 \text{Im } \Sigma_v + \text{Im } \Sigma_v \text{Im } \Sigma_0^2 - \text{Im } \Sigma_v^3 - \text{Im } \Sigma_v \text{Im } \Sigma_m^2 + M_\psi^2 \text{Im } \Sigma_v \right), \end{aligned} \quad (3.180)$$

and the part proportional to the unit matrix is

$$\begin{aligned} \frac{1}{2} \rho_m(K) &= \text{Im } \mathcal{G}_m(K) \\ &= \frac{1}{N} \left( 2M_\psi |\mathbf{k}| \text{Im } \Sigma_v - 2M_\psi k_0 \text{Im } \Sigma_0 - 2M_\psi^2 \text{Im } \Sigma_m - k_0^2 \text{Im } \Sigma_m \right. \\ &\quad \left. + \mathbf{k}^2 \text{Im } \Sigma_m + \text{Im } \Sigma_m \text{Im } \Sigma_0^2 - \text{Im } \Sigma_m \text{Im } \Sigma_v^2 - \text{Im } \Sigma_m^3 + M_\psi^2 \text{Im } \Sigma_m \right). \end{aligned} \quad (3.181)$$

Due to this connection the self-energies obviously enter themselves via the spectral function. The problem is therefore said to be *self-consistent*. However, there are some restraints that should be mentioned. In this work only the imaginary parts of the self-energies are taken into account for reasons of renormalization as well as computational effort. The complete spectral functions would also contain the real parts which have been set to zero above.

### 3.2.6 Sum rules

For the numerical solution of the above set of integral equations space-time and energy-momentum space have to be discretized. Sometimes it happens that the spectral function becomes very narrow with a small width. Then the lattice might be too coarse to resolve the spectral function and contribution to the propagator strength gets lost. One can repair the spectral function with help of *sum rules* which control whether the spectrum is complete. The sum rules follow directly from the commutation relations as shown in the following.

#### Sum rule for the scalar meson

The most simple case is the scalar meson again. To deduce a sum rule consider the Fourier transform

$$D^>(t) - D^<(t) = \int_{-\infty}^{\infty} \frac{dk_0}{2\pi} e^{-ik_0 t} (D^>(k_0) - D^<(k_0)) \quad . \quad (3.182)$$

The derivative of this with respect to time is

$$\frac{d}{dt} (D^>(t) - D^<(t)) = -i \int_{-\infty}^{\infty} \frac{dk_0}{2\pi} k_0 e^{-ik_0 t} \underbrace{(D^>(k_0) - D^<(k_0))}_{\rho(k_0)} \quad , \quad (3.183)$$

where the spectral function has been identified from its definition (3.7). From the definition of the two-point functions (3.2) and (3.3) it is known that

$$D^>(t) - D^<(t) = \langle [\hat{\phi}(t), \hat{\phi}(0)] \rangle_{\beta} \quad . \quad (3.184)$$

With the canonical equal-time commutation relation

$$\left[ \hat{\phi}(t), \frac{d}{dt'} \hat{\phi}(t') \right]_{t'=t} = i \quad (3.185)$$

the left-hand side of (3.183) can then be written as

$$\frac{d}{dt} (D^>(t) - D^<(t)) = \left\langle \left[ \frac{d}{dt} \hat{\phi}(t), \hat{\phi}(0) \right] \right\rangle_{\beta} = -i \quad . \quad (3.186)$$

Inserting this into (3.183) and taking the limit  $t \rightarrow 0$  yields the sum rule

$$\int_{-\infty}^{\infty} \frac{dk_0}{2\pi} k_0 \rho(k_0) = 1 \quad . \quad (3.187)$$

It provides a test if the spectral function is complete. Missing contributions can result from three effects. First, the width of the spectral function might be too small to be resolved by the lattice spacing. In this case the spectral function

can be repaired by numerically adding a box function, which is a function that is constant over a step in the energy lattice, whose strength just repairs the sum rule. The second violation of the sum rule can result from the fact that I only consider the imaginary parts of the sunset diagrams when calculating the spectral functions. Finally, it might happen that the lattice is too small to cover the whole spectral function. If the width is sufficiently large I correct the spectral function by an overall factor.

### Sum rules for the vector meson

The spectral functions of the vector mesons are projected onto their longitudinal and transverse direction as shown in section 3.1.2. Both projections have different sum rules [Pos98]. The canonical commutation relation for massive vector mesons is

$$[\omega^i(\mathbf{x}, t), \pi^j(\mathbf{y}, t)] = i\delta^{ij}\delta^3(\mathbf{x} - \mathbf{y}) \quad (3.188)$$

with the canonical conjugate field

$$\pi^i(\mathbf{x}, t) = \frac{\partial \mathcal{L}}{\partial(\partial_0 \omega^i)} = \partial^0 \omega^i - \partial^i \omega^0 = F^{0i} \quad (3.189)$$

where  $F^{\mu\nu}$  is the field-strength tensor and

$$\mathcal{L} = -\frac{1}{4}F_{\mu\nu}F^{\mu\nu} + \frac{1}{2}m_\omega^2\omega_\mu\omega^\mu \quad (3.190)$$

is the Proca Lagrangian. Inserting the Lagrangian into the Euler-Lagrange equation one finds that

$$\omega^0 = -\frac{1}{m_\omega^2}\partial_i F^{i0} \quad (3.191)$$

With this expression and the canonical conjugate field (3.189) the time-derivative of the field can be calculated:

$$\partial^0 \omega^i = \pi^i + \frac{1}{m_\omega^2}\partial^i \partial_j \pi^j \quad (3.192)$$

With this the canonical commutation relation (3.188) leads to

$$[\partial^0 \omega^i(t, \mathbf{x}), \omega^j(0, 0)] = ig^{ij}\delta^3(\mathbf{x}) + i\frac{1}{m_\omega^2}\partial^j \partial_k g^{ki}\delta^3(\mathbf{x}) \quad , \quad (3.193)$$

so according to the definition of  $D^<$  and  $D^>$

$$\frac{d}{dt} (D^{ij>}(t) - D^{ij<}(t)) = \langle [\partial^0 \omega^i(t), \omega^j(0)] \rangle_\beta = ig^{ij} - i\frac{1}{m_\omega^2}k^i k^j \quad (3.194)$$

As for the scalar mesons above I take the time derivative of the Fourier transform

$$\frac{d}{dt} \left( D^{ij>}(t) - D^{ij<}(t) \right) = -i \int_{-\infty}^{\infty} \frac{dk_0}{2\pi} k_0 e^{-ik_0 t} \underbrace{\left( D^{ij>}(k_0) - D^{ij<}(k_0) \right)}_{\rho^{ij}(k_0)} \quad (3.195)$$

and insert (3.194). After calculating the limit  $t \rightarrow 0$  one obtains the sum rule

$$\int_{-\infty}^{\infty} \frac{dk_0}{2\pi} k_0 \rho^{ij}(k_0) = -g^{ij} + \frac{1}{m_\omega^2} k^i k^j \quad . \quad (3.196)$$

The *transverse projector*  $T^{\mu\nu} = -A^{\mu\nu} = \frac{1}{2}(\delta^{ij} - \hat{k}^i \hat{k}^j)$  can now be applied directly on the above sum rule because it is independent of energy and can therefore be put under the integral. The sum rule for the transverse projection is thus

$$\int_{-\infty}^{\infty} \frac{dk_0}{2\pi} k_0 \rho^t(k_0) = \frac{1}{2}(\delta^{ij} - \hat{k}^i \hat{k}^j) \left( -g^{ij} + \frac{1}{m_\omega^2} k^i k^j \right) = 1 \quad . \quad (3.197)$$

For the  $\rho_b$  *projection* I proceed analogously. From the canonical commutation relations it follows that

$$\begin{aligned} [\partial^0 \omega^0(t, \mathbf{x}), \omega^0(0, 0)] &= -\frac{1}{m_\omega^2} [\partial^0 \omega^0(t, \mathbf{x}), \partial_j F^{j0}] \\ &= -\frac{1}{m_\omega^2} [\partial_i \omega^i(t, \mathbf{x}), \partial_j \pi^j(0, 0)] \\ &= -\frac{1}{m_\omega^2} \partial_i \partial_j [\omega^i(t, \mathbf{x}), \pi^j(0, 0)] \\ &= -\frac{i}{m_\omega^2} g^{ij} \partial_i \partial_j \delta^3(\mathbf{x}) \quad . \end{aligned} \quad (3.198)$$

From the definition of  $D^{<}$  and  $D^{>}$  one obtains

$$\frac{d}{dt} \left( D^{00>}(t) - D^{00<}(t) \right) = \left\langle [\partial^0 \omega^0(t), \omega^0(0)] \right\rangle_\beta = -\frac{|\mathbf{k}|^2}{m_\omega^2} \quad . \quad (3.199)$$

Again, the time derivative of the Fourier transform is

$$\frac{d}{dt} \left( D^{00>}(t) - D^{00<}(t) \right) = -i \int_{-\infty}^{\infty} \frac{dk_0}{2\pi} k_0 e^{-ik_0 t} \underbrace{\left( D^{00>}(k_0) - D^{00<}(k_0) \right)}_{\rho^{00}(k_0)} \quad (3.200)$$

Inserting (3.199) and calculating the limit  $t \rightarrow 0$  yields

$$\int_{-\infty}^{\infty} \frac{dk_0}{2\pi} k_0 \rho_\omega^{00}(K) = -\frac{|\mathbf{k}|^2}{m_\omega^2} \quad (3.201)$$

If the spectral function is transverse, i.e. ,  $\rho_\omega^{\mu\nu} K_\mu = 0$ , the time part  $\rho_\omega^{00}$  can be connected to the  $\rho_b$  projection as

$$\rho_b = -\frac{K^2}{|\mathbf{k}|^2} \rho^{00} \quad . \quad (3.202)$$

Therefore, the above relation (3.201) gives a sum rule for  $\rho_b$

$$\int_{-\infty}^{\infty} \frac{dk_0}{2\pi} k_0 \frac{m_\omega^2}{K^2} \rho^b(k_0) = 1 \quad . \quad (3.203)$$

### Sum rules for fermions

Also for the fermions a sum rule can be derived. The derivation is analogous to the boson case but based on the anti commutation relation instead of the commutation-relation. As for bosons case I start from the Fourier transform

$$S^>(t) - S^<(t) = \int_{-\infty}^{\infty} \frac{dk_0}{2\pi} e^{-ik_0 t} \underbrace{(S^>(k_0) - S^<(k_0))}_{\rho_\psi(k_0)} \quad . \quad (3.204)$$

The left-hand side is by definition

$$\begin{aligned} S_{ab}^>(t) - S_{ab}^<(t) &= \langle \psi_a(t) \bar{\psi}_b(0) \rangle_\beta + \langle \bar{\psi}_b(0) \psi_a(t) \rangle_\beta \\ &= \left\langle \left\{ \psi_a(t), \psi_b^\dagger(0) \right\} \right\rangle_\beta \gamma_{cb}^0 \\ &= \delta_{ac} \gamma_{cb}^0 = \gamma_{ab}^0 \quad , \end{aligned} \quad (3.205)$$

where the anti-commutation relation  $\{\psi_a(t), \psi_b^\dagger(t')\}|_{t=t'} = \delta_{ab}$  has been used. Inserting this into (3.204) gives

$$\mathbb{1} = \int_{-\infty}^{\infty} \frac{dk_0}{2\pi} e^{-ik_0 t} \gamma^0 \rho_\psi(k_0) \quad (3.206)$$

and calculating the trace yields a sum rule if one inserts the decomposition (3.74):

$$\lim_{t \rightarrow 0} \frac{1}{4} \text{Tr} \int_{-\infty}^{\infty} \frac{dk_0}{2\pi} e^{-ik_0 t} \gamma^0 \rho_\psi(k_0) = \int_{-\infty}^{\infty} \frac{dk_0}{2\pi} \rho_0(k_0) = 1 \quad . \quad (3.207)$$

Again the limit  $t \rightarrow 0$  has been performed. Obviously there is a sum rule for the  $\gamma_0$  component of the fermion spectral function, only. In fact there is no possibility to control the other contributions but it will turn out in the numerical calculations that these parts have a width which is sufficiently large to be covered by the lattice spacing. However, a possible real part is only taken into account on Hartree level.

### 3.2.7 The field equation and the masses

The vertex of the  $\sigma$  sunset diagram contains the expectation value of the  $\sigma$  field explicitly. It is therefore necessary to determine the value of this field. This is done by solving the field equation which follows from the potential (2.2) with the two-particle irreducible contributions (3.76). As in the Hartree case the field equation is obtained from eq. (1.108). Taking into account all possible contributions it reads

$$0 = m_\sigma^2 \hat{\sigma} + 4\lambda \hat{\sigma}^3 + 12\lambda \hat{\sigma} \int_Q \mathcal{G}_\sigma(Q) - g_\sigma \int_Q \text{Tr} \mathcal{G}_\psi(Q) - 6(4\lambda)^2 \hat{\sigma} \int_P \int_Q \mathcal{G}_\sigma(P-Q) \mathcal{G}_\sigma(P) \mathcal{G}_\sigma(Q) = 0 \quad . \quad (3.208)$$

Those terms containing integrals and Matsubara sums have to be evaluated. The integral over the  $\sigma$  loop is calculated straightforwardly with the above techniques. Going to mixed representation and inserting the spectral function as above gives

$$\int_Q \mathcal{G}_\sigma(Q) = \frac{2}{(2\pi)^2} \int \frac{d\ell}{2\pi} \int d|\mathbf{q}| |\mathbf{q}|^2 (1 + f(\ell)) \rho_\sigma(\ell, |\mathbf{q}|) \quad . \quad (3.209)$$

The constant term under the integral is divergent. It is therefore subtracted. Also the fermion loop can be calculated quickly. The evaluation of the Matsubara sum and the introduction of the spectral function gives

$$\int_Q \text{Tr} \mathcal{G}_\psi(Q) = \text{Tr} \int \frac{d^3 \mathbf{q}}{(2\pi)^3} \int \frac{d\ell}{2\pi} (1 - \tilde{f}(\ell)) \rho_\psi(\ell, \mathbf{q}) \quad . \quad (3.210)$$

Again, the decomposition into the Dirac structure (3.74) has to be performed. However, if the trace is taken, only the part proportional to the unit-matrix survives because  $\gamma$  matrices are traceless. The momentum integral can then be simplified as above to yield

$$\begin{aligned} \int_Q \text{Tr} \mathcal{G}_\psi(Q) &= \frac{8}{(2\pi)^2} \int_{-\infty}^{\infty} \frac{d\ell}{2\pi} \int d|\mathbf{q}| |\mathbf{q}|^2 (1 - \tilde{f}(\ell)) \rho_m(\ell, |\mathbf{q}|) \\ &= \frac{8}{(2\pi)^2} \int_0^{\infty} \frac{d\ell}{2\pi} \int d|\mathbf{q}| |\mathbf{q}|^2 (1 - 2\tilde{f}(\ell)) \rho_m(\ell, |\mathbf{q}|) \quad , \quad (3.211) \end{aligned}$$

where the anti-symmetry of  $\rho_m$  has been used. The constant term in the second row is divergent and therefore has to be subtracted, so that one finally obtains

$$\int_Q \text{Tr} \mathcal{G}_\psi(Q) = -\frac{16}{(2\pi)^2} \int_0^{\infty} \frac{d\ell}{2\pi} \int d|\mathbf{q}| |\mathbf{q}|^2 \tilde{f}(\ell) \rho_m(\ell, |\mathbf{q}|) \quad . \quad (3.212)$$

The sunset term of (3.208) bears some problems in its treatment. Because there is no possibility to calculate any momentum integrals analytically the full expression contains six integrals. The computational effort of this is too high to include this

term. However, it turned out that this term is (at  $T = 200$  MeV) by a factor of  $10^4$  smaller than the tadpole term. I therefore neglect it in this work. I concentrate on the influence of the decay widths on the fields and masses, so I calculate those analogous to the Hartree approximation where the sunset diagrams were not included.

If the condensate has been calculated by solving the above field equation the masses of the mesons and the fermions can be determined. Therefor an ansatz of a propagator with an effective mass (2.7) and (2.8) is made in the Schwinger-Dyson equations (2.5). These masses are regarded as the effective masses of the respective particles. However, unlike in Hartree approximation the tadpole diagram is calculated with the spectral functions. The fermion mass is thus

$$M_\psi = m_\psi + g_\sigma \sigma \quad (3.213)$$

and the  $\sigma$  mass is

$$M_\sigma^2 = m_\sigma^2 + 12\lambda\hat{\sigma}^2 + 12\lambda\frac{2}{(2\pi)^2} \int \frac{d\ell}{2\pi} \int d|\mathbf{q}||\mathbf{q}|^2 (1 + f(\ell)) \rho_\sigma(\ell, |\mathbf{q}|) \quad . \quad (3.214)$$

The mass of the  $\omega$  meson is again constant.

### 3.3 Numerical solution of the self-consistent equations

To actually determine the spectral functions of the involved fields the coupled equations for the  $\sigma$ -meson self-energy (3.110), the  $\omega$ -meson self-energies (3.118) and (3.120) as well as the fermionic contributions (3.165), (3.167) and (3.168) have to be solved. The problem is self-consistent as stated above. The spectral functions are functions of energy and momentum that is integrated over. The equations are solved on a discretized energy-momentum lattice where self-energies as well as spectral functions are calculated at each point.

The calculation is done iteratively within the following algorithm:

1. The calculation is initialized with the spectral functions of the free particles (3.21) for bosons and (3.38) for fermions which are known analytically. The  $\sigma$  field and the masses are those from the Hartree calculations.
2. The spectral function is inserted into the equations for the imaginary parts of the self-energies. In this step the momentum and energy integrals are calculated, which is the most time-consuming task. To minimize the effort the  $\Theta$ -function is evaluated beforehand and only permitted momenta are taken into account (see fig. 3.6).
3. From the imaginary parts of the self-energies determined in step 2 the new spectral functions are calculated as shown in section 3.2.5.

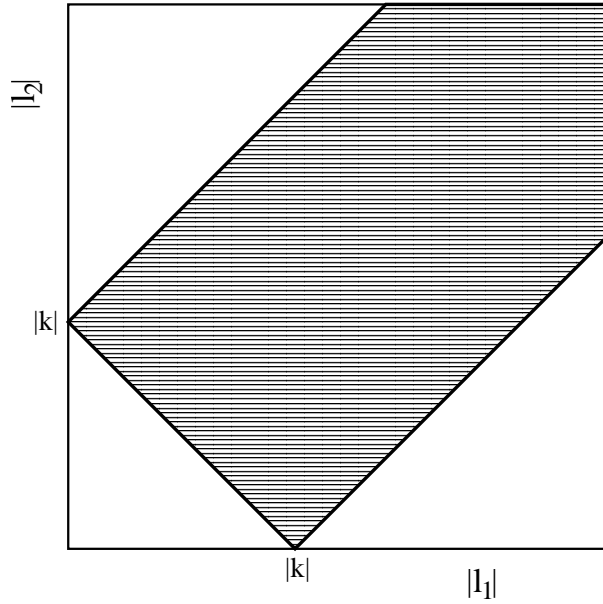


Figure 3.6: The hatched region shows the momenta which are integrated over. The momentum integration is constrained by the Theta function. Note that the size of this region depends on the external momentum.

4. If a sum rule exists, its fulfillment is checked and if necessary a correction is made. This holds for the boson spectral functions as well as the  $\gamma_0$  part of the fermion spectral function. The correction is done either by adding a  $\delta$  function at the mass shell or by multiplying the spectral function by an overall factor.
5. With the resulting spectral functions the  $\sigma$  field and the masses  $M_\psi$  as well as  $M_\sigma$  are determined according to section 3.2.7.
6. With the new spectral functions,  $\sigma$  field, and masses the calculation starts again from step 2.

The algorithm resembles a simple fix-point scheme. Its convergence shows that the approximation applied is meaningful in the following sense. In the first step one starts with the tree-level propagators to construct the self-energies. Those self-energies are therefore built from tree-level propagators. In the next iteration the new propagators enter the self-energies. Those are not tree-level anymore but contain the dressing of the step before. Convergence of this algorithm means that the higher-order contributions get smaller and smaller. This iterative procedure has been widely used for self-consistent calculations at non-zero density and temperature in relativistic (e.g. [MR05, KM93]) and non-relativistic (e.g. [LEL<sup>+</sup>00, LLLM02, FLM03a]) approaches with the interactions based on nucleon-nucleon scattering data.

There are two problems to bear in mind. On the one hand, the lattice spacing must not be too wide to be able to resolve the peak of the spectral function at



the mass-shell. On the other hand, the lattice must not be too small in energy-momentum space because otherwise significant parts of the spectral functions might be cut off. However, a calculation of more than around  $200 \times 200$  points would be too time consuming with the computing power currently at hand. It turned out that for my calculations a total extent of the lattice of 5730 MeV in energy and momentum direction is reasonable if the temperature is below 200 MeV. For temperatures of 200 MeV and higher a range of 11460 MeV is necessary. Although the final spectral functions are not much broader than at lower temperatures, it emerged that intermediate states of the calculation are too broad to fit onto the small lattice. The loss of spectral strength does not happen unnoticed. If the lattice spacing is too wide and the delta function gets lost, some spectral functions either show a change of their sign at positive energies or vanish completely after a certain number of iterations. If, on the other hand, the lattice range is not sufficient the maxima of some spectral functions cross the lightcone in the  $|\mathbf{k}|$ - $k_0$ -plane. The number of grid points was  $191 \times 191$  which yields a lattice spacing of 30 MeV in the calculations below 200 MeV while for the larger energy-momentum range the lattice spacing is 60 MeV. The correction of the sum rules has been carried out in the following way: At temperatures below 175 MeV all corrections were done by adding a delta function at the mass-shell because the width of the spectral functions was very small. The delta function was realized as a box function on three lattice points with a height that just corrected the sum rule. Between  $T = 175$  MeV and  $T = 200$  MeV the  $\gamma_0$  component of the fermion spectral function has been corrected by an overall factor while the meson spectral functions were corrected by a delta function. Above  $T = 200$  MeV all sum rules were corrected by factors. The factors had values between approximately 0.7 and 1.3. At very high momenta, at the edge of the lattice, the factors became higher because the spectral function was truncated.

For practical purposes the momentum integral has been split into 32 pieces which could be calculated in parallel. At the end of each step all parts were put together and the next iteration step was initialized.

The convergence was checked by calculating the ratio of the spectral function in two successive iterations. Very good convergence (ratios of 0.99999 to 1.0000) was achieved in 15 to 20 iteration steps.

## 3.4 Results in the improved approximation

### 3.4.1 The masses and the fields

The masses and the  $\sigma$  field are calculated as described in section 3.2.7. The equations are the same as in Hartree approximation but the integrals over the propagators are computed with the spectral functions inserted as shown in section 3.2.7 instead of the Ansätze with fixed masses. The Hartree results can be

reproduced if the spectral functions are delta functions at the mass-shell.

The studies presented here therefore show the effects which result from the non-zero width of the spectral functions as well as from the interaction of fermions with mesons. It should be noted that, as shown in eq. (3.211), the scalar part of the fermion spectral function  $\rho_m$  enters the field equation (3.208) while there is no sum rule for this. Therefore, in principle it could happen that some contribution to this term of the field equation gets lost by falling between the lattice spacing or because the real part is neglected for the sunset diagrams. The observations for  $\rho_0$ , where the sum rule has to be corrected by around 20 %, suggest that  $\rho_m$  might be uncertain by a similar amount which would not change the qualitative findings.

The left part of figure 3.7 shows the  $\sigma$  field as a function of temperature, comparing tree-level, Hartree, and the calculation where all diagrams of figure 2.1 are taken into account (except for the real parts of the sunset diagrams). The latter will be referred to as *improved approximation* in the following. The right-hand part shows the mass of the fermion in the same approximations. Both quantities are directly correlated via (3.213). One observes a significant influence of the additional interactions and the non-zero widths. The rise of the field and the decrease of the fermion mass are smoother than in the other approximations. The

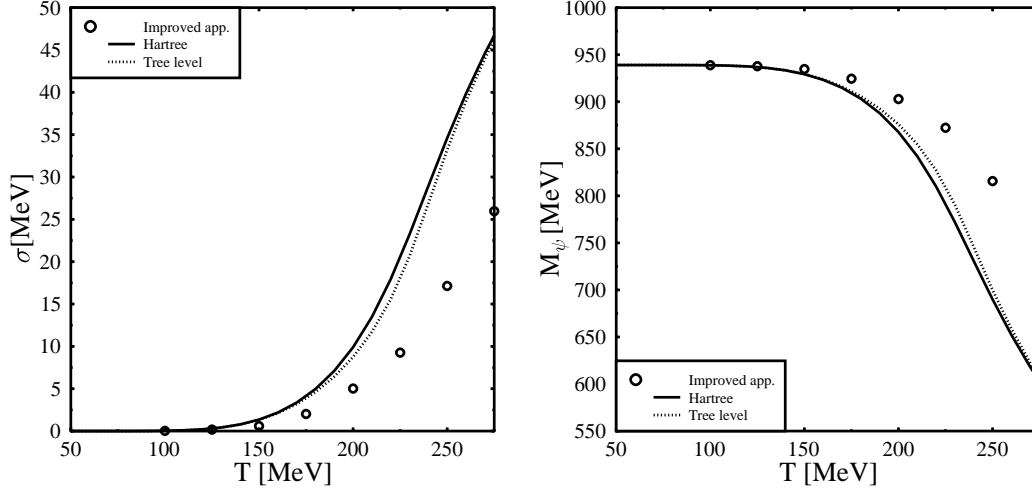


Figure 3.7: The left figure shows the  $\sigma$  field in comparison of the Hartree-, tree-level and the improved approximation. The right diagram shows the same comparison for the mass of the fermion.

difference compared to tree-level is much more pronounced than in the Hartree calculations. This is due to the fact that in the Hartree approximation the only difference compared to tree-level is the additional term in the  $\sigma$ -meson mass

which emerges from the tadpole diagram. The field equation is influenced only indirectly because it contains the  $\sigma$ -meson mass. Although the terms which occur in the improved approximation are the same as in Hartree, all propagators are now expressed by their spectral functions which also include the sunset diagrams of figure 2.1 and have a non-zero decay width. It will be shown later in the discussion of the spectral functions that the widths of the spectral functions increase with higher temperatures (compare figures 3.11, 3.16 and 3.19). Therefore, the influence of the non-zero width should increase with temperature as well. To demonstrate this figure 3.8 shows the two integral terms of the  $\sigma$  field equation (3.208), individually. The left-hand figure shows the integral over  $\mathcal{G}_\sigma$  while the right-hand side shows the scalar density which is the term proportional to  $g_\sigma$ . Actually, both terms deviate from each other in the different approximations. The first thing to observe is that the scalar density is bigger than the integral

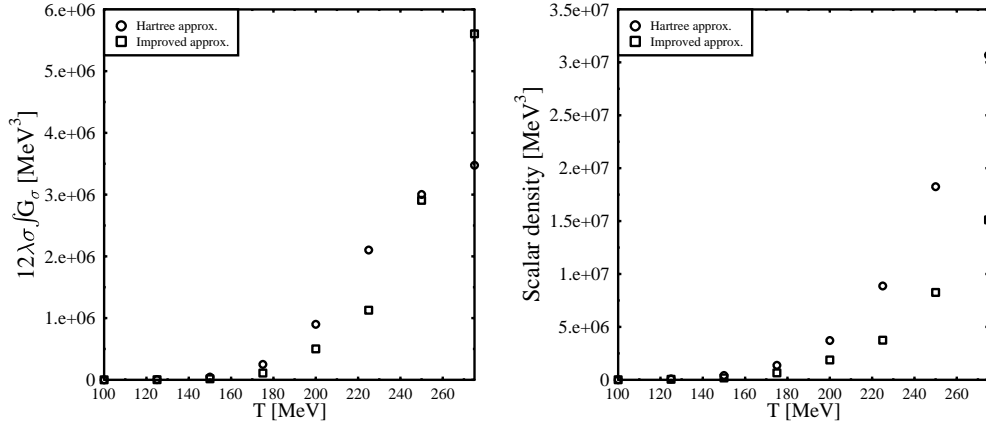


Figure 3.8: The two integral terms of the  $\sigma$  field equation. The left-hand figure shows the integral over  $\mathcal{G}_\sigma$  while the right-hand side shows the scalar density which is the term proportional to  $g_\sigma$ .

over  $\mathcal{G}_\sigma$  by an order of magnitude. It therefore dominates the behavior of the  $\sigma$  field and the fermion mass. Indeed it rises much more slowly in the improved approximation than on Hartree level. The difference between the two resembles the difference in the  $\sigma$  field and the fermion mass. Physically, a slower decrease of the fermion mass leads to a suppressed production of particle anti-particle pairs whereby the scalar density, which is essentially the sum of particle number and anti-particle number (compare eq. 2.32), rises more slowly. This induces a slower increase of the scalar field.

Figure 3.9 shows the mass of the  $\sigma$  meson as a function of temperature comparing tree-level, Hartree approximation, and the improved approximation. Its behavior is determined by the  $\sigma$  field and the same integral over  $\mathcal{G}_\sigma$  which appears in the field equation. The latter is shown in the left-hand diagram in figure 3.8. This term emerges from the tadpole diagram. Here the two levels of approximation

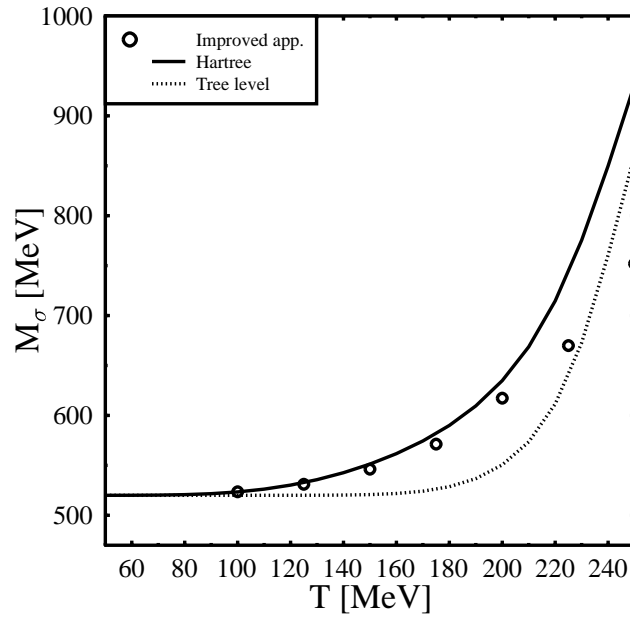


Figure 3.9: Mass of the  $\sigma$  field in the Hartree, tree-level, and the improved approximation.

show a qualitatively different behavior. In the Hartree approximation it rises most rapidly between temperatures of 175 MeV and 250 MeV but saturates at higher temperatures. This explains why the difference compared to tree-level is most pronounced in this very region and becomes smaller again at higher temperatures. In contrast, in the improved approximation the respective term rises almost exponentially without reaching saturation within the calculated range of temperatures. As a result, Hartree and improved approximation first stay close to each other but diverge at higher temperatures.

The calculations show that the non-zero width indeed changes the results compared to a quasi-particle approach. It significantly smoothens the crossover which is usually observed in the Walecka model.

Calculations beyond  $T = 275$  MeV are unfortunately not practicable because the lattice size is restricted by computing power as discussed in section 3.3.

For further studies it might be interesting to investigate the influence of the non-zero width when more baryons are taken into account. It was shown in [WTM<sup>+</sup>87] that a real first-order phase transition is observed in the Walecka model if baryon resonances are included in the calculation. This is because the scalar density, which triggers the  $\sigma$  field and thus the fermion mass, is connected to the number of fermion-anti-fermion pairs. If the number of fermion degrees of freedom is increased by including more baryon species, the scalar density changes much more quickly with temperature and therefore also the  $\sigma$  field. It should be investigated if this phase transition is also softened when non-zero widths are taken

into account.

### 3.4.2 The bosonic spectral functions

I now want to show the spectral functions explicitly as they result from the self-consistent calculations.

#### The $\sigma$ meson

Figure 3.10 shows the spectral function of the  $\sigma$  meson at four different temperatures. It exhibits a non-trivial structure for  $\omega > |\mathbf{k}|$ , but drops exponentially for  $\omega < |\mathbf{k}|$  which is shown exemplary in figure 3.12 on the right-hand side. In the following the lower bounds of the figures are chosen to bring out the other structures more clearly while the decrease in the space-like region of the energy-momentum plane is truncated by hand.

The most prominent feature in the spectral function is a pronounced maximum at the mass-shell which is highest at small momenta and decreases with higher momenta. Especially at low temperatures it is very sharp and approaches a delta function. As mentioned in section 3.3 the sum rule is checked at each momentum and is corrected by adding a delta function at the mass-shell or multiplying an overall factor, if necessary. The peak gets broader at higher temperatures. Its width  $\Gamma$  is connected to the imaginary part shown in fig. 3.12 on the left-hand side by [Wel83]

$$\Gamma(\omega) = -\frac{\text{Im } \Pi(\omega)}{\omega} \quad , \quad (3.215)$$

evaluated at the mass-shell  $\omega = \sqrt{M^2 + k^2}$ . It is shown in fig. 3.11 for the  $\sigma$  meson at different temperatures. The most important thing to observe is the increase of the decay width with temperature. Another prominent feature of figure 3.10 is the decay of the  $\sigma$  meson into a baryon anti-baryon pair which occurs at an energy of two times the baryon mass at  $k = 0$  MeV. It appears as a rapid increase of the spectral function at the respective energy. At low temperatures the onset is relatively sharp. With higher temperatures it becomes smeared out, on the one hand because the effective baryon mass decreases and on the other hand because the mass-shell peak becomes broader. Eventually the peak and the decay overlap.

The decay structure itself essentially maintains its shape, however, it becomes sharper with higher momenta. Together with the mass-shell peak becoming more narrow a deep trough is formed at high momenta at temperatures around 200 MeV. However, it should be mentioned that this structure might be unphysical because two spectral functions ( $\rho_m$  and  $\rho_q$ ) that enter here cannot be corrected by sum rules. I found that in general a missing correction can lead to such structures.

The  $\sigma$  meson also couples to itself in the sunset diagram, allowing for a decay

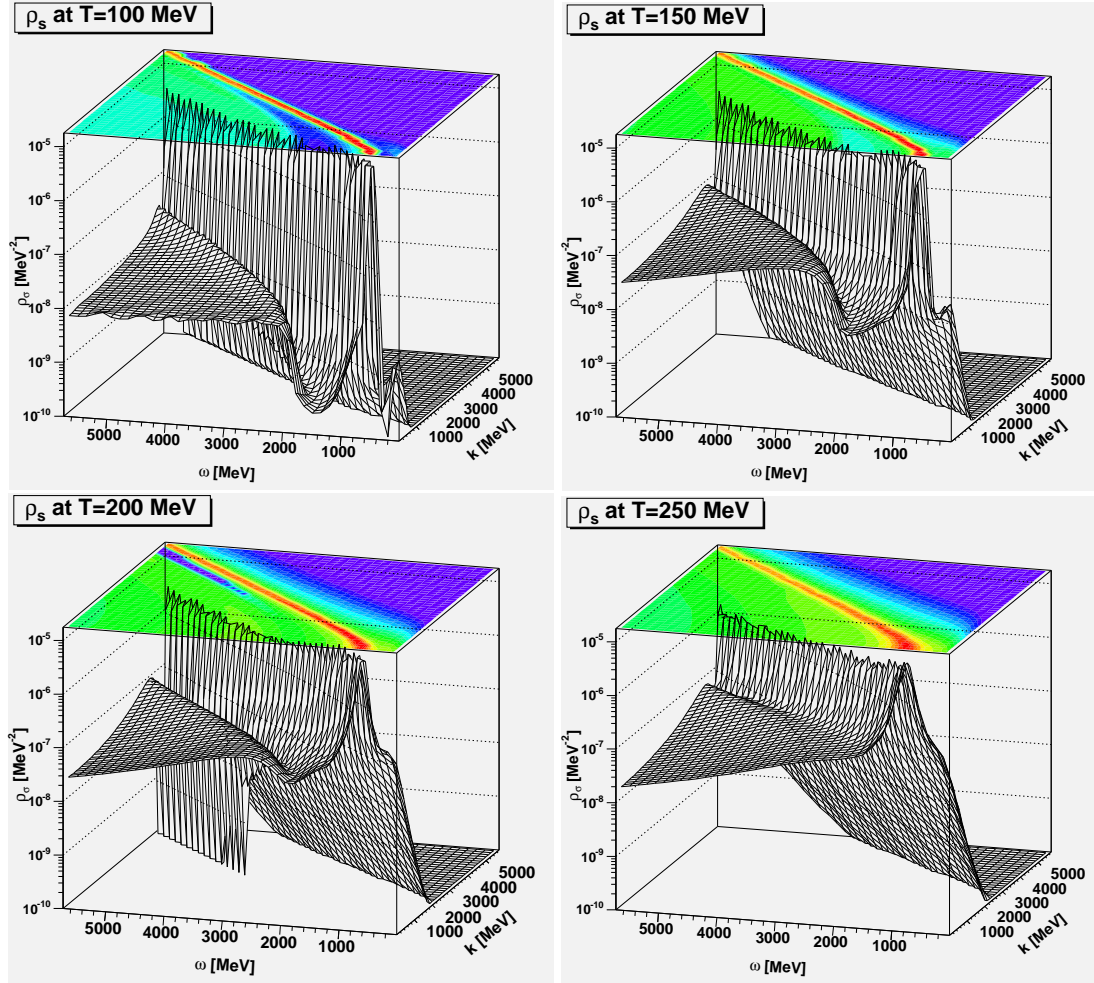


Figure 3.10: The spectral function of the  $\sigma$  meson at a temperature of  $T = 100$  MeV,  $T = 150$  MeV,  $T = 200$  MeV and  $T = 250$  MeV.

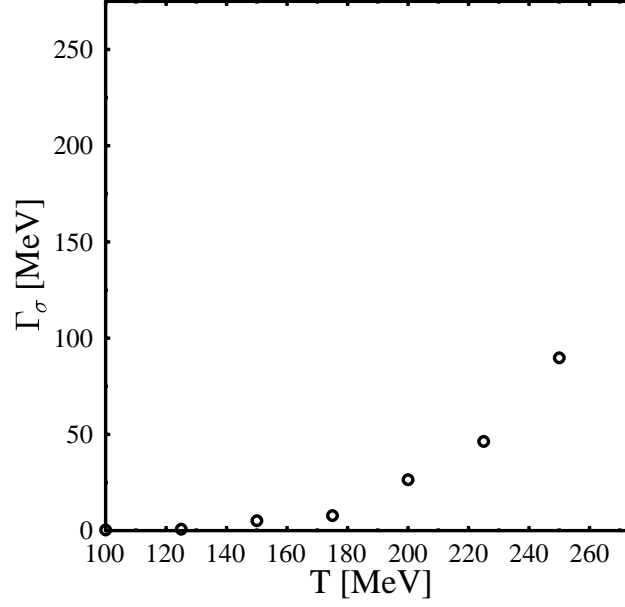


Figure 3.11: The decay width of the  $\sigma$  meson as a function of temperature at  $k = 165$  MeV. The width approximately increases exponentially with higher temperatures.

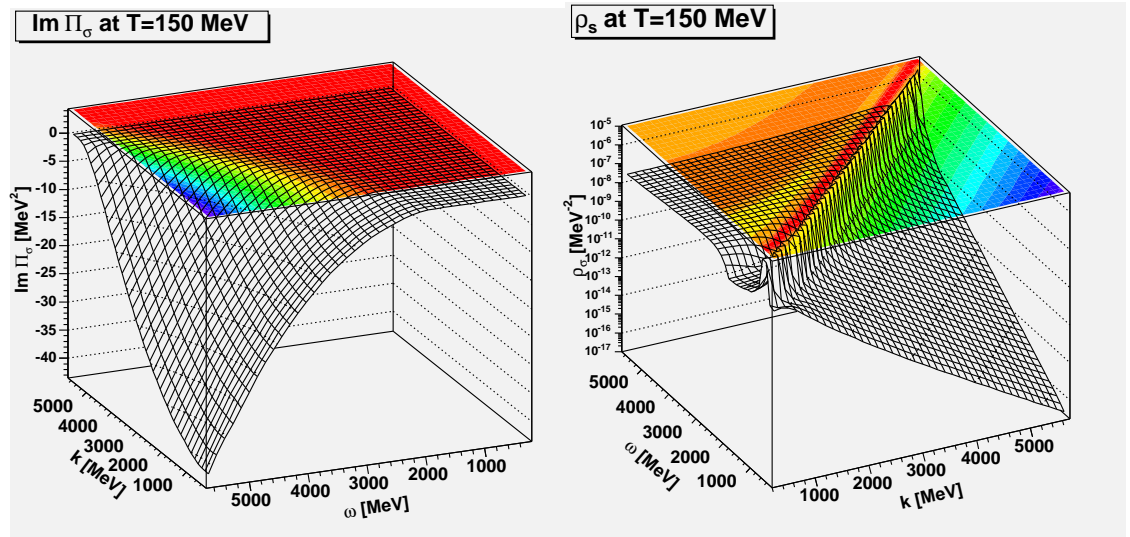


Figure 3.12: The imaginary part of the self-energy (left-hand side) and the complete spectral function (right-hand side) of the  $\sigma$  meson at  $T = 150$  MeV.



of a  $\sigma$  meson into two  $\sigma$  mesons. This decay is visible in the spectral function at temperatures below or equal 200 MeV. To illustrate this, figure 3.13 shows a cut through the  $\sigma$ -spectral function at a momentum of  $k = 165$  MeV and different temperatures. The two-sigma decay is visible at  $T = 150$  MeV and  $T = 200$  MeV as a little step at twice the effective  $\sigma$ -meson mass, which is  $M_\sigma = 546$  MeV at  $T = 150$  MeV and  $M_\sigma = 617$  MeV at  $T = 200$  MeV. At higher temperatures it becomes covered by the broadening mass-shell peak. The two-fermion decay is also visible very well at  $T = 150$  MeV, where the effective mass of the fermion is  $M_\psi = 935$  MeV, and at  $T = 200$  MeV with  $M_\psi = 903$  MeV. At higher temperatures this structure also merges with the mass-shell peak because of the decreasing fermion mass as well as the rising  $\sigma$ -meson mass. The shift of the mass-shell peak itself and its broadening with rising temperature are also nicely visible in this figure. Not shown in the figures is the fact that the  $\sigma$  spectral func-

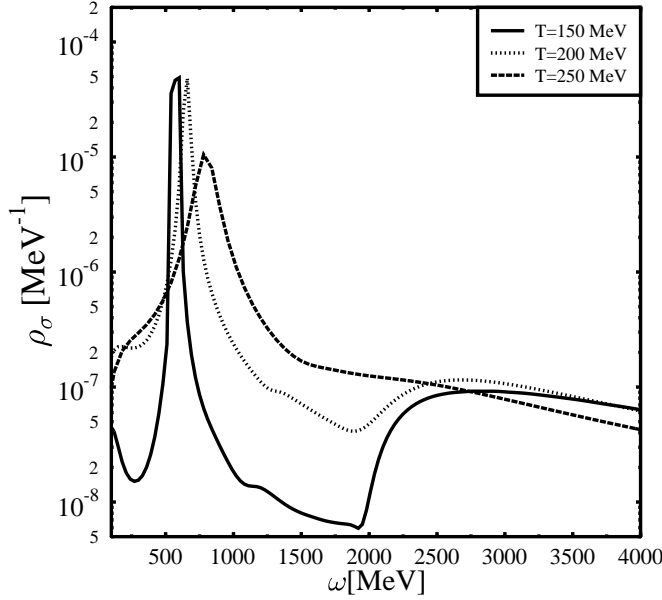


Figure 3.13: The spectral function of the  $\sigma$  meson at a momentum of  $k = 165$  MeV as a function of energy at  $T = 150$  MeV,  $T = 200$  MeV and  $T = 250$  MeV. Beside the mass-shell and the two-baryon decay one can see the two  $\sigma$ -meson decay of the sunset diagram at an energy of twice the effective  $\sigma$  mass.

tion is anti-symmetric in energy, as are all other bosonic spectral functions. This can be easily seen in (3.11) together with the definition of the spectral function (3.7).

### The $\omega$ meson

Figure 3.14 shows the transverse projection of the  $\omega$ -meson spectral function. The most prominent structure is again the mass-shell peak which gets broader



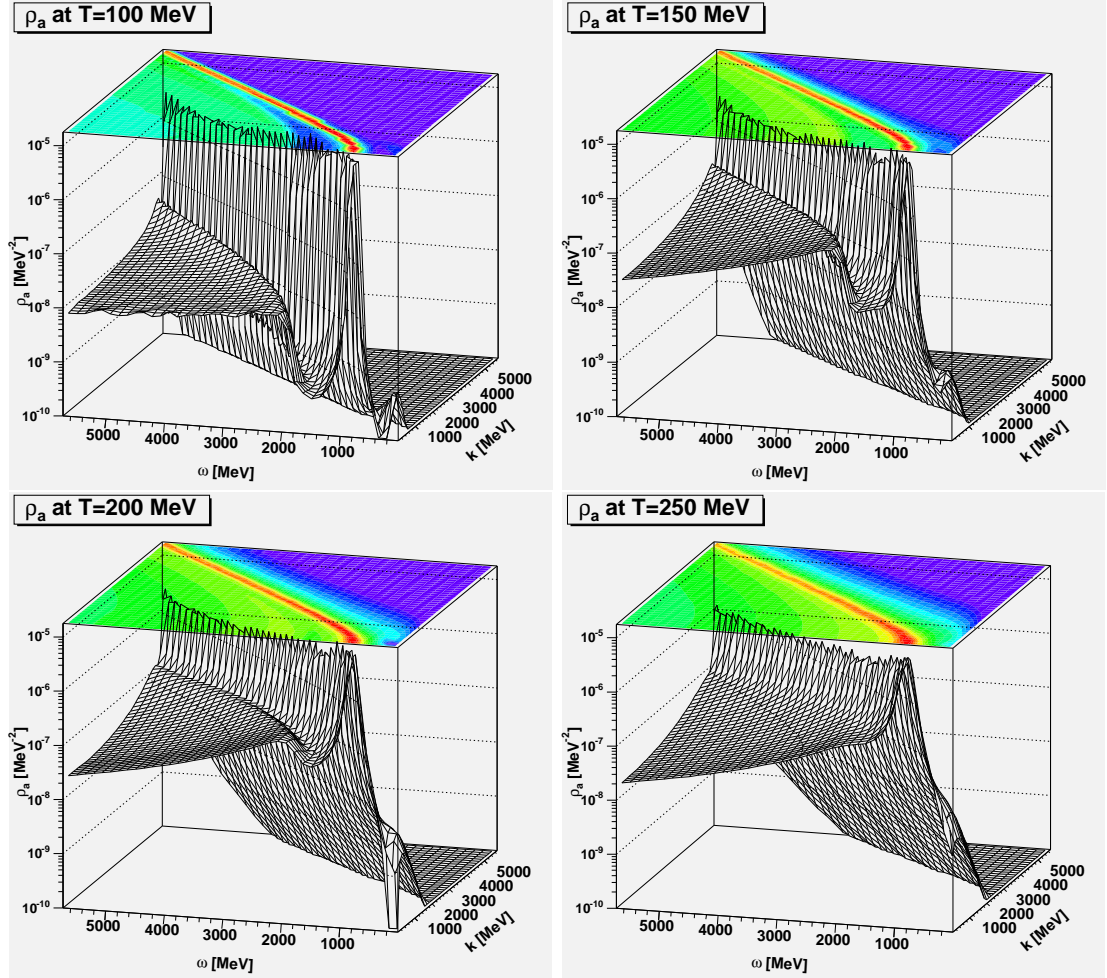


Figure 3.14: The transverse projection of the spectral function of the  $\omega$  meson at a temperature of  $T = 100$  MeV,  $T = 150$  MeV,  $T = 200$  MeV and  $T = 250$  MeV.

with higher temperatures while the maximum value decreases. Furthermore, the spectral function clearly shows the onset of the decay into two baryons at energies of twice their effective mass, a process which corresponds to the sunset diagram in the self-energy. At low temperature the mass-shell peak and the

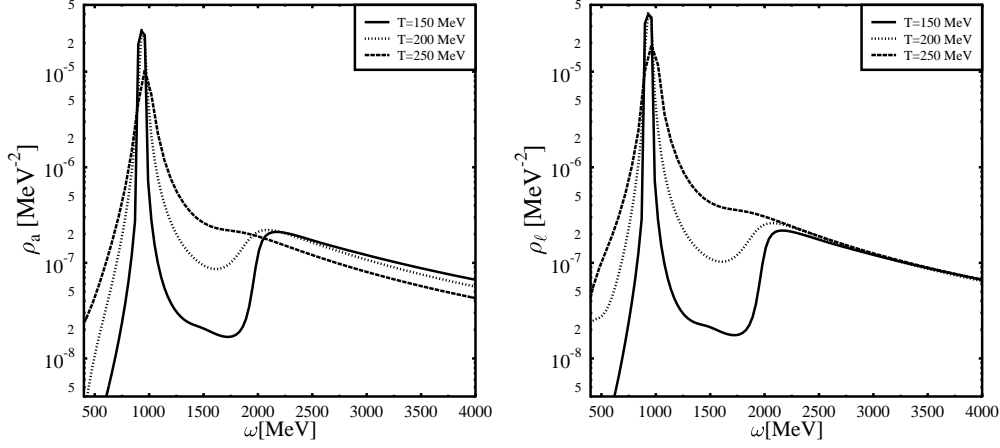


Figure 3.15: The transverse (left) and longitudinal (right) projection of the  $\omega$ -meson spectral function at a momentum of  $k = 495$  MeV as a function of energy at  $T = 150$  MeV,  $T = 200$  MeV and  $T = 250$  MeV. The fermion-anti-fermion decay is very pronounced at the lower two temperatures and merges with the mass-shell peak at  $T = 250$  MeV.

decay are well separated although the trough between them gets more shallow at higher momenta. With the peak becoming broader and the effective baryon mass decreasing at higher temperatures the two structures start to overlap until the trough vanishes. The situation is highlighted in figure 3.15 which shows a cut through the transverse and the longitudinal projection of the  $\omega$ -meson spectral function at a momentum of  $k = 495$  MeV and three different temperatures. Since the real parts of the  $\omega$ -meson self-energies are not taken into account, the mass of the  $\omega$  meson does not change. Thus the peak on the mass-shell does not change its location. The decay maximum flattens a little bit at higher momenta.

The decay width of the transverse as well as the longitudinal projection is shown in figure 3.16 as a function of temperature at a momentum of  $k = 765$  MeV. It increases approximately exponentially with rising temperature, but a little bit faster for the longitudinal projection. Figure 3.17 shows the longitudinal projection of the  $\omega$ -meson spectral function  $\rho_\ell$ . As in the other spectral functions two main structures are visible: a pronounced peak at the mass-shell and the decay into baryon and anti-baryon. Again the peak gets broader with higher temperatures while the onset of the decay moves to lower energies. As in the transverse spectral function the trough gets more shallow at higher momenta but here it vanishes completely, so that the mass-shell and the decay structure become indistinguishable. Figure 3.15 shows a cut through  $\rho_\ell$  at different temperatures

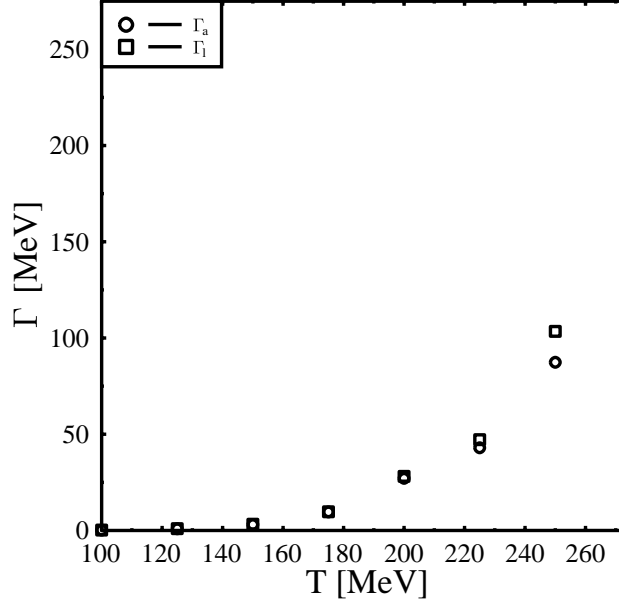


Figure 3.16: The decay width of the transverse and the longitudinal projection of the  $\omega$  meson at different temperatures and a momentum of  $k = 765$  MeV. Both widths approximately increase exponentially with temperature.

on the right-hand side. It very much resembles the transverse projection.

### 3.4.3 The fermionic spectral functions

The fermionic spectral function is decomposed into three parts with different Dirac structure. Figure 3.18 shows the part proportional to  $\gamma_0$ . Like the bosonic spectral functions, the fermionic  $\rho_0$  shows a sharp peak at the mass-shell. It becomes broader with higher temperatures as shown in figure 3.19. At the same time the height of the mass-shell peak is reduced by around 75 %.

Furthermore, a decay structure is visible. It occurs at energies between  $\omega = 1400$  MeV and  $\omega = 1500$  MeV which coincides very well with the emission of a  $\sigma$  meson, which at  $T = 150$  MeV has an effective mass of  $M_\sigma = 547$  MeV, by the fermion with an effective mass of  $M_\psi = 935$  MeV. The decay is very well separated at low temperatures. However, with the broadening of the mass-shell peak this starts to overlap with the decay.

On the other hand, the  $\omega$  meson with a mass of  $m_\omega = 782$  MeV also couples to the fermion. This decay occurs at  $\omega \simeq 1700$  MeV and forms a little step in the spectral function at  $T = 150$  MeV. At higher temperatures it is not visible. The situation is highlighted in figure 3.20 which is a cut through the spectral function at a momentum of  $k = 195$  MeV for different temperatures. This figure also shows the shift of the mass-shell peak and its broadening very well.

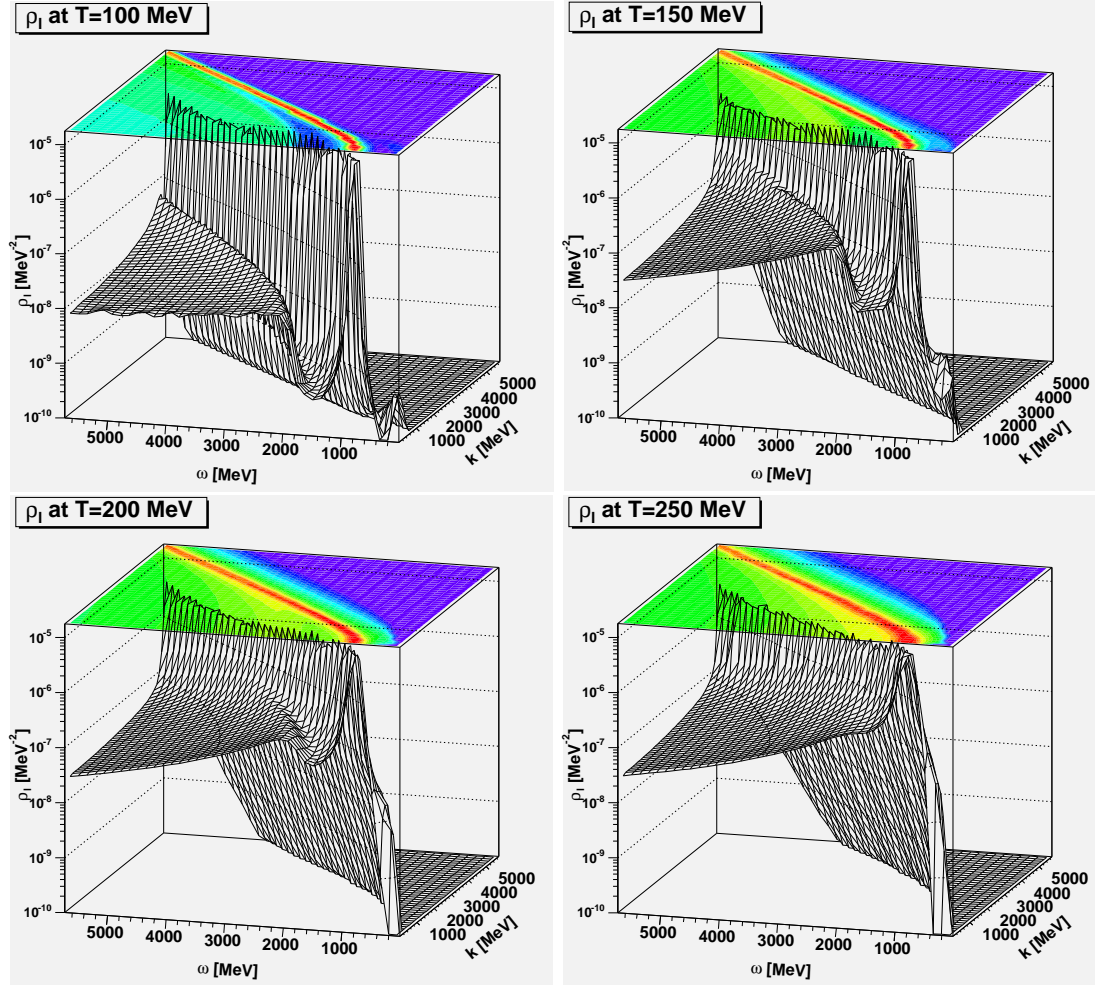


Figure 3.17: The longitudinal projection of the spectral function of the  $\omega$  meson at a temperature of  $T = 100$  MeV,  $T = 150$  MeV,  $T = 200$  MeV and  $T = 250$  MeV.

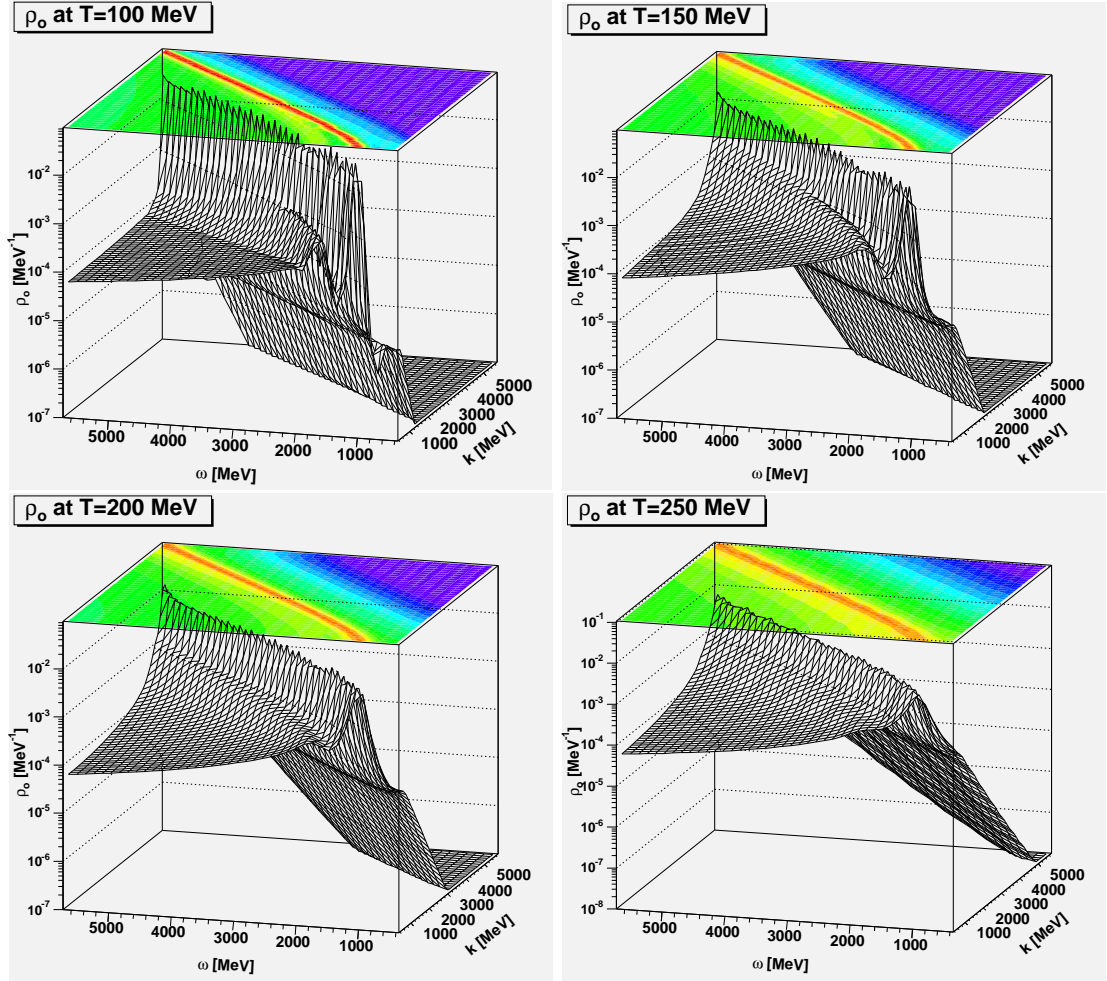


Figure 3.18: The part of the fermionic spectral density which is proportional to  $\gamma_0$  at a temperature of  $T = 100 \text{ MeV}$ ,  $T = 150 \text{ MeV}$ ,  $T = 200 \text{ MeV}$  and  $T = 250 \text{ MeV}$ .

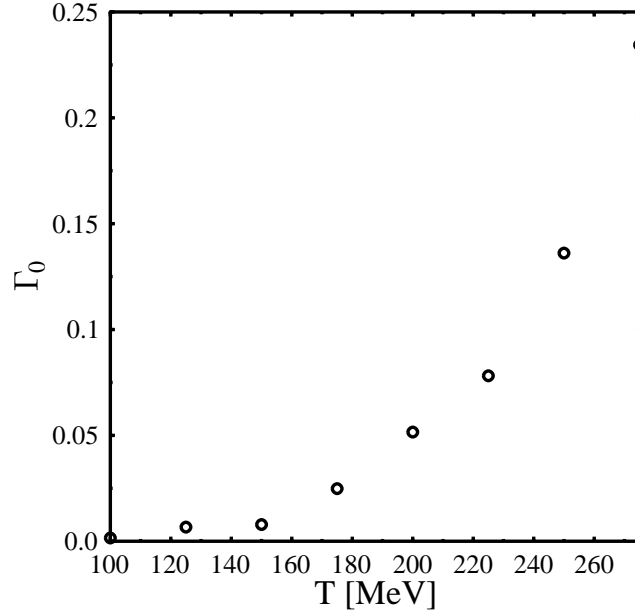


Figure 3.19: The width of the fermion spectral function  $\rho_0$  as a function of momentum at different temperatures and  $k = 765$  MeV.

It should be noted that the  $\gamma_0$  component of the fermion self-energy is symmetric in energy, in contrast to all other spectral functions calculated here which are anti-symmetric. This behavior can also be observed in the spectral function of the free fermion (3.38) where the spatial and the scalar component are anti-symmetric while the time component is multiplied by  $k_0$  and therefore symmetric.

Figure 3.21 shows the part of the fermion spectral function which is proportional to the unit matrix. Again a prominent peak is visible on the mass-shell which gets broader with higher temperatures. Furthermore a decay structure can be identified which overlaps with the mass-shell peak at higher momenta and higher temperatures. As for the  $\gamma_0$  component of the spectral function  $\rho_0$ , this decay can be associated with the decay of a fermion into a  $\sigma$  meson and a fermion since it occurs at around  $\omega = 1550$  MeV which is just the sum  $M_\sigma + M_\psi$ . Also the  $\omega$  decay is visible at  $T = 150$  MeV and  $T = 200$  MeV as a little bump at an energy which is the sum of the effective fermion mass at the respective temperature and the  $\omega$  mass of  $m_\omega = 782$  MeV (around  $\omega = 1700$  MeV). Figure 3.22 highlights this in a cut through the spectral function at a momentum of  $k = 195$  MeV. For  $\rho_m$  no sum rule exists to check whether some contribution falls between the lattice spacing or misses because the real part has been neglected. However, the time component  $\rho_0$  is corrected by at most 20 %, so that a similar uncertainty should be expected here.

Finally, figure 3.23 shows the part of the fermion spectral function which is



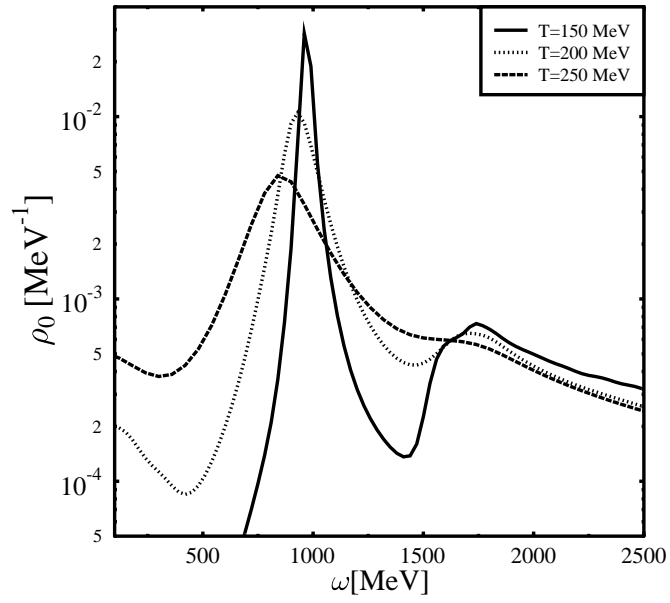


Figure 3.20: Cut through the spectral function  $\rho_0$  of the fermion at a momentum of  $k = 195$  MeV. The onset of the  $\sigma$  meson decay is clearly visible between  $\omega = 1400$  MeV and  $\omega = 1500$  MeV at the lower two temperatures. At higher temperatures this process only alters the slope a bit. The interaction with the  $\omega$  meson occurs at around  $\omega = 1700$  MeV as a little step at  $T = 150$  MeV.

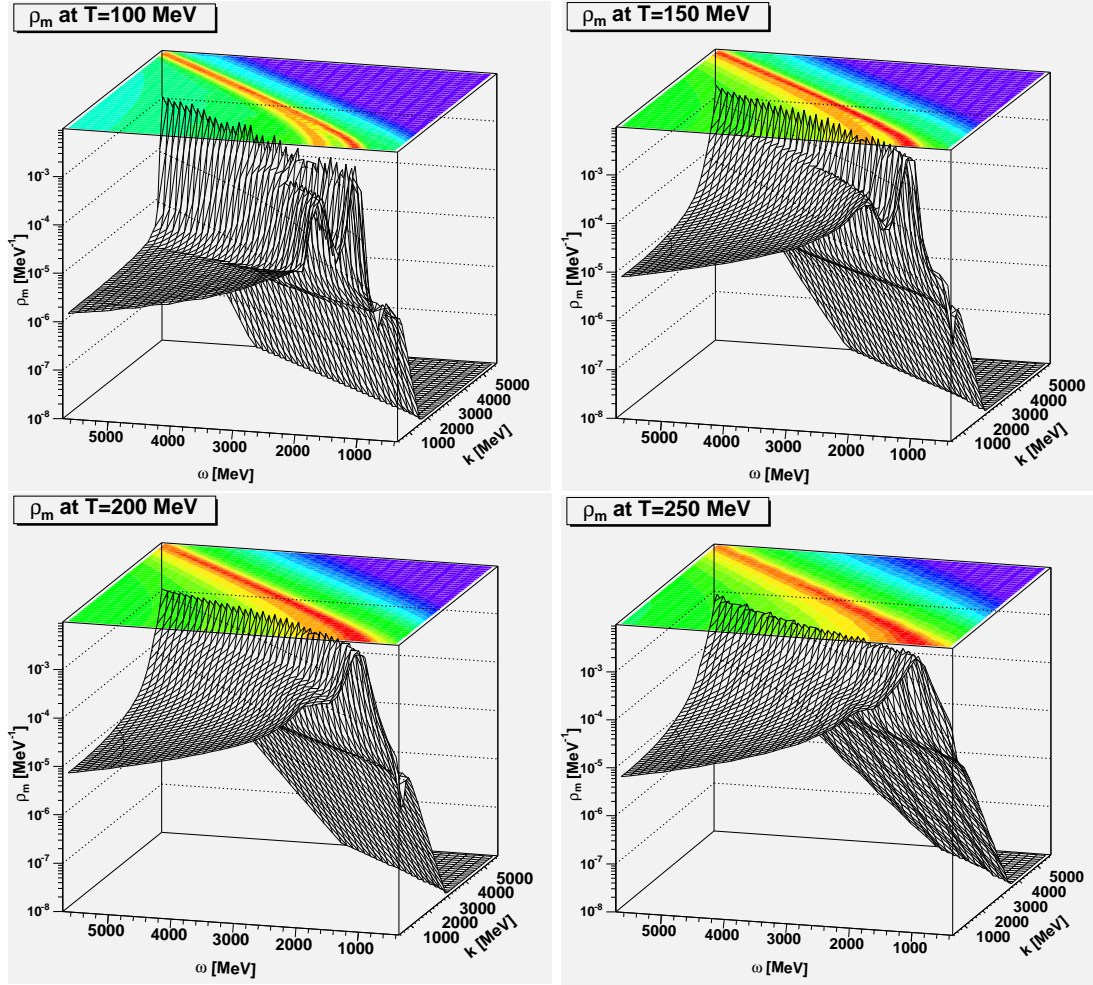


Figure 3.21: The part of the fermionic spectral density which is proportional to the unit matrix,  $\rho_m$ , at a temperature of  $T = 100$  MeV,  $T = 150$  MeV,  $T = 200$  MeV and  $T = 250$  MeV.



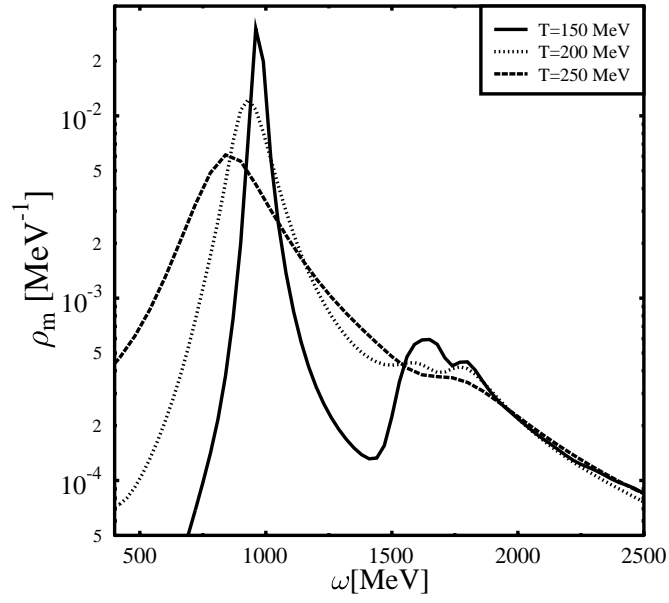


Figure 3.22: Cut through the fermion spectral function  $\rho_0$  at a momentum of  $k = 195$  MeV. The onset of the decay with the  $\sigma$  meson is clearly visible between  $\omega = 1400$  MeV and  $\omega = 1500$  MeV. Also the  $\omega$  decay at around  $\omega = 1700$  MeV is visible as a little step at the lower two temperatures.

proportional to  $\gamma_i$ . Again a pronounced peak on the mass-shell and a decay

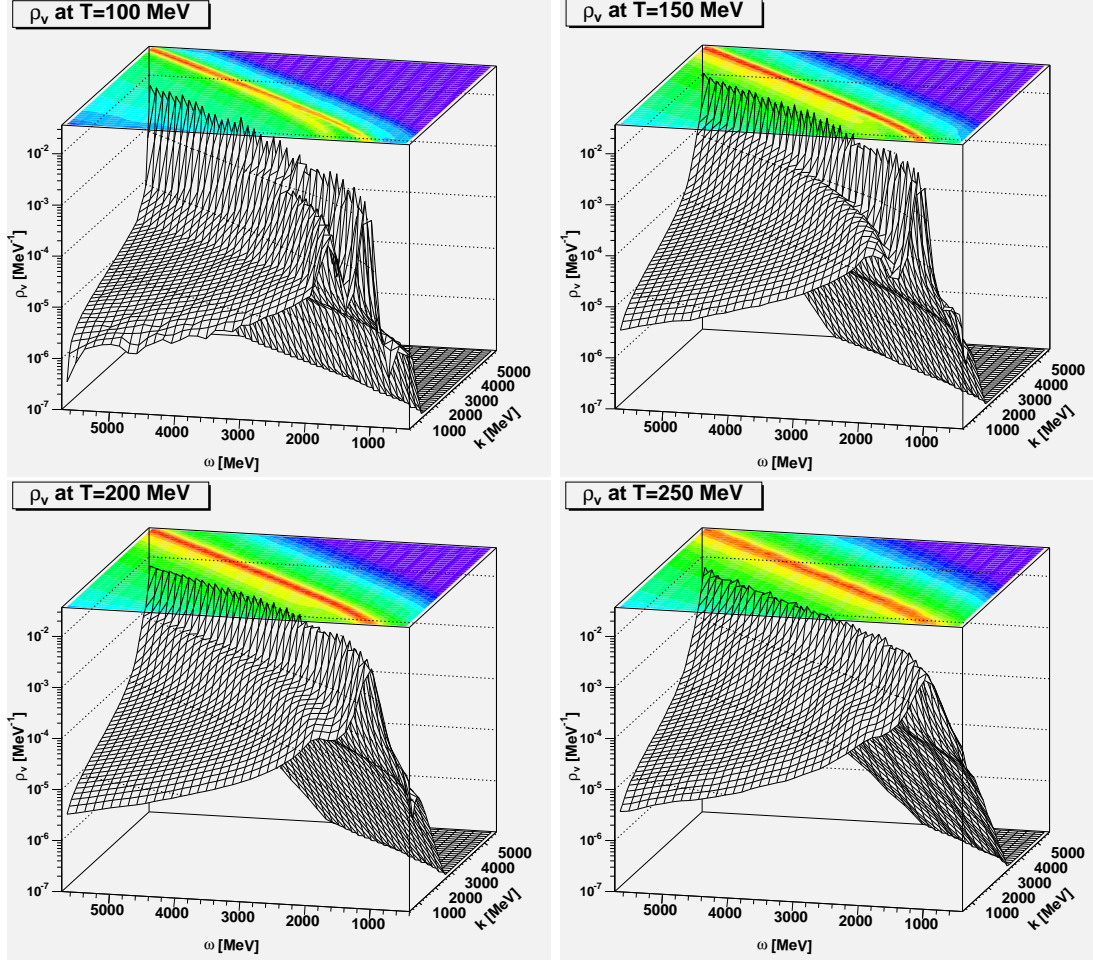


Figure 3.23: The part of the fermionic spectral density which is proportional to  $\gamma_i$  at a temperature of  $T = 100$  MeV,  $T = 150$  MeV,  $T = 200$  MeV and  $T = 250$  MeV.

structure are visible. The decay and the mass-shell peak merge at high momenta as well as high temperatures because the mass-shell peak broadens significantly. At the same time it reduces its height by about 70 %. The decay is highlighted in figure 3.24 which provides a cut through the spectral function at a momentum of  $k = 195$  MeV. The shape resembles the cut through  $\rho_m$ . The  $\sigma$ -meson decay and the  $\omega$ -meson decay are clearly visible as steps at energies which are the sums of the respective effective masses. Again there is no sum rule for  $\rho_v$ .

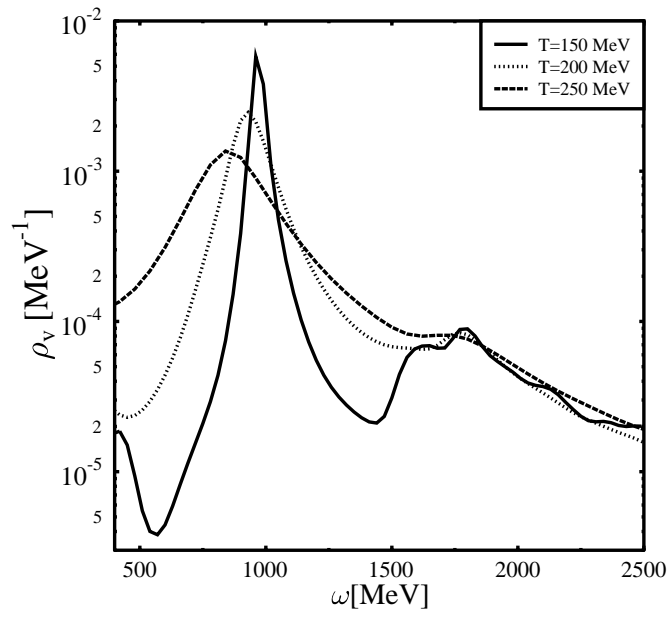


Figure 3.24: Cut through the fermion spectral function  $\rho_v$  at a momentum of  $k = 195$  MeV. The onset of the decay with the  $\sigma$  meson is clearly visible between  $\omega = 1400$  MeV and  $\omega = 1500$  MeV. The  $\omega$ -meson decay occurs at  $\omega = 1720$  MeV and moves to the right together with the fermion mass.



## –IV–

# CONCLUSIONS AND OUTLOOK

This work is dedicated to the investigation of nuclear matter at non-zero temperatures within an effective hadronic model based on the Walecka model. It includes fermions as well as a vector  $\omega$  meson and a scalar  $\sigma$  meson where for the latter a quartic self-interaction has been considered. The coupling constants have been adapted to the saturation properties of infinite nuclear matter.

A set of self-consistent Schwinger-Dyson equations has been set up for all included particles within the Cornwall-Jackiw-Tomboulis (CJT) formalism. This has been expanded to non-zero temperatures via the imaginary time formalism. Three different stages of approximations have been considered: The tree-level approximation including no two-particle irreducible loop diagrams at all, the Hartree approximation which takes into account the double-bubble diagram for the scalar meson, and finally an improved approximation where in addition two-particle irreducible sunset diagrams for all fields were included (compare figure 2.1). The tree-level and the Hartree approximation lead to quasi-particle solutions where all particles have fixed masses which are functions of temperature and chemical potential but not of the external momentum. In contrast, the improved approximation leads to particles which have a non-zero width in energy and therefore have to be expressed in terms of spectral functions. The parameters determined within the Hartree approximation have been used for all calculations, which made it possible to study the influence of the non-zero width directly.

The Schwinger-Dyson equations are solved by the fully dressed propagators. For the quasi-particles the self-energies of these propagators are real functions which account for a shift of the mass. In the improved approximation the solutions are complex functions in general. However, since the real parts of the sunset diagrams require thorough renormalization and a huge computational effort, only their imaginary parts have been considered in this work. Those define the widths of the spectral functions. The real parts of the self-energies are taken into account on Hartree level in all calculations.

On Hartree level the mean-field approximation has been applied, whereby only the time component of the vector mesons survives and the expectation value of

the fermion vanishes. The Schwinger-Dyson equations are then a set of coupled equations which can be solved straightforwardly.

In the improved approximation the vector mesons have to be projected with a suitable set of projection tensors and the fermions have to be decomposed into products of  $\gamma$  matrices to account for their Dirac structure. This procedure leads to a set of six coupled integral equations which are solved for the spectral functions on a discretized energy-momentum lattice in an iterative algorithm. The algorithm models the dressing of the propagator by inserting the self-energy on a certain level of approximation into the next iteration and thereby adding the loop dressing of the previous step. A meaningful approximation therefore leads to a converging iteration.

The Hartree-level calculations have been done at different temperatures as well as chemical potentials. It turned out that the difference compared to tree-level rises with temperature up to a maximum at around  $T = 200$  MeV at zero chemical potential. At higher chemical potentials the influence of the tadpole diagram is significantly reduced. The difference between the approximations is most pronounced for the mass of the  $\sigma$  meson where the Hartree value lies above the tree-level value by around 15 to 20 % (fig. 2.4) because here the tadpole diagram enters directly. The  $\sigma$ -mass rises with temperature which is a usual feature of the Walecka model in Hartree approximation.

The influence on the  $\sigma$ -field itself and the mass of the fermion emerged to be minor (fig. 2.6 and fig. 2.5). Also the thermodynamic properties pressure and entropy density remained virtually unchanged when the tadpole diagram was taken into account (fig. 2.7).

The improved approximation differs more obviously from the other calculations. Here, the effect of the non-zero widths leads to a strong deviation in all quantities under consideration. However, the investigation has been done for zero chemical potential, only.

The value of the  $\sigma$  field increases with temperature as in the other calculations but significantly more slowly and at higher temperatures (fig. 3.7). This behavior can be traced back to the scalar density which is clearly reduced compared to the Hartree approximation. The mass of the fermion is directly connected to the  $\sigma$  field and consequently shows the analogous behavior.

Also the mass of the  $\sigma$  meson changes (fig. 3.9). At low and intermediate temperatures it stays close to the Hartree result but rises much more slowly at higher temperatures. This behavior can be attributed to the tadpole term which behaves qualitatively different when calculated with non-zero widths. While it shows a saturation in the Hartree approximation it rises almost exponentially over the whole temperature range in the improved calculation.

Furthermore, the spectral functions of all involved particles have been studied. They all approximately broaden exponentially with increasing temperature. Besides a peak on the mass-shell, which all spectral functions have in common, one observes the different decay channels. In the bosonic spectral functions the

fermion-anti-fermion decay is most pronounced. For the  $\omega$  meson it is the only decay to occur. On the other hand, for the  $\sigma$  meson also a two-sigma decay is possible which indeed can be observed at low temperatures. At higher temperatures it becomes covered by the broadening mass-shell peak.

The fermion spectral functions show the decay into the  $\sigma$  meson and a fermion as well as into the  $\omega$  meson and a fermion. Although both structures are eventually visible the  $\sigma$  decay is much more pronounced than the  $\omega$  decay.

In all spectral functions the decay structures merge with the mass-shell peaks at very high temperatures of around  $T = 250$  MeV.

Within this work the techniques have been developed to apply the self-consistent CJT formalism to the investigation of hadronic matter which includes fermions together with vector and scalar mesons. All particles adopt non-zero widths which leads to a significant softening of the rise of the  $\sigma$ -field. It would be an interesting next step to investigate real phase transitions under the inclusion of non-zero widths to see if the order of the phase transition possibly changes. In particular the Walecka model shows a first-order phase transition from massive fermions to nearly massless ones if more fermionic degrees of freedom are taken into account [WTM<sup>+</sup>87]. Potentially, this becomes a cross-over when non-zero widths are considered.

But also the expansion to models which are closer to QCD is promising. Especially the investigation of the chiral phase transition within models based on chiral symmetry should be possible (section 1.7 lists some possible models). It is an interesting question if this phase transition changes its behavior when the particles acquire a non-zero width as it is suggested by the findings in this work. More physical models would also allow for physical predictions of particle productions in experiments.

A very straightforward expansion would be the inclusion of non-zero chemical potentials. However, it should be kept in mind that the current calculation already came close to the limit of computing power. The inclusion of more particles would certainly increase the computing time. Especially the widening of the spectral functions constitutes a limit. This is particularly important for calculations where the  $\sigma$  meson plays the role of the chiral partner of a light Goldstone boson. Here it is known that the  $\sigma$  meson acquires a huge decay width whereby a lattice of  $200 \times 200$  points might probably not be sufficient. Furthermore, the inclusion of the real parts of the sunset diagrams should be mentioned as a possible expansion of this work. It would hereby become possible to investigate the mass shift which is induced by the sunset diagrams. However, thorough renormalization has then to be performed.





# –APPENDIX A–

## CONVENTIONS

The following conventions have been used in this work:  
Four-vectors are denoted by upper case letters:

$$X = (t, \mathbf{x}) \tag{A.1}$$

are spatial vectors and

$$P = (\omega, \mathbf{p}) \tag{A.2}$$

are momentum vectors. The metric tensor is

$$g_{\mu\nu} = \begin{pmatrix} 1 & 0 & 0 & 0 \\ 0 & -1 & 0 & 0 \\ 0 & 0 & -1 & 0 \\ 0 & 0 & 0 & -1 \end{pmatrix} . \tag{A.3}$$

The integrals over space variables are, unless otherwise noted,

$$\int_X f(X) = \int_0^{1/T} d\tau \int d^3\mathbf{x} f(\tau, \mathbf{x}) \quad , \tag{A.4}$$

and integrals over momentum variables are

$$\int_K f(K) = T \sum_{n=-\infty}^{\infty} \int \frac{d^3\mathbf{k}}{(2\pi)^3} f(i\omega_n, \mathbf{k}) \quad , \tag{A.5}$$

where  $\omega_n$  are the Matsubara frequencies  $\omega_n = 2n\pi T$  for bosons and  $\omega_n = (2n + 1)\pi T$  for fermions.



## –APPENDIX B–

# DETERMINATION OF THE PARAMETERS

The Walecka model used in this work contains three parameters. These have been determined by adaption to the properties of nuclear matter at zero temperature in mean-field approximation.

All thermodynamic quantities can be derived from the grand canonical potential [FS90]

$$\Omega = -T \ln Z \quad (\text{B.1})$$

where  $Z = \text{Tr} \hat{\rho}$  is the grand canonical partition function and  $T$  the temperature. It is the trace over the statistical density matrix

$$\hat{\rho} = \exp \left[ -\frac{1}{T} (\hat{H} - \mu \hat{B}) \right] \quad , \quad (\text{B.2})$$

where  $\mu$  is the chemical potential. Here  $\hat{B}$  is the baryon number operator. The Hamilton operator  $\hat{H}$  can be deduced from the energy-momentum tensor

$$T_{\mu\nu} = \frac{\partial \mathcal{L}}{\partial (\partial^\nu \psi)} \partial_\mu \psi - g_{\mu\nu} \mathcal{L} \quad , \quad (\text{B.3})$$

as

$$\hat{H} = \int d^3x T^{00} \quad . \quad (\text{B.4})$$

In order to calculate  $T^{00}$  explicitly we insert the Fourier representation of the baryon field

$$\begin{aligned} \psi(\mathbf{x}, t) &= \sum_{s=\pm 1} \int \frac{d^3\mathbf{p}}{(2\pi)^{3/2}} \left[ b_{\mathbf{p},s} u(\mathbf{k}, s) e^{i(\mathbf{p}\mathbf{x} - \epsilon^+ t)} + d_{\mathbf{p},s}^\dagger v(\mathbf{p}, s) e^{-i(\mathbf{p}\mathbf{x} + \epsilon^- t)} \right] \\ \bar{\psi}(\mathbf{x}, t) &= \sum_{s=\pm 1} \int \frac{d^3\mathbf{p}}{(2\pi)^{3/2}} \left[ b_{\mathbf{p},s}^\dagger \bar{u}(\mathbf{k}, s) e^{-i(\mathbf{p}\mathbf{x} - \epsilon^+ t)} + d_{\mathbf{p},s} \bar{v}(\mathbf{p}, s) e^{i(\mathbf{p}\mathbf{x} + \epsilon^- t)} \right] \end{aligned} \quad (\text{B.5})$$

into the energy-momentum tensor and obtain

$$\begin{aligned}
T^{00} = & \sum_{s=\pm 1} \int \frac{d^3 \mathbf{p}}{(2\pi)^3} p_0 \left( b^\dagger b + d^\dagger d (+1) \right) - \frac{1}{2} \partial_\mu \sigma \partial^\mu \sigma + \frac{1}{2} m_\sigma^2 \sigma^2 \\
& + \lambda \sigma^4 - \frac{1}{2} m_\omega^2 \omega_\mu \omega^\mu + \frac{1}{4} (\partial_\mu \omega_\nu - \partial_\nu \omega_\mu) (\partial^\mu \omega^\nu - \partial^\nu \omega^\mu) \quad ,
\end{aligned} \tag{B.6}$$

where the divergent part in the first line represents the Dirac sea which is neglected here. The Hamilton operator is now given by (B.4). The partition function is obtained as the trace over the density matrix (B.2)

$$\begin{aligned}
Z = \text{Tr} \hat{\rho} = & \sum_{n_{\mathbf{k}}} \langle n_{\mathbf{k}} | \exp \left\{ -\frac{1}{T} \left[ \sum_{s,i} p_0 \left( b^\dagger b + d^\dagger d \right) - \mathcal{V} \left( \frac{1}{2} \partial_\mu \sigma \partial^\mu \sigma + \frac{1}{2} m_\sigma^2 \sigma^2 + \lambda \sigma^4 \right. \right. \right. \\
& \left. \left. - \frac{1}{2} m_\omega^2 \omega_\mu \omega^\mu + \frac{1}{4} (\partial_\mu \omega_\nu - \partial_\nu \omega_\mu) (\partial^\mu \omega^\nu - \partial^\nu \omega^\mu) \right) - \mu \hat{B} \right] \right\} | n_{\mathbf{k}} \rangle \\
= & \exp \left\{ \frac{1}{T} \mathcal{V} \left[ \frac{1}{2} \partial_\mu \sigma \partial^\mu \sigma + \frac{1}{2} m_\sigma^2 \sigma^2 + \lambda \sigma^4 \right. \right. \\
& \left. \left. - \frac{1}{2} m_\omega^2 \omega_\mu \omega^\mu + \frac{1}{4} (\partial_\mu \omega_\nu - \partial_\nu \omega_\mu) (\partial^\mu \omega^\nu - \partial^\nu \omega^\mu) \right] \right\} \\
\times & \prod_{s,i} \left( 1 + e^{-\frac{1}{T}(E - \mu_i^*)} \right) \left( 1 + e^{-\frac{1}{T}(E + \mu_i^*)} \right) \quad ,
\end{aligned} \tag{B.7}$$

where the sum over  $i$  counts the intrinsic quantum numbers. For the Walecka model the grand canonical potential is with (B.1)

$$\begin{aligned}
\frac{\Omega}{\mathcal{V}} = & -\frac{1}{2} \partial_\mu \sigma \partial^\mu \sigma + \frac{1}{2} m_\sigma^2 \sigma^2 + \lambda \sigma^4 - \frac{1}{2} m_\omega^2 \omega_\mu \omega^\mu + \frac{1}{4} (\partial_\mu \omega_\nu - \partial_\nu \omega_\mu) (\partial^\mu \omega^\nu - \partial^\nu \omega^\mu) \\
& - T \gamma \sum_{i,k} \left[ \ln(1 + e^{-\frac{1}{T}(E - \mu_i^*)}) + \ln(1 + e^{-\frac{1}{T}(E + \mu_i^*)}) \right] \quad .
\end{aligned} \tag{B.8}$$

Here  $\gamma$  is the spin-isospin degeneracy factor. In *mean-field approximation* at  $T = 0$  this becomes

$$\frac{\Omega}{\mathcal{V}} \Big|_{T=0} = \frac{1}{2} m_\sigma^2 \sigma^2 + \lambda \sigma^4 - \frac{1}{2} m_\omega^2 \omega_0^2 + \frac{\gamma}{(2\pi)^3} \sum_i \int d^3 \mathbf{k} (E(k) - \mu_i^*) \tag{B.9}$$

as long as  $E < \mu^*$ .

In the following the definitions  $S = g_\sigma \sigma$ ,  $C_S^2 = \frac{g_\sigma^2}{m_\sigma^2}$ ,  $C_V^2 = \frac{g_\omega^2}{m_\omega^2}$  and  $\lambda' = \frac{\lambda}{g_\sigma^4}$  are used.

## Binding energy

In general the binding energy is  $\mathcal{E} = \Omega/\mathcal{V} + T\mathcal{S} + \mu\rho_B$ , where

$$\mathcal{S} = \frac{\partial(\Omega/\mathcal{V})}{\partial T} \tag{B.10}$$

is the entropy density. At zero temperature one obtains in a straightforward calculation for the Walecka model:

$$\begin{aligned} \mathcal{E} = & \left( \frac{1}{2} \frac{S^2}{C_S^2} + \lambda' S^4 + \frac{1}{2} C_V^2 \rho_B^2 \right) \\ & + \frac{1}{2\pi^2} \gamma \left[ \frac{1}{4} k_F^3 E_F^* + \frac{1}{8} M_\psi^2 k_F E_F^* - \frac{1}{8} M_\psi^4 \ln \left( \frac{k_F + E_F^*}{M_\psi} \right) \right] \quad , \quad (\text{B.11}) \end{aligned}$$

which is connected to the binding energy per nucleon  $E_B$  by

$$E_B = \frac{\mathcal{E}}{\rho_B} - m_\Psi \quad . \quad (\text{B.12})$$

Here  $E^* = \sqrt{\vec{k}^2 + m_\Psi + S}$ ,  $M_\psi = m_\Psi + S$  and  $\mu^* = \mu - \rho_B C_V^2$ . The Fermi-momentum  $k_F$  can be determined via the Einstein theorem as (1.138)

$$k_F = \sqrt{\mu^{*2} - M_\psi^2} \quad . \quad (\text{B.13})$$

In this work I used a value of  $E_B = -16$  MeV for the saturation binding energy.

### Baryon density

The baryon density is at zero temperature (compare (1.137))

$$\rho_B = \gamma \frac{k_F^3}{6\pi^2} \quad , \quad (\text{B.14})$$

where  $\gamma = 4$  counts the fermionic spin-isospin degrees of freedom. Here a value of  $\rho_0 = 0.15891 \text{fm}^{-3}$  for nuclear matter at saturation has been used.

### Compressibility

The compressibility is in general [KMN<sup>+</sup>95]

$$K = 9\rho_0 \left. \frac{\partial \mu}{\partial \rho} \right|_{\rho=\rho_0} \quad , \quad (\text{B.15})$$

with  $\mu = \sqrt{k_F^2 + M_\psi^2} + C_V^2 \rho$  , where

$$M_\psi = m_\psi + g_\sigma \sigma = m_\psi - C_S^2 \rho_S + C_S^2 m_\psi^2 \lambda' \frac{(m_\psi - M_\psi)^3}{m_\psi^2} \quad (\text{B.16})$$

and  $\rho_S$  is the scalar density. Thus, for the Walecka model one obtains

$$K = 9\rho_0 \left( C_V^2 + \frac{2\pi^2}{\gamma k_F E_F^*} - C_S^2 \frac{M_\psi^2}{E_F^{*2}} g \right) \quad , \quad (\text{B.17})$$

where

$$g = \left(1 + \frac{\gamma}{4\pi^2} C_S^2 f + 12\lambda' C_S^2 S^2\right)^{-1}, \quad (\text{B.18})$$

with

$$f = k_F E_F^* + \frac{2k_F M_\psi^2}{E_F^*} - 3M_\psi^2 \ln\left(\frac{k_F + E_F^*}{M_\psi}\right). \quad (\text{B.19})$$

In this work I used a compressibility of  $K = 300$  MeV, however, this value is known with relatively low accuracy, only.

### Gap equations for the $\sigma$ field

The field equations can also be derived from the grand canonical potential. They provide the value of the field, which extremizes the potential:

$$\frac{\partial(\Omega/V)}{\partial\sigma} = 0. \quad (\text{B.20})$$

In the Walecka model at zero temperature one obtains in a straightforward calculation

$$m_\sigma^2 S + 4\lambda' C_S^2 m_\sigma^2 S^3 + C_S^2 m_\sigma^2 \rho_S = 0, \quad (\text{B.21})$$

where

$$\rho_S = \frac{\gamma}{4\pi^2} m^* \left[ k_F E_F^* - m^{*2} \ln\left(\frac{k_F + E_F^*}{m^*}\right) \right]. \quad (\text{B.22})$$

which is the  $T = 0$  limit of the result obtained in the CJT calculation.

### Gap-equations for the $\omega$ field

Similarly for the  $\omega$  field one obtains from

$$\frac{\partial(\Omega/V)}{\partial\omega_0} = 0. \quad (\text{B.23})$$

in a simple calculation

$$-m_\omega^2 \hat{\omega}_0 + g_\omega \rho_B = 0 \quad (\text{B.24})$$

which can be solved for  $\hat{\omega}_0$  immediately.

## –APPENDIX C–

# DEUTSCHE ZUSAMMENFASSUNG

Im Alter von  $10^{-5}$  Sekunden hatte das Universum eine Temperatur von ungefähr 170 MeV. Zu dieser Zeit fanden sich die Quarks, welche bis dahin mit den Gluonen in einem *Quark-Gluon-Plasma* vorgelegen hatten, zu Hadronen zusammen. Es entstanden Baryonen aus je drei Quarks und Mesonen aus je einem Quark und einem Antiquark. Je drei Antiquarks bildeten ein Antibaryon.

Wären im Urknall Quarks und Antiquarks in gleichen Mengen entstanden, hätten sich nach ungefähr  $10^{-4}$  Sekunden alle Teilchen mit ihren Antiteilchen gegenseitig vernichtet, so dass das Universum vollständig wieder zerstrahlt wäre. Dass dennoch Materie existiert ist ein Hinweis darauf, dass im Urknall mehr Teilchen als Antiteilchen erzeugt worden sein müssen, oder dass der anschließende Zerfall nicht für beide gleich abgelaufen ist.

Ein solcher Effekt muss allerdings sehr klein gewesen sein, denn bis heute konnte er in Experimenten nicht reproduziert werden.

Man darf also davon ausgehen, dass das frühe Universum einerseits sehr heiß war aber andererseits eine sehr geringe Netto-Baryonendichte hatte, weil die Zahl der Teilchen ungefähr genauso hoch war wie die Zahl der Antiteilchen. Ziel der vorliegenden Arbeit ist die Berechnung der Eigenschaften von Hadronen unter solchen Bedingungen.

Da die Abstände zwischen den Teilchen als groß angesehen werden können, bietet sich eine Untersuchung auf hadronischer Ebene an, in der die Quarkstruktur nicht berücksichtigt wird. In dieser Arbeit verwende ich als hadronisches Modell das *Walecka-Modell*, auch bekannt als *Quanten-Hadro-Dynamik I (QHD I)*, welches neben Baryonen ein skalares  $\sigma$ -Feld und ein vektorielles  $\omega$ -Feld enthält [Wal74]. Für das skalare Feld wird zusätzlich eine quartische Selbstwechselwirkung einbezogen.

Da die Teilchen sich bei hohen Temperaturen relativistisch verhalten und die Teilchenzahl nicht erhalten ist, erfolgt die Beschreibung quantenfeldtheoretisch. Um temperaturabhängige Prozesse untersuchen zu können, muss die Temperatur gesondert eingeführt werden. Dies geschieht auf elegante Weise in der *Pfadintegral-Quantisierung*. In der Pfadintegral-Quantisierung wird der

Propagator eines Feldes beschrieben als kohärente Summe aller Wege, die der Wert des Feldes an einem Raum-Zeit-Punkt zu einem anderen Wert an einem anderen Raum-Zeit-Punkt nehmen kann. Die zeitliche Entwicklung des Feldes wird durch die Übergangsamplitude beschrieben. Die Temperatur wird in den Pfadintegral-Formalismus nun eingeführt, indem man eine Analogie dieser Übergangsamplitude zur thermodynamischen Zustandfunktion ausnutzt. Man beobachtet nämlich, dass der Zeitentwicklungsoperator zur thermodynamischen Dichtematrix wird, wenn man die Zeit durch eine imaginäre Temperatur  $t = -i\frac{1}{T}$  ersetzt. Da man die Übergangsamplitude durch ein Pfadintegral beschrieben hat, kann man nun auch die Zustandfunktion auf diese Weise ausdrücken. Als Folge geht allerdings die Zeitabhängigkeit verloren, so dass nur statische Systeme im thermodynamischen Gleichgewicht mit diesem *Imaginärzeitformalismus* beschrieben werden können.

Berechnungen von Kernmaterieeigenschaften bei nicht verschwindenden Temperaturen sind weit verbreitet. Allerdings wurden sie bisher meist in der *Mean-Field-Näherung* [FS90, SW86, CW74, Wal95] oder in Ein-Schleifen-Näherung in der *Loop-Expansion* [FS91, HS81] durchgeführt. Störungsentwicklungen sind bei nicht verschwindenden Temperaturen im allgemeinen nicht konvergent, wie in Abschnitt 1.4 dargelegt.

Wie Furnstahl et al. gezeigt haben, ist im Walecka-Modell auch die Loop-Expansion, zumindest wenn bis zu zwei Schleifen berücksichtigt werden, nicht konvergent [FPS89].

In dieser Arbeit verwende ich den *Cornwall-Jackiw-Tomboulis*-Formalismus (CJT) für meine Berechnungen. Die Idee ist hier, einen Satz von selbst-konsistenten Schwinger-Dyson-Gleichungen aufzustellen, deren Lösungen die vollen Propagatoren der berücksichtigten Teilchen sind. Die Schwinger-Dyson-Gleichungen werden hierbei über ein effektives Potential ausgedrückt, welches für die Berechnungen in dieser Arbeit näherungsweise aufgestellt wird. Diagrammatisch gesprochen besteht die Näherung darin, dass nur Beiträge bis zu einer bestimmten Irreduzibilität berücksichtigt werden. In dieser Arbeit sind dies alle einteilchenirreduziblen und einige zweiteilchenirreduziblen Diagramme aber keine, die drei- oder mehrteilchenirreduzibel sind.

Der CJT-Formalismus wurde ursprünglich für verschwindende Temperatur entwickelt und wurde als solcher bereits auf Berechnungen von Kernmaterieeigenschaften angewandt. Zum Beispiel verwendeten Phat und Anh das Walecka-Modell als Rahmen für ihre Untersuchungen [PA97a, PA97b] von Kernmaterie. Aber auch bei nicht verschwindenden Temperaturen wurden Rechnungen im CJT-Formalismus durchgeführt. So untersuchten Ruppert et al. die Verbreiterung des  $\rho$ -Mesons in Abhängigkeit von der Temperatur [RR05]. Einige Autoren behandeln den chiralen Phasenübergang im Rahmen dieses Formalismus, einerseits für Quasiteilchen mit impulsunabhängiger Masse [Pet99, LRSB00, RRR03] aber andererseits auch unter Berücksichtigung von



Effekten durch eine nicht verschwindende Zerfallsbreite [RRR05].

Ziel der vorliegenden Arbeit ist die Untersuchung des Einflusses nicht verschwindender Zerfallsbreiten auf die Eigenschaften von Baryonen sowie skalaren und vektoriellen Mesonen.

Die Untersuchung erfolgt in zwei Schritten. Im ersten Schritt berücksichtige ich nur ein einziges zweiteilchenirreduzibles Diagramm, nämlich das Double-Bubble-Diagramm (Zwei-Blasen-Diagramm) für das  $\sigma$ -Meson, welches aus der quartischen Selbstwechselwirkung resultiert. Hier können die sich ergebenden Schwinger-Dyson-Gleichungen durch Quasiteilchen-Ansätze gelöst werden, das heißt, die Massen der Teilchen sind unabhängig vom Impuls und haben keine Zerfallsbreite. Diese Näherung bezeichne ich im Folgenden als *Hartree-Näherung*. Im zweiten Schritt beziehe ich zusätzlich die zweiteilchenirreduziblen Sunset-Diagramme (Sonnenuntergangsdigramme) mit ein. Dabei spielen drei Diagramme eine Rolle. Zum einen ergibt sich aus der Selbstwechselwirkung des  $\sigma$ -Mesons die Möglichkeit eines Sunset-Diagramms mit drei  $\sigma$ -Propagatoren. Zum anderen können die Baryonen mit beiden Mesonen wechselwirken, wodurch sich zwei weitere Sunset-Diagramme ergeben. Diese Näherung wird im Folgenden als *verbesserte Näherung* bezeichnet. Alle in dieser Arbeit verwendeten Diagramme sind in Abbildung 2.1 dargestellt.

Für den Fall, dass Sunset-Diagramme berücksichtigt werden, lassen die Schwinger-Dyson-Gleichungen keine Quasiteilchen-Lösung mehr zu, so dass Spektraldichten eingeführt werden müssen. Ich berücksichtige hier die Realteile der Selbstenergien weiterhin in Hartree-Näherung und behalte auch die Parameter bei. Hinzu kommen jetzt allerdings Imaginärteile der Selbstenergien, welche zu nicht verschwindenden Zerfallsbreiten führen. Daher lässt der Vergleich dieser verbesserten Näherung zur Hartree-Näherung die direkte Untersuchung des Einflusses der nicht verschwindenden Zerfallsbreiten auf die Eigenschaften der berücksichtigten Felder zu.

Die verbesserte Näherung bringt einige Komplikationen verglichen mit der Hartree-Näherung mit sich. Einerseits, weil nun auch das vektorielle  $\omega$ -Meson eine Selbstenergie bekommt, die eine Lorentz-Struktur hat und daher tensoriell zerlegt werden muss. Andererseits aber auch, weil die Lösungen der Schwinger-Dyson-Gleichungen jetzt keine einfachen Zahlen (nämlich die Massen der Teilchen) sind, sondern Funktionen von Energie und Impuls, die Spektralfunktionen. Darüber hinaus müssen die Baryonen hinsichtlich ihrer Dirac-Struktur zerlegt werden.

Die Lösung der Schwinger-Dyson-Gleichungen nach den Spektralfunktionen wird numerisch auf einem diskretisierten Energie-Impuls-Gitter bewerkstelligt. Der Lösungsalgorithmus ist eine Iteration, bei welcher die in einem Iterationsschritt berechneten Spektralfunktionen im nächsten Schritt zu Berechnung der neuen Spektraldichten eingesetzt werden. Das Ergebnis dieses Vorgehens sind die vollen Propagatoren. Die Konvergenz des Verfahrens zeigt an, dass die gewählte Näherung physikalisch sinnvoll ist, weil Konvergenz bedeutet, dass die

Berücksichtigung höherer Schleifen-Beiträge zum Propagator diesen ab einem bestimmten Niveau nicht mehr verändern, wie in Abschnitt 3.3 dargestellt.

Wenden wir uns nun zunächst dem Einfluss des Double-Bubble-Diagramms des  $\sigma$ -Mesons auf die Eigenschaften der Teilchen zu. Die Näherung ohne das Double-Bubble-Diagramm wird im allgemeinen als Tree-Level-Näherung (Baumgraphennäherung) bezeichnet.

Der Einfluss des Double-Bubble-Diagramms ist am deutlichsten in der Masse des  $\sigma$ -Mesons bei verschwindendem chemischen Potential zu erkennen (Abb. 2.4). In Hartree-Näherung ist sie um bis zu 15 bis 20 % größer als in Tree-Level-Näherung, wobei der Unterschied bei Temperaturen um  $T = 200$  MeV am stärksten ausgeprägt ist. Bei nicht verschwindenden chemischen Potentialen fällt der Einfluss des Double-Bubble-Diagramms deutlich geringer aus. Dieses Ergebnis wird schon dadurch angedeutet, dass der einzige zusätzliche Term, der in Hartree-Näherung gegenüber der Tree-level-Näherung hinzukommt, in der Gleichung für die Masse des  $\sigma$ -Mesons steht (Abb. 2.4). Alle anderen Größen werden nur mittelbar beeinflusst, weil sie von dieser Masse abhängen. Entsprechend ist der Einfluss des zusätzlichen Terms hier deutlich schwächer ausgeprägt. Da der zusätzliche Term nicht vom chemischen Potential abhängt, reduziert sich sein relativer Anteil mit steigendem chemischen Potential. Auf die thermodynamischen Größen Druck und Entropiedichte hat das Double-Bubble-Diagramm so gut wie keinen Einfluss (Abb. 2.7). Der Unterschied zwischen den beiden Näherungen beträgt maximal 2 % (Abb. 2.8).

Das qualitative Verhalten bleibt in Hartree-Näherung gegenüber Tree-Level-Näherung für alle betrachteten Größen das gleiche. Die Masse des  $\sigma$ -Mesons steigt mit steigender Temperatur und steigendem chemischen Potential während die Baryonenmasse (Abb. 2.5) als Folge des steigenden  $\sigma$ -Feldes (Abb. 2.6) abfällt.

Die verbesserte Näherung hingegen zeigt sehr viel deutlichere Unterschiede zur Tree-Level-Näherung. Generell lässt sich sagen, dass alle Anstiege und Abfälle wesentlich langsamer mit steigender Temperatur geschehen als in den beiden anderen Näherungen. Der Crossover zwischen der Phase schwerer Baryonen und jener leichter Baryonen wird also stark aufgeweicht (Abb. 3.7). Eine ähnliche Aufweichung beobachtet man bei der Masse des  $\sigma$ -Mesons (Abb. 3.9). Diese wurde auch in der Hartree-Näherung schon angedeutet.

Der Unterschied zwischen den Näherungen nimmt mit steigender Temperatur zu. Interessant ist in diesem Zusammenhang die Betrachtung der Zerfallsbreiten, welche jetzt, durch Einführen einer Spektralfunktion, explizit berücksichtigt werden. Für alle Teilchen ergibt sich eine ungefähr exponentielle Verbreiterung mit zunehmender Temperatur (Abb. 3.11, 3.16 und 3.19). Nimmt man an, dass die Unterschiede zur Hartree-Näherung durch die nicht verschwindenden Zerfallsbreiten bedingt sind, passt es gut ins Bild, dass sie mit höheren Temperaturen stärker ausgeprägt sind.

Ein weiteres zentrales Resultat dieser Arbeit sind die Spektralfunktionen der

berücksichtigten Teilchen (Abb. 3.10, 3.14, 3.17, 3.18, 3.21 und 3.23). Die Spektralfunktionen können als Stärke eines Propagators bei einer bestimmten Energie und einem bestimmten Impuls interpretiert werden.

Allen betrachteten Spektralfunktionen ist ein scharfes Maximum auf der Massenschale gemein. Bei verschwindendem Impuls liegt es genau bei einer Energie, die der effektiven Masse des Teilchens entspricht und folgt bei höheren Impulsen der relativistischen Energie-Impuls-Beziehung.

Auch die Zerfälle, welche durch die berücksichtigten Diagramme ermöglicht werden, sind in den Spektralfunktionen zu erkennen. Für das  $\sigma$ -Meson beobachtet man eine sehr ausgeprägte Zerfallsstruktur in ein Fermion-Antifermion-Paar so wie, deutlich schwächer und teilweise durch die Spitze auf der Massenschale verdeckt, den Zerfall in zwei  $\sigma$ -Mesonen, der durch die Selbstwechselwirkung des  $\sigma$ -Mesons ermöglicht wird (Abb. 3.13).

In den Spektralfunktionen des  $\omega$ -Mesons ist der Fermion-Antifermion-Zerfall ebenfalls zu erkennen (Abb. 3.15). Weitere Prozesse gehen hier allerdings nicht ein.

Für die Fermionen ergeben sich Zerfälle sowohl in ein  $\sigma$ -Meson als auch in ein  $\omega$ -Meson. Die  $\sigma$ -Zerfälle sind sehr ausgeprägt, während die  $\omega$ -Zerfälle nur schwach zu erkennen sind (Abb. 3.20).

In allen Spektralfunktionen beobachtet man, wie schon oben erwähnt, mit steigender Temperatur eine signifikante Verbreiterung des Maximums auf der Massenschale. Dadurch überlagert es die Zerfallsstrukturen. Die Verbreiterung des Maximums begrenzt auch die maximale Temperatur, die numerisch zugänglich ist. Bei Temperaturen jenseits von  $T = 250$  MeV wird die Spektralfunktion zu breit um sich durch ein Gitter von 200 mal 200 Stützstellen überdecken zu lassen. Mehr Stützstellen würden aber die Rechenzeit zu sehr vergrößern. Auch der Gitterabstand lässt sich nicht beliebig verbreitern, weil sonst das scharfe Maximum auf der Massenschale nicht mehr aufgelöst werden kann.

Eine Fortführung dieser Arbeit ist in verschiedene Richtungen interessant. Nahelegend ist zum Beispiel die Berücksichtigung eines nicht verschwindenden chemischen Potentials. Allerdings werden diese Rechnungen sehr rechenaufwändig sein, einerseits, weil die zu erwartende Verbreiterung der Spektralfunktionen ein größeres Gitter erforderlich macht und andererseits, weil die Parameter neu angepasst werden müssen, wofür die Berechnung der geschlossenen Diagramme nötig ist. Möglicherweise könnten verbesserte Integrationsroutinen dieses Problem lösen.

Im untersuchten Modell führte die Einbeziehung nicht verschwindender Zerfallsbreiten zu einer Abschwächung der Änderungen der Teilcheneigenschaften mit der Temperatur. Ein interessanter nächster Schritt wäre die Untersuchung echter Phasenübergänge unter Berücksichtigung nicht verschwindender Zerfallsbreiten. Zum Beispiel zeigt das Walecka-Modell einen Phasenübergang erster Ordnung von einer Phase massiver Fermionen in eine Phase nahezu masseloser Fermionen,

wenn mehr fermionische Freiheitsgrade berücksichtigt werden [WTM<sup>+</sup>87]. Es wäre interessant zu sehen, ob dieser Phasenübergang mit nicht verschwindenden Zerfallsbreiten zu einem Crossover würde.

Eine andere vielversprechende Erweiterung dieser Arbeit wäre die Anwendung der hier entwickelten Techniken auf chirale Modelle und insbesondere die Untersuchung des chiralen Phasenübergangs. Auch dessen Verhalten wird möglicherweise von nicht verschwindenden Zerfallsbreiten beeinflusst.

# BIBLIOGRAPHY

- [ACP93] G. Amelino-Camelia and S.-Y. Pi. Selfconsistent improvement of the finite temperature effective potential. *Phys. Rev.*, D47:2356–2362, 1993.
- [ACPS83] M. R. Anastasio, L. S. Celenza, W. S. Pong, and C. M. Shakin. Relativistic nuclear structure physics. *Phys. Rept.*, 100:327–401, 1983.
- [BB77] J. Boguta and A. R. Bodmer. Relativistic calculation of nuclear matter and the nuclear surface. *Nucl. Phys.*, A292:413–428, 1977.
- [BD98] J. D. Bjorken and S. D. Drell. *Relativistic Quantum Mechanics*. McGraw-Hill, New York, 1998.
- [Ber04] J. Berges. n-PI effective action techniques for gauge theories. *Phys. Rev.*, D70:105010, 2004.
- [BG77] G. Baym and G. Grinstein. Phase transition in the sigma model at finite temperature. *Phys. Rev.*, D15:2897–2912, 1977.
- [BGSG99] S. A. Bass, M. Gyulassy, H. Stöcker, and W. Greiner. Signatures of quark-gluon-plasma formation in high energy heavy-ion collisions: A critical review. *J. Phys.*, G25:R1–R57, 1999.
- [BK89] J. Boguta and J. Kunz. Chiral nuclear interactions. *Nucl. Phys.*, A501:637–652, 1989.
- [BLM54] K. Brückner, C. Levinson, and H. Mahmoud. Two-body forces and nuclear saturation. I. central forces. *Phys. Rev.*, 95:217, 1954.
- [BM96] R. Brockmann and R. Machleidt. The Dirac-Brueckner approach. *nucl-th/9612004*, 1996.
- [BM03] J. Baacke and S. Michalski. The o(n) linear sigma model at finite temperature beyond the hartree approximation. *Phys. Rev.*, D67:085006, 2003.
- [Bog83a] J. Boguta. Abnormal nuclei. *Phys. Lett.*, B128:19–23, 1983.

- 
- [Bog83b] J. Boguta. A saturating chiral field theory of nuclear matter. *Phys. Lett.*, B120:34–38, 1983.
- [BP90a] E. Braaten and R. D. Pisarski. Resummation and gauge invariance of the gluon damping rate in hot QCD. *Phys. Rev. Lett.*, 64:1338, 1990.
- [BP90b] E. Braaten and R. D. Pisarski. Soft amplitudes in hot gauge theories: A general analysis. *Nucl. Phys.*, B337:569, 1990.
- [BPZ<sup>+</sup>02] C. Beckmann, P. Papazoglou, D. Zschesche, S. Schramm, H. Stöcker, and W. Greiner. Nuclei, superheavy nuclei and hypermatter in a chiral SU(3)-model. *Phys. Rev.*, C65:024301, 2002.
- [BRS95] V. I. Borodulin, R. N. Rogalev, and S. R. Slabospitsky. CORE: COmpendium of RElations: Version 2.1. *hep-ph/9507456*, 1995.
- [BS03] J. Berges and J. Serreau. Progress in nonequilibrium quantum field theory. *hep-ph/0302210*, 2003.
- [Car04] M. E. Carrington. The 4PI effective action for  $\phi^4$  theory. *Eur. Phys. J.*, C35:383–392, 2004.
- [CH98] S. Chiku and T. Hatsuda. Optimized perturbation theory at finite temperature. *Phys. Rev.*, D58:076001, 1998.
- [CJT74] John M. Cornwall, R. Jackiw, and E. Tomboulis. Effective action for composite operators. *Phys. Rev.*, D10:2428–2445, 1974.
- [CW73] S. R. Coleman and E. Weinberg. Radiative corrections as the origin of spontaneous symmetry breaking. *Phys. Rev.*, D7:1888–1910, 1973.
- [CW74] S. A. Chin and J. D. Walecka. An equation of state for nuclear and higher-density matter based on a relativistic mean-field theory. *Phys. Lett.*, B52:24, 1974.
- [DJ74] L. Dolan and R. Jackiw. Symmetry behavior at finite temperature. *Phys. Rev.*, D9:3320–3341, 1974.
- [Due56] H.-P. Duerr. Relativistic effects in nuclear forces. *Phys. Rev.*, 103:469, 1956.
- [FLM02] F. Frömel, S. Leupold, and U. Mosel. Spectral functions of quarks in quark matter. *nucl-th/0209033*, 2002.
- [FLM03a] F. Frömel, H. Lenske, and U. Mosel. Short-range correlations in nuclear matter at finite temperatures and high densities. *Nucl. Phys.*, A723:544–556, 2003.

- 
- [FLM03b] F. Frömel, S. Leupold, and U. Mosel. Spectral function of quarks in quark matter. *Phys. Rev.*, C67:015206, 2003.
- [FPS89] R. J. Furnstahl, R. J. Perry, and B. D. Serot. Two loop corrections for nuclear matter in the Walecka model. *Phys. Rev.*, C40:321–353, 1989.
- [Frö01] F. Frömel. *Diploma Thesis*. 2001. <http://theorie.physik.uni-giessen.de/documents/diplom/froemel.pdf>.
- [FS90] R. J. Furnstahl and B. D. Serot. Covariant mean-field calculations of finite-temperature nuclear matter. *Phys. Rev.*, C41:262–279, 1990.
- [FS91] R. J. Furnstahl and B. D. Serot. Covariant Feynman rules at finite temperature: Application to nuclear matter. *Phys. Rev.*, C43:105–129, 1991.
- [FS93] R. J. Furnstahl and B. D. Serot. Finite nuclei in relativistic models with a light chiral scalar meson. *Phys. Rev.*, C47:2338–2343, 1993.
- [FS00] R. J. Furnstahl and B. D. Serot. Quantum hadrodynamics: Evolution and revolution. *Comments Nucl. Part. Phys.*, 2:A23–A45, 2000.
- [GM62] M. Gell-Mann. Symmetries of baryons and mesons. *Phys. Rev.*, 125:1067–1084, 1962.
- [GM64] M. Gell-Mann. The symmetry group of vector and axial vector currents. *Physics*, 1:63–75, 1964.
- [GML60] M. Gell-Mann and M Levy. The axial vector current in beta decay. *Nuovo Cim.*, 16:705, 1960.
- [Gol57] J. Goldstone. Derivation of Brueckner many-body theory. *Proc. R. Soc.*, A239:267, 1957.
- [GR96] W. Greiner and J. Reinhardt. *Field Quantization*. Springer-Verlag, Berlin, Heidelberg, 1996.
- [Gre05] W. Greiner. *Quantum Mechanics: Symmetries*. Springer-Verlag, Berlin, Heidelberg, 2005.
- [GRT90] Y. K. Gambhir, P. Ring, and A. Thimet. Relativistic mean field theory for finite nuclei. *Annals Phys.*, 198:132–179, 1990.
- [GW73a] D. J. Gross and F. Wilczek. Asymptotically free gauge theories. 1. *Phys. Rev.*, D8:3633–3652, 1973.

- 
- [GW73b] D. J. Gross and F. Wilczek. Ultraviolet behavior of non-abelian gauge theories. *Phys. Rev. Lett.*, 30:1343–1346, 1973.
- [HM84] F. Halzen and A. D. Martin. *Quarks & Leptons*. John Wiley & Sons, New York, 1984.
- [HS81] C. J. Horowitz and B. D. Serot. Selfconsistent hartree description of finite nuclei in a relativistic quantum field theory. *Nucl. Phys.*, A368:503, 1981.
- [Jac74] R. Jackiw. Functional evaluation of the effective potential. *Phys. Rev.*, D9:1686, 1974.
- [JRK83] A. D. Jackson, M. Rho, and E. Krotscheck. The sigma model and the binding energy of nuclear matter. *Nucl. Phys.*, A407:495, 1983.
- [JT55] M. Johnson and E. Teller. Classical field theory of nuclear forces. *Phys. Rev.*, 98:783, 1955.
- [Kap89] J. I. Kapusta. *Finite-Temperature Field Theory*. Cambridge University Press, Cambridge, 1989.
- [Kar02] F. Karsch. Lattice QCD at high temperature and density. *Lect. Notes Phys.*, 583:209–249, 2002.
- [KM] A. K. Kerman and L. D. Miller. Field theory methods for finite nuclear systems and the possibility of density isomerism. (talk). In \*Berkeley 1974, Proceedings, Lawrence Berkeley Lab Lbl- 3675\*, Berkely 1974, 73-107.
- [KM93] C. L. Korpa and R. Malfliet. Towards a relativistic selfconsistent nucleon spectral function in the nuclear medium. *Phys. Lett.*, B315:209–214, 1993.
- [KMN<sup>+</sup>95] H. Kouno, T. Mitsumori, N. Noda, K. Koide, and A. Hasegawa. Effective nucleon mass, incompressibility and third derivative of nuclear binding energy in the nonlinear relativistic mean field theory. *Phys. Rev.*, C51:1754–1761, 1995.
- [KMP87] J. Kunz, D. Masak, and U. Post. Multiple solutions in configuration space in a chiral nuclear model. *Phys. Lett.*, B186:124–128, 1987.
- [KMPB86] J. Kunz, D. Masak, U. Post, and J. Boguta. Finite structures in a saturating chiral field theory. *Phys. Lett.*, B169:133–138, 1986.
- [Koc95] V. Koch. Introduction to chiral symmetry. *nucl-th/9512029*, 1995.



- [Kug97] T. Kugo. *Eichtheorie*. Springer, Berlin, Heidelberg, 1997.
- [LB00] M. Le Bellac. *Thermal Field Theory*. Cambridge University Press, Cambridge, 2000.
- [LEL<sup>+</sup>00] J. Lehr, M. Effenberger, H. Lenske, S. Leupold, and U. Mosel. Transport theoretical approach to the nucleon spectral function in nuclear matter. *Phys. Lett.*, B483:324–330, 2000.
- [Lev67] M. Levy. *Nuovo Cim.*, 52:23, 1967.
- [LLLM02] J. Lehr, H. Lenske, S. Leupold, and U. Mosel. Nuclear matter spectral functions by transport theory. *Nucl. Phys.*, A703:393–408, 2002.
- [LP03] E. Laermann and O. Philipsen. Status of lattice QCD at finite temperature. *Ann. Rev. Nucl. Part. Sci.*, 53:163–198, 2003.
- [LR00] J. T. Lenaghan and D. H. Rischke. The O(N) model at finite temperature: Renormalization of the gap equations in hartree and large-N approximation. *J. Phys.*, G26:431–450, 2000.
- [LRSB00] J. T. Lenaghan, D. H. Rischke, and J. Schaffner-Bielich. Chiral symmetry restoration at nonzero temperature in the SU(3)<sub>(r)</sub> x SU(3)<sub>(l)</sub> linear sigma model. *Phys. Rev.*, D62:085008, 2000.
- [LW60] J. M. Luttinger and J. C. Ward. Ground state energy of a many fermion system. 2. *Phys. Rev.*, 118:1417–1427, 1960.
- [Mat55] T. Matsubara. A new approach to quantum statistical mechanics. *Prog. Theor. Phys.*, 14:351–378, 1955.
- [MPG01] A. Mishra, P. K. Panda, and W. Greiner. Quantum vacuum in hot nuclear matter: A nonperturbative treatment. *J. Phys.*, G27:1561–1576, 2001.
- [MPS<sup>+</sup>97] A. Mishra, P. K. Panda, S. Schramm, J. Reinhardt, and W. Greiner. Structure of the vacuum in nuclear matter: A nonperturbative approach. *Phys. Rev.*, C56:1380–1388, 1997.
- [MR05] M. Mannarelli and R. Rapp. Hadronic modes and quark properties in the quark-gluon plasma. *hep-ph/0505080*, 2005.
- [MS82] T. Matsui and B. D. Serot. The pion propagator in relativistic quantum field theories of the nuclear many body problem. *Ann. Phys.*, 144:107, 1982.

- 
- [NHKK94] M. Nakano, A. Hasegawa, H. Kouno, and K. Koide. Nuclear schwinger-dyson formalism applied to finite baryon density. 1. formulation. *Phys. Rev.*, C49:3061, 1994. SAGA-HE-53-93.
- [NMM<sup>+</sup>94] M. Nakano, T. Mitsumori, M. Muraki, K. Koide, H. Kouno, and A. Hasegawa. Nuclear schwinger-dyson formalism applied to finite baryon density. 2. numerical calculation and medium effects of meson selfenergies. *Phys. Rev.*, C49:3076, 1994. SAGA-HE-54-93.
- [NR76a] E. M. Nyman and M. Rho. Abnormal nuclear matter and many body forces. *Nucl. Phys.*, A268:408–444, 1976.
- [NR76b] E. M. Nyman and M. Rho. Chiral symmetry and many body forces in nuclei. *Phys. Lett.*, B60:134, 1976.
- [PA97a] T. H. Phat and N. T. Anh. The effective action approach applied to nuclear matter - I. *Nuovo Cim.*, 110A:475, 1997.
- [PA97b] T. H. Phat and N. T. Anh. The effective action approach applied to nuclear matter - II. *Nuovo Cim.*, 110A:839, 1997.
- [Pet99] N. Petropoulos. Linear sigma model and chiral symmetry at finite temperature. *J. Phys.*, G25:2225–2241, 1999.
- [Pos98] M. Post. *Diploma Thesis*. 1998. <http://theorie.physik.uni-giessen.de/documents/diplom/dp-post.ps.gz>.
- [PS95] M. E. Peskin and D. V. Schroeder. *An Introduction to Quantum Field Theory*. Perseus Books, Reading, Massachusetts, 1995.
- [PSS<sup>+</sup>97] P. Papazoglou, J. Schaffner, S. Schramm, D. Zschesche, H. Stöcker, and W. Greiner. Phase transition in the chiral sigma omega model with dilatons. *Phys. Rev.*, C55:1499–1508, 1997.
- [PZS<sup>+</sup>99] P. Papazoglou, D. Zschesche, J. Schramm, S. Schaffner-Bielich, H. Stöcker, and W. Greiner. Nuclei in a chiral SU(3) model. *Phys. Rev.*, C59:411–427, 1999.
- [Rei89] P. G. Reinhard. The relativistic mean field description of nuclei and nuclear dynamics. *Rept. Prog. Phys.*, 52:439, 1989.
- [RG94] D. H. Rischke and W. Greiner. A functional integral approach to the thermodynamics of the  $\sigma - \omega$  model. *Int. J. Mod. Phys.*, E3:1157–1194, 1994.
- [Ris04] D. H. Rischke. The quark-gluon plasma in equilibrium. *Prog. Part. Nucl. Phys.*, 52:197–296, 2004.

- 
- [RK04] F. Riek and J. Knoll. Self-consistent description of vector-mesons in matter. *Nucl. Phys.*, A740:287–308, 2004.
- [RR05] J. Ruppert and T. Renk. Non-perturbative finite T broadening of the rho meson and dilepton emission in heavy ion collisions. *Phys. Rev.*, C71:064903, 2005.
- [RRM<sup>+</sup>86] P. G. Reinhard, M. Rufa, J. Maruhn, W. Greiner, and J. Friedrich. Nuclear ground state properties in a relativistic meson field theory. *Z. Phys.*, A323:13–25, 1986.
- [RRR03] D. Röder, J. Ruppert, and D. H. Rischke. Chiral symmetry restoration in linear sigma models with different numbers of quark flavors. *Phys. Rev.*, D68:016003, 2003.
- [RRR05] D. Röder, J. Ruppert, and D. H. Rischke. Selfconsistent calculations of spectral densities in the O(N) model: Improving the hartree-fock approximation by including nonzero decay widths. *hep-ph/0503042*, 2005.
- [Ryd96] L. H. Ryder. *Quantum Field Theory*. Cambridge University Press, Cambridge, 1996.
- [SC85] S. Sarkar and S. K. Chowdhury. Saturating chiral field theory for the study of nuclear matter in the relativistic hartree approximation. *Phys. Lett.*, B153:358–362, 1985.
- [Sch51] L. Schiff. Nonlinear meson theory of nuclear forces. I. neutral scalar mesons with point-contact repulsion. *Phys. Rev.*, 84:1, 1951.
- [Ser92] B. D. Serot. Quantum hadrodynamics. *Rept. Prog. Phys.*, 55:1855–1946, 1992.
- [Sky59] T. H. R. Skyrme. The effective nuclear potential. *Nucl. Phys.*, 9:615, 1959.
- [SL05] S. Shu and J.-R. Li. Thermodynamical consistent CJT calculation in studying nuclear matter. *nucl-th/0503056*, 2005.
- [SMMR01] O. Scavenius, A. Mocsy, I. N. Mishustin, and D. H. Rischke. Chiral phase transition within effective models with constituent quarks. *Phys. Rev.*, C64:045202, 2001.
- [SNR93] M. M. Sharma, M. A. Nagarajan, and P. Ring. Rho meson coupling in the relativistic mean field theory and description of exotic nuclei. *Phys. Lett.*, B312:377–381, 1993.

- 
- [SW86] B. D. Serot and J. D. Walecka. *Advances in Nuclear Physics*, 16:1, 1986.
- [SW97] B. D. Serot and J. D. Walecka. Recent progress in quantum hadrodynamics. *Int. J. Mod. Phys.*, E6:515–631, 1997.
- [vHK00] H. van Hees and J. Knoll. Finite pion width effects on the rho-meson. *Nucl. Phys.*, A683:369–382, 2000.
- [Wal74] J. D. Walecka. A theory of highly condensed matter. *Annals Phys.*, 83:491–529, 1974.
- [Wal95] J. D. Walecka. Theoretical nuclear and subnuclear physics. *Oxford Stud. Nucl. Phys.*, 16:1–610, 1995.
- [Wei74] S. Weinberg. Gauge and global symmetries at high temperature. *Phys. Rev.*, D9:3357–3378, 1974.
- [Wel83] H. Arthur Weldon. Simple rules for discontinuities in finite temperature field theory. *Phys. Rev.*, D28:2007, 1983.
- [WTM<sup>+</sup>87] B. M. Waldhauser, J. Theis, J. A. Maruhn, H. Stöcker, and W. Greiner. Phase structure of excited baryonic matter in the relativistic mean field theory. *Phys. Rev.*, C36:1019–1026, 1987.
- [Yuk35] H. Yukawa. On the interaction of elementary particles. *Proc. Phys. Math. Soc. Jap.*, 17:48–57, 1935.
- [ZGS<sup>+</sup>01] D. Zschesche, L. Gerland, S. Schramm, J. Schaffner-Bielich, H. Stöcker, and W. Greiner. Critical review of quark gluon plasma signals. *Nucl. Phys.*, A681:34–40, 2001.
- [ZPB<sup>+</sup>00] D. Zschesche, P. Papazoglou, C. Beckmann, S. Schramm, J. Schaffner-Bielich, H. Stöcker, and W. Greiner. Chiral model for dense, hot and strange hadronic matter. *Nucl. Phys.*, A663:737–740, 2000.
- [ZPS<sup>+</sup>01] D. Zschesche, P. Papazoglou, S. Schramm, J. Schaffner-Bielich, H. Stöcker, and W. Greiner. Hadrons in dense resonance-matter: A chiral  $SU(3)$  approach. *Phys. Rev.*, C63:025211, 2001.
- [ZW92] W. M. Zhang and L. Wilets. Transport theory of relativistic heavy ion collisions with chiral symmetry. *Phys. Rev.*, C45:1900–1917, 1992.

# DANKSAGUNG

Obwohl auf dieser Doktorarbeit letztlich nur ein einziger Name steht, nämlich meiner, ist sie doch in hohem Maße ein Produkt der vereinten Anstrengung vieler Menschen. Jeder von ihnen hat auf ganz besondere Weise zu ihrem Gelingen beigetragen, und das Fehlen jedes einzelnen hätte ein großes Loch in dieser Arbeit zurückgelassen. Ich habe also allen Anlass, dankbar zu sein.

Das Loch hätte wohl die ganze Arbeit umfasst, wäre mein Doktorvater Dirk Rischke nicht gewesen. Er hat mich während meiner Promotion mit außergewöhnlichem Engagement geleitet und freundschaftlich unterstützt, wo immer es ging. Ich danke ihm für seinen unermüdlichen Einsatz.

Meine Promotion wäre nur schwer ohne die tatkräftige Unterstützung der anderen Mitglieder meiner Arbeitsgruppe möglich gewesen. So danke ich meinen Zimmergenossen Dirk Röder und Detlef Zschesche für die angenehme Arbeitsatmosphäre und ihren Rat, auf den ich nicht hätte verzichten wollen. Viele gute Ideen sind in der Diskussion mit ihnen entstanden.

Auch den Meistern der Vektormesonen, Jörg Ruppert und Stefan Strüber, möchte ich hier danken, denn Vektormesonen sind recht garstige Gesellen, die alleine nur schwer zu bändigen sind.

Sehr viel Mühe hat Susanna Wilms investiert. Sie hat alle meine Rechnungen solange überprüft und hinterfragt bis wir beide der Ansicht waren, sie seien richtig.

Für viele interessante Diskussionen und gute Ideen, die meine Promotion bereichert haben möchte ich unseren Gästen Amruta Mishra, Jonathan Lenaghan, Qun Wang, Igor Mishustin und Lonya Frankfurt danken. Ihre neue Perspektive war mir oft eine große Hilfe.

Ungefähr die Hälfte der Arbeit, die hier niedergeschrieben ist, haben freundlicherweise Computer erledigt. Vermutlich hätten sie sich sofort zur Ruhe gesetzt, hätten nicht unsere Administratoren Gebhard Zeeb und Alexander Achenbach sowie Manuel Reiter und Boris Wagner vom Center for Scientific Computing es verstanden, sie immer wieder zu motivieren. Hierfür sei ihnen gedankt.

Großer Dank gebührt auch Daniela Radulescu, Veronika Palade und Astrid Steidl, die das Institut meisterhaft am Laufen erhalten haben, und ohne die ich meine Promotion wahrscheinlich durch Minnesang auf der Zeil hätte finanzieren müssen. In gewisser Weise ist das Institut für Theoretische Physik wie eine große Familie.

Ich möchte deshalb den Familienvätern Walter Greiner und Horst Stöcker dafür danken, dass sie mich damals aufgenommen haben und meine Arbeit seither mit großem Interesse verfolgen.

Auch meinem Zweitgutachter Carsten Greiner danke ich für sein Interesse an meiner Arbeit und dafür, dass er die Aufgabe der Begutachtung freiwillig übernommen hat.

Einige Menschen haben entscheidend dazu beigetragen, dass ich morgens gerne ins Institut gekommen bin. Sie haben mich daran erinnert, Pausen zu machen, und mich durch ihren Humor vom Mensaessen abgelenkt. Ich danke dafür Thomas Cornelius, Uli Eichmann, Lars Gerland, Uli Harbach, Sabine Hossenfelder, Ben Koch, Manuel Reiter, Philipp Reuter, Dirk Röder, Stefan Scherer, Stefan Strüber, Boris Wagner, Susanna Wilms und Detlef Zschiesche.

Meine Arbeit wurde unterstützt durch die Josef-Buchmann-Stiftung, der ich hiermit ganz herzlich danken möchte. Das Stipendium hat mir eine große Chance eröffnet und mir finanzielle Unabhängigkeit ermöglicht.

Der wärmste Dank gebührt meinen Eltern. Ihre Unterstützung und Anteilnahme hat mich über alle Probleme getragen und die glücklichen Momente dieser Zeit verschönert. Eigentlich hätten sie eine eigene Danksagung verdient.

## AKADEMISCHE LEHRER

Prof. Dr. R. Becker  
Prof. Dr. H. Behr  
Prof. Dr. K. Bethge  
Prof. Dr. R. Bieri  
Prof. Dr. M. Bleicher  
PD Dr. G. Bruls  
Prof. Dr. R. Dreizler  
Prof. Dr. A. Dumitru  
Prof. Dr. T. Elze  
Dr. K. Fendler  
Prof. Dr. W. Greiner  
Prof. Dr. R. Jelitto  
Prof. Dr. H. Klein  
Prof. Dr. B. Luethi  
Prof. Dr. J. Maruhn  
Prof. Dr. W. Metzler  
Prof. Dr. K. H. Müller  
Prof. Dr. E. Mohler  
Dr. J. Reinhardt  
Prof. Dr. D. Rischke  
PD Dr. F. Ritter  
Prof. Dr. A. Schaarschmidt  
PD Dr. Schaffner-Bielich  
Prof. Dr. H. Schmidt-Böcking  
Prof. Dr. S. Schramm  
Prof. Dr. D. Schubert  
Prof. Dr. W. Schwarz  
Prof. Dr. R. Stock  
Prof. Dr. H. Stöcker  
Prof. Dr. H. Ströbele  
Dr. B. Wiedemann





# LEBENS LAUF

Name: **Wolf Christian Beckmann**  
Adresse: Mittelweg 16  
60318 Frankfurt am Main  
Geburtstag/-ort: 1.5.1974 in Düsseldorf  
Familienstand: ledig

## SCHULBILDUNG

1980 – 1984 Römerstadt-Schule (Grundschule),  
Frankfurt am Main  
1984 – 1991 Liebig-Gymnasium in  
Frankfurt am Main  
1991 – 1994 Albert-Einstein-Gymnasium in  
Schwalbach am Taunus  
mit Abschluss Abitur

## UNIVERSITÄT

1994 – 1999 Studium der Physik und Mathematik an der Johann  
Wolfgang Goethe-Universität, Frankfurt am Main  
Oktober 1996 Vordiplom in Physik  
Oktober 1999 Diplom  
Thema der Diplomarbeit: Kerne, superschwere El-  
emente und Hyperkerne in einem chiralen  $SU(3)$ -  
Modell  
Seit 1999 Promotionsstudium am Institut für Theoretische  
Physik der J. W. Goethe-Universität, Frankfurt am  
Main  
1999 – 2002 Graduiertenstipendium der *Josef-Buchmann-Stiftung*  
Seit 2002 Wissenschaftlicher Mitarbeiter am Institut für Theo-  
retische Physik der J. W. Goethe-Universität